Title

Remote Detection of Xenon-based Molecular Sensors and the Development of Novel Paramagnetic Agents

Author

Smith, Monica A.

Publication Date

2012

Remote Detection of Xenon-based Molecular Sensors and the Development of Novel Paramagnetic Agents

by

Monica Ann Smith

A dissertation submitted in partial satisfaction of the
requirements for the degree of
Doctor of Philosophy

in

Biophysics

in the

GRADUATE DIVISION
of the
UNIVERSITY OF CALIFORNIA, BERKELEY

Committee in charge:
Professor David E. Wemmer, Chair
Professor Alexander Pines
Professor Steven Conolly
Professor Daniel Fletcher

Spring 2012

Remote Detection of Xenon-based Molecular Sensors and the Development of Novel Paramagnetic Agents

Abstract

Remote Detection of Xenon-based Molecular Sensors and the Development of Novel Paramagnetic Agents

by

Monica Ann Smith

Doctor of Philosophy in Biophysics

University of California, Berkeley

Professor David E. Wemmer, Chair

Applications of laser-polarized xenon nuclear magnetic resonance (NMR) spectroscopy and imaging have grown in number due to the exceptional sensitivity of xenon to its local environment. When paired with microfluidic technology, xenon-based molecular sensors (XBMS) have the potential to be used in a broad range of applications from medical devices to geochemistry. Detection of XBMS on a microfluidic chip requires remote detection NMR methodology, where the encoding and detection of aqueous xenon is separated in both space and time. In order to give a clear sense for the state of XBMS with respect to both microfluidics in NMR and magnetic resonance (MR) contrast agents, this thesis provides the background of NMR relevant for performing remote detection NMR experiments, a history of laser-polarized xenon NMR spectroscopy, traditional proton-based magnetic resonance (MR) contrast agents, and the development of XBMS as MR contrast agents.

The primary XBMS used in this thesis is a water soluble version of the organic cryptophane-A molecule (cryA). Xenon had been shown to associate with cryA in water with high affinity and relatively fast exchange and cryA can be indirectly detected in low concentrations in solution. A variable previously unexploited in laser-polarized xenon NMR experiments using XBMS was temperature. Temperature is an important parameter in XBMS experiments for generating MR contrast as the affinity for xenon with all soluble versions of cryptophane-A had been shown to increase with increasing temperature and also the exchange of xenon in and out of the cryA was previously shown to increase at higher temperatures. In experiments described in this thesis, temperature was used to increase contrast in both spectroscopic and imaging studies. At 37 °C, the threshold for detecting the presence of a negatively charged cryA in solution was decreased to 10 nM - two orders of magnitude lower than what was previously detectable for a positively charged cryA at 25 °C.

In order to detect the presence of XBMS with an optimized coil separated in space from the location of the sensors (remote detection), a radio frequency (RF) probe tuned to the resonance of xenon was built that was compatible with aqueous xenon flow through 1/16 inch tubing. An efficient means of dissolving xenon into water close to the encoding region was developed leading to the detection of the first aqueous xenon remote detection travel

curves. Furthermore, polystyrene beads grafted with 1.3 mM cryA were loaded into 1/16 inch tubing in the encoding region. By applying a saturation pulse at the cryA resonance frequency in the encoding region, the presence of cryA was remotely detected by monitoring the subsequent decrease in intensity at the aqueous xenon resonance frequency.

Following the remote detection of XBMS in this macroscopic environment, a platform was developed for the remote detection of XMBS on a microfluidic chip. An RF probe tuned to both ^{1}H and ^{129}Xe was designed and fabricated for remote detection experiments at the microfluidic scale. This probe was used to detect aqueous xenon flowing through a microfluidic chip via the time-of-flight dimension. Furthermore, water proton flow through a microfluidic chip was detected in remotely in both spectroscopic and imaging experiments.

Finally, a novel class of XBMS is discussed in detail. Instead of detecting XBMS by their unique resonance frequency in solution, when paired with a paramagnetic center XBMS have the potential to be used as T_1 relaxation agents. The theory of T_1 contrast agents is presented and the simulation developed to model this new type of xenon-based contrast agent is described in detail. The results of the simulation are tabulated and the early work with the first agent synthesized for this purpose is presented. The incorporation of a XBMS T_1 relaxation agent with a microfluidic device could lead to the development of chemically sensitive, portable, low-field devices.

To my family, for their endless love and support.

Contents

List of Figures

List of Tables

Acknowledgments

It is hard to know where to begin. First and foremost, I would like to thank my advisers David Wemmer and Alex Pines. Dave is one of the most brilliant scientists I have had the pleasure to learn from, whose scientific method I will continue to strive to match and whose patience and support I will always cherish. Alex is by far the most charismatic man I have ever met. He was always there to inspire me, generate brilliant ideas, and lend an ear in some of my darker moments. Together, the two strike an unmatchable balance.

I would like to thank Tom L. for getting me started and Leif for not only teaching me most of what I know about the biosensor project, but for being a tremendous friend. ‘Team Biosensor’ would not have been complete without Tyler, Franz, Matt, Tom T., Todd, and Nick G. as an honorary member. I will always cherish these guys for their scientific creativity, stimulating conversations, and friendship. Recently, Dan and Hattie have helped me in more ways than I can express and Vik was always looking out for me behind the scenes. New to the project are Lindsay, Clancy, and Phuong. I am looking forward to hearing about their endeavors as they push the biosensor projects forward over the next few years. Then, I have had the opportunity to work with a number of talented collaborators along the way including Theresa from the Kumar Lab and Gary, Kristen, and Kanna from Matt Francis’s Lab. Unrelated to my research, I would like to thank Pete for being such a great officemate and for listening to my babble over the years. Finally, the lab would not function without Alyse, whose advice I will always appreciate and dedication to the spirit of the ’Girlnuts’ I will always remember.

While I spent most of my time in the Pines Lab, I will forever treasure my peers in the Wemmer Lab. Natasha, Aaron, Joe, and Judy were always there to make me laugh and provide a safe haven when I needed to escape the magnet room. Aleks, Hagit, Alex, and Zhijuan have continued that legacy, making me feel at home on the 5th floor.

Outside of the lab, I will always be indebted my friends. In particular I would like to thank Rose, Sarah, and Michael for dragging me out of the lab and my roommates over the years Jennifer, Melania, Christine, Paul, Amy, Jaime, Lucy, and Sonja for their companionship and support. My life would not be the same without my ‘east coast’ friends, who in spite of the distance were always there for me with arms wide open. Finally, I would like to thank my family for their endless love and encouragement.

Symbols, Constants, and Abbreviations

Symbols

B_0	amplitude of the external magnetic field
γ	gyromagnetic ratio
$\mathbf{I}$	spin operators
T_1	spin-lattice relaxation rate constant
T_{1e}	electronic spin-lattice relaxation rate constant
T_2	spin-spin relaxation rate constant
T_2^*	inhomogeneous spin-spin relaxation rate constant
ω_1	saturation frequency in rad/sec
ω_{ref}	reference radio frequency field strength in rad/sec

Physical Constants

h	Planck's constant, 6.626176×10^{-34} Js
$\hbar$	$\hbar = h/2\pi$
k_B	Boltzmann constant, 1.380662×10^{-23} J/K
β	Bohr magneton, 9.27×10^{-24} J/T
μ_0	Permeability of free space, $4\pi \times 10^{-7}$ H/m

Abbreviations

CEST	Chemical Exchange Saturation Transfer
cryA	Cryptophane-A
FID	Free Induction Decay
FT	Fourier Transform
IR	Inversion Recovery
MRI	Magnetic Resonance Imaging
NMR	Nuclear Magnetic Resonance
RF	Radio Frequency
SEOP	Spin Exchange Optical Pumping
SNR	Signal to Noise Ratio
SPIO	Superparamagnetic Iron Oxide nanoparticle
TE	Time to Echo
TOF	Time-of-flight
TR	Repetition Time
XBMS	Xenon-based Molecular Sensor

Chapter 1

Introduction

Over the past several decades, the semiconductor industry has driven the development of cheap, fast, reliable electronics. In addition to fueling the digital age, the equipment used to make electronic components has aided in microfluidic chip development. The growth of microfluidic technology has revolutionized biomolecular and chemical analysis, with impact ranging from molecular biology to geochemistry. In the biomedical industry alone, close to 230 companies world-wide are developing microfluidic-based point-of-care diagnostics and cutting-edge research tools [74]. Applications of these technologies are used in both academia and industry and include blood analyzers, cell-based assays, immunoassays, PCR, and drug discovery tools. In all of these cases, microfluidics offers a means for devising cheap, portable experiments with limited reagent usage.

Through the turn of the twenty-first century, the advantages of conducting experiments on microfluidic chips had not been paired with the flexibility and chemical sensitivity of nuclear magnetic resonance (NMR). In 2000, Trumbull, et al. tested the potential for this combination by monitoring chemical electrophoresis on a microfluidic chip with a planar radiofrequency (RF) microcoil [133]. In this study, the sensitivity of the microcoil was not adequate to detect the analytes of interest, but water and ethanol were easily detected. Since that time, improvements in planar microcoils led to the detection of chemical reactions on a microfluidic chip [142], implementation of solenoid coils for remote detection of analytes led to the tracking of mixing of immiscible solvents ([6], [58], [59]), and data acquisition advances such as compressed sensing led to velocity mapping of water flowing through a serpentine chip [10]. The principles of magnetic resonance and remotely detected NMR relevant to this thesis will be reviewed for clarity in Chapter 2.

As microfluidic applications for remotely detected proton-based applications advanced, xenon-based molecular sensors (XBMS) were being developed as targeted MR contrast agents. These organic sensors, known to reversibly host xenon, were first solubilized and functionalized for targeted applications in 2001 [124]. Over the past decade, clever pulse sequences for indirect detection of the sensors [116] and sensor scaffolding via biological agents ([93], [126]) have driven the threshold for detecting these agents into the sub-nanomolar regime. The fundamentals of xenon NMR and xenon-based molecular sensors will be reviewed in Chapters 3 and 4, followed by the author's contributions to lowering the threshold for detecting XBMS in Chapter 5.

While originally developed with biomedical applications such as early tumor detection in mind, XBMS are ideal for analytical applications. This thesis combines the sensitivity of xenon to its local environment with the utility of microfluidics and remotely detected NMR spectroscopy in order to develop a platform for detecting an array of XBMS sensors on a microfluidic chip. A method was established for dissolving xenon into water as it flows through 1/16 inch tubing to a region containing the sensors, followed by remote detection of the sensors with a home-built detection probe (Chapter 6). Additionally, a dually tuned probe was designed and constructed to detect both water protons and xenon with a micro solenoid coil and was paired with a commercially available RF probe for chip-based spectroscopic and imaging applications (Chapter 7).

In addition to using variations on currently available sensors to develop a library for screening for biological and chemical analytes, it would be very interesting to consider using a new class of sensors with the same organic molecule as its base. Instead of localizing sensors by their unique xenon chemical shift, a paramagnetic XMBS could induce local changes in xenon's relaxation rate that are significantly different from the relaxation of bulk xenon in water. The principle of T_1 relaxation with paramagnetic sensors is reviewed in Chapter 8, where the simulations used to guide the design of a novel sensor and initial experimental results are also described. Finally, Chapter 9 gives a perspective on the future of combinatorial screening with xenon-based molecular sensors.

Chapter 2

Background on Nuclear Magnetic Resonance Spectroscopy and Imaging

A full, quantum mechanical description of NMR is simultaneously simplistic and complex. While beautiful to behold, it has been reviewed at length by countless authors. For this reason, a full, comprehensive overview of NMR will not be presented here. Instead, the details of NMR and MRI directly relevant to this thesis will be presented below. For more in-depth information about NMR, the reader is referred to Keeler [70] and Levitt [80] for introductory material or Abragam [3] and Ernst [39] for a more thorough description of the subject. Furthermore, the fundamentals of MRI are presented with extreme clarity in Nishimura [97], to which the reader is referred if wanting for more information on this topic.

2.1 Spin

Through the early 20^{th} century, people of all ages could talk about 'spin'. The earth spins on its axis, at least from the perspective of the $19th$ century and forward. An ice skater turns about herself, a top precesses... In all of these cases, spin is referring to angular momentum, the generator of physical rotations. Then, in 1922, Stern and Gerlach shocked the scientific community by discovering that electrons also have spin. Unlike the manifestation of their macroscopic counterparts, electrons have an intrinsic spin that is quantized rather than continuous. Quantum mechanics was born.

Like the electron, it was found that the nucleus has spin. This spin, or spin angular momentum $\mathbf{S}$, is also the generator of rotations in the presence of a magnetic field. When combined with a magnetic field, nuclear spin is the basis for all of NMR. All nuclei with spin $\geq 1/2$ are observable by NMR, provided that their lifetime is long enough. The result of spin is that the nucleus posesses a magnetic moment

$$\boldsymbol{\mu} = \gamma \mathbf{S} = \gamma \hbar \mathbf{I} \tag{2.1}$$

where, γ in (rad/sec) is a proportionality constant called the gyromagnetic ratio that is an intrinsic property of the nucleus, $\hbar$ is Planck's constant divided by 2π, and $\mathbf{I}$ is the spin

Table 2.1: Nuclear Spins and Gyromagnetic Ratios for Commonly Used Nuclei. Adapted from Levitt [80].

Nucleus	Spin Number	Gyromagnetic Ratio (rad sec^{-1} T^{-1})
^{1}H	1/2	267.522
^{2}H	1	41.066
^{3}H	1/2	285.349
^{13}C	1/2	67.283
^{15}N	1/2	-27.126
^{19}F	1/2	251.815
^{23}Na	3/2	70.808
^{31}P	1/2	108.394
^{129}Xe	1/2	-74.521

operator. Table 2.1 provides a list of spin numbers and gyromagnetic ratios for nuclei typically considered for NMR experiments and less commonly used nuclei presented in this thesis.

Observable signal arises from the component of spin initially aligned with the magnetic field, I_z. From quantum mechanics, the number of observable states equals $2I + 1$ given by $I_z = -I, -(I+1), \ldots, (I-1), I$. Therefore, nuclei with spin-1/2 will have the simplest spectra as they only have two spin states, $I_z = \pm 1/2$. Unless otherwise noted, the details presented in this chapter pertain to spin-1/2 nuclei.

2.2 Zeeman Effect

Now that we have our spin-1/2 nucleus, what happens when it is placed in a magnetic field? Classically, the potential energy for the system is given by $E = -\mu \cdot \mathbf{B}$. Assuming the external field is applied along the z-axis, $\mathbf{B} = (0\hat{\imath}, 0\hat{\jmath}, B_0\hat{k})$,

$$\begin{aligned} E &= -\mu \cdot \mathbf{B} && (2.2)\\ &= -\gamma\hbar I_z B_0 && (2.3)\\ &= I_z \hbar\omega_0 && (2.4)\end{aligned}$$

where $\omega_0 \equiv -\gamma B_0$ is defined as the Larmor frequency. For spin-1/2 nuclei with $I_z = \pm 1/2$, the presence of an external magnetic field results in an energy splitting with the difference in energy between the two states equal to $\Delta E = \hbar\omega_0$ (Figure 2.1). This energy splitting is commonly known as the Zeeman Effect.

2.3 Magnetization

For nuclei with a positive gyromagnetic ratio such as ^{1}H, $I_z = +1/2$ corresponds to the lower energy state $E = -\frac{1}{2}\gamma\hbar B_0$. Spins in a magnetic field will have a slight bias for populating this state over the higher energy state $I_z = -1/2$ (Figure 2.1). This bias gives rise to

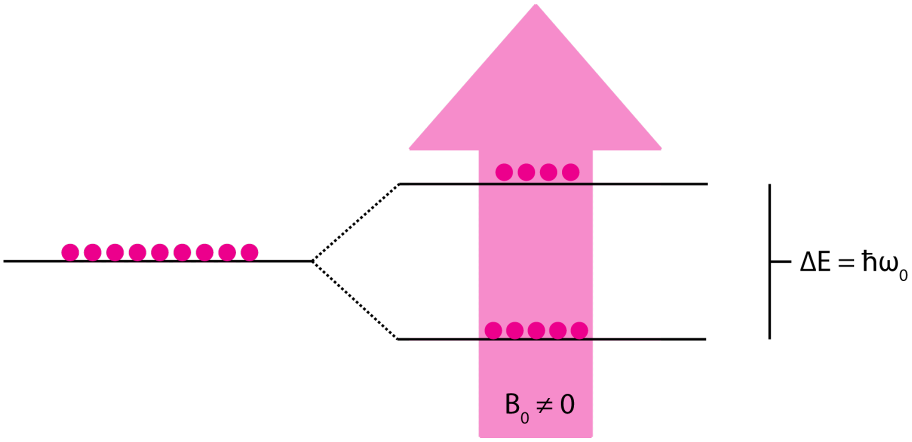

Figure 2.1: Zeeman Effect. When an external magnetic field is applied, a Boltzmann distribution of spin states gives a slight population difference for the two states in a spin-1/2 system. The difference in energy between the two states is $\Delta E = -\gamma\hbar B_0 = \hbar\omega_0$ where ω_0 is the nuclear Larmor frequency.

an initial net magnetization vector aligned with the external magnetic field.

The initial magnetization of a spin active sample in a magnetic field is given by

$$M_0 = \frac{1}{2} N_s \gamma \hbar P \tag{2.5}$$

where γ is the gyromagnetic ratio, $\hbar$ is Planck's constant divided by 2π, N_s is the number density of spins and P is the polarization of the sample. At thermal equilibrium, polarization is given by the Boltzmann distribution

$$\begin{aligned} P &= \frac{N_\alpha - N_\beta}{N_\alpha + N_\beta} && (2.6) \\ &= \frac{e^{-E_\alpha/kT} - e^{-E_\beta/kT}}{e^{-E_\alpha/kT} + e^{-E_\beta/kT}}. && (2.7) \end{aligned}$$

Given that $\Delta E = E_\beta - E_\alpha$,

$$\begin{aligned} P &= \tanh(\frac{\gamma\hbar B_0}{kT}) && (2.8) \\ &\approx \frac{\gamma\hbar B_0}{2kT} && (2.9) \end{aligned}$$

since $\gamma\hbar B_0 \ll kT$. For protons in a 7.05 T magnet at room temperature (typically 18 °C in the Pines Lab), the Boltzmann distribution results in a 25 parts per million population difference for water protons.

2.4 Theoretical Basis for the NMR Signal

Given that the population difference is so low at thermal polarization, how is it possible to detect a MR signal? Inserting thermal polarization into Equation 2.5,

$$M_0 = \frac{N_s \gamma^2 \hbar^2 B_0}{4kT}. \tag{2.10}$$

Equation 2.10 suggests that the initial magnetization scales linearly with the number density of spins in the sample (N_s) and with the strength of the magnetic field (B_0) and inversely with temperature (T). Thus, the initial magnetization will be larger at higher magnetic field strengths and lower temperatures. Furthermore, with the water proton concentration close to 110 M, the net magnetization is detectable, even at low field strengths. For xenon dissolved into water at μM - mM concentrations, detection of aqueous xenon-129 is more challenging, the details of which will be addressed in Chapter 3.

2.4.1 The Bloch Equation

Typically, the direction of the main magnetic field is considered the z' direction in the laboratory frame with x' and y' perpendicular to this axis. For the NMR experiments considered in this thesis, magnetization will be detected inductively by coils placed in the x'-y' plane. Therefore, the initial magnetization must be perturbed for a signal to be detected. When a pulse tuned to the nuclear Larmor frequency is applied to the sample, the net magnetization is tipped away from equilibrium along the z'-axis. Once the spins are no longer in equilibrium,

$$\boldsymbol{\tau} = \boldsymbol{\mu} \times \mathbf{B} \tag{2.11}$$

where τ is the torque acting on a magnetic dipole moment in the presence of a magnetic field. As τ is the time derivative of the angular momentum, $\tau = \mathrm{d}\mathbf{S}/\mathrm{d}t$. Then,

$$\frac{\mathrm{d}\mathbf{S}}{\mathrm{d}t} = \mu \times \mathbf{B} \tag{2.12}$$

$$\frac{\mathrm{d}\mu}{\mathrm{d}t} = \mu \times \gamma\mathbf{B}. \tag{2.13}$$

Given the number density as a function of position x within the sample ($\rho(x) = N(x)/V$) of N magnetic dipoles in a sample of volume V, the sample magnetization is $M(x) = \rho(x)\mu(x)$. Then, the time evolution of magnetization is described by the Bloch Equation [18]

$$\frac{d\mathbf{M}}{dt} = \mathbf{M} \times \gamma\mathbf{B}. \tag{2.14}$$

2.4.2 Pulses in the Rotating Frame

Traditionally, the pulse used to excite spins in an NMR experiment is a linearly polarized electromagnetic wave. When decomposed, this pulse can be viewed as containing one circular

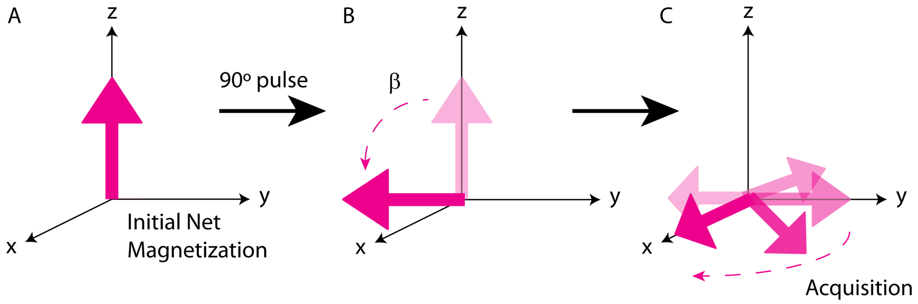

Figure 2.2: Pulse Acquire Experiment. A) The initial net magnetization vector is aligned with the external magnetic field. B) An RF pulse viewed from the rotating frame is tipped away from equilibrium. The angle through which the magnetization vector nutates is given by $\beta = \omega_1 \tau$. C) Following application of the RF pulse, the magnetic moments precess about the external magnetic field.

component tuned close to the resonance frequency of the spins, $-\omega_{\text{ref}}$ for spins with positive γ and another at $+\omega_{\text{ref}}$ which is hundreds of MHz off-resonance of the Larmor frequency and therefore does not affect the spins. That the component $-\omega_{\text{ref}}$ is tuned to the Larmor frequency, typically 10s to 100s of MHz, gives the pulse its more common name, the radio frequency (RF) pulse.

Viewing an NMR experiment from the reference frame of this pulse, the rotating frame, simplifies analysis considerably. If a pulse is applied along one axis, say +x, the effective field seen by the magnetic moments during the pulse reduces to $B_{\text{eff}} = (B_1, 0, \Delta B_0)$ where ΔB_0 is the residual field along the z-axis. It is clear to see why an RF pulse perturbs the system, as the spins will now experience a torque inducing precession about the x-axis. With the application of an RF pulse, the initial magnetization vector nutates away from the positive z-axis towards the -y-axis in a right-handed coordinate system (Figure 2.2B). The angle of nutation, β, is directly related to the strength of the B_1 field and the duration of the RF pulse

$$\beta = \omega_1 \tau \tag{2.15}$$

where $\omega_1 = \frac{1}{2}\gamma B_1$ for a linear RF pulse and τ is the duration of the pulse. In a practical NMR experiment the value τ is referred to as the pulse width of the applied pulse. When $\beta = \omega_1 \tau = \frac{\pi}{2}$, τ is commonly referred to as the 90 time. This time corresponds to the moment when the initial magnetization has been tipped 90 degrees out of equilibrium and the signal detected in the M_{xy} plane is at a maximum. Similarly, when $\omega_1 \tau = \pi$, τ is referred to as the 180 time and corresponds to the point in which the initial magnetization is fully inverted. In an ideal experiment, the signal is zero here as none of the magnetization remains in the x-y plane.

If viewed from the rotating frame, a pulse along the x-axis results in a field $\mathbf{B} = (\frac{1}{2}\mathrm{B}_1, 0, 0)$, where the x-component is equal to half of the full field strength since only half of the linear field is on-resonance with the Larmor frequency. Then, the time precession of magnetization as defined in Equation 2.14 is given by

$$\frac{d}{dt}M_x(t) = 0 \tag{2.16}$$

$$\frac{d}{dt}M_y(t) = \frac{1}{2}\gamma M_z \mathrm{B}_1 \tag{2.17}$$

$$\frac{d}{dt}M_z(t) = -\frac{1}{2}\gamma M_y \mathrm{B}_1 \tag{2.18}$$

Solving these coupled differential equations gives $M_x(t) = 0$, $M_y(t) = M_z\mathrm{cos}(\frac{1}{2}\gamma\mathrm{B}_1 t)$, and $M_z(t) = -M_y\mathrm{sin}(\frac{1}{2}\gamma\mathrm{B}_1 t)$.

2.4.3 Ideal Free Induction Decay

Following application of the B_1 excitation pulse along the +x axis, precession is once again about the external magnetic field (Figure 2.2C). When receiver coils are placed perpendicular to the main magnetic field, the precession of spins is inductively detected via Faraday's Law

$$\epsilon = -\frac{\mathrm{d}\Phi(t)}{\mathrm{d}t} \tag{2.19}$$

where ϵ is the electromotive force and $\Phi(t) = B(t)\mathrm{A}$ is the magnetic flux of the precessing magnetization vector $B(t)$ through the coils with cross-sectional area A. During precession, the magnetic field can be decomposed into

$$B(t) = \left(\frac{\omega_{RF}}{\gamma} + \frac{\Omega}{\gamma}\right)t \tag{2.20}$$

where and γ is the gyromagnetic ratio, ω_{RF} is the transmitted radio frequency tuned close to the Larmor frequency and Ω is the difference between the transmitted frequency and the resonance frequency of the nuclei of interest. Typically, the signal detected in the coil is demodulated by mixing it with the opposite of the transmitted frequency $-\omega_{RF}$, such that the recorded signal only retains the off-resonance frequencies Ω. The result of this detection scheme is known as the free induction decay (FID). In an ideal system, the FID would be an un-damped sinusoid of the form $s(t) = \cos(\Omega t)$ (Figure 2.3A). In practice, most samples contain a range of resonance frequencies. Then, the FID becomes the sum of these individual components

$$s(t) = \sum_i A_i \mathrm{cos}(\Omega_i t) \tag{2.21}$$

where A_i is the amplitude of the component with frequency Ω_i.

2.4.4 Quadrature Detection and Phase Cycling

For any real experiment, the FID is the sum of the frequencies, amplitudes, and phases of many oscillating waves. In modern spectrometers, the signal resulting in the FID is detected

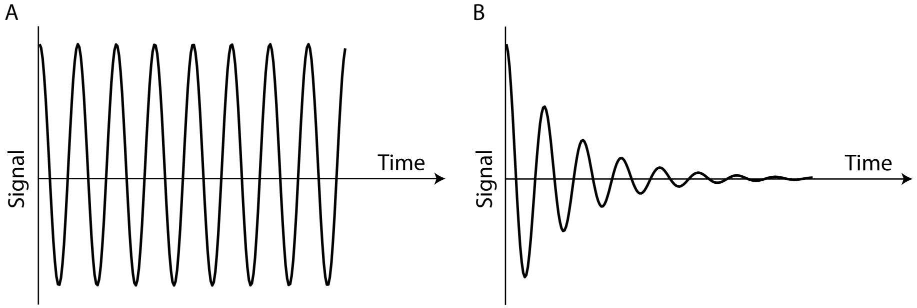

Figure 2.3: Free Induction Decay. A) Free induction decay (FID) is the signal detected by receiver coils following application of an RF pulse to tip the initial magnetization vector into the x-y plane. An ideal FID would oscillate without damping at the resonance frequency of the chemical species of interest. B) In practice, the FID exponentially decays to zero due to T2 relaxation.

using two orthogonal detection channels along the x and y axes. This is known as quadrature detection and the signal equation is instead given by

$$\begin{aligned} s(t) &= [\cos(\Omega t) + \imath\sin(\Omega t)] && (2.22)\\ &= e^{\imath\Omega t} && (2.23) \end{aligned}$$

where $\cos(\Omega t)$ is detected in the x-channel and $\sin(\Omega t)$ is detected in the y-channel. Using a quadrature detection scheme, it becomes possible to uniquely assign resonance frequencies. Without the simultaneous acquisition of $\cos(\Omega t)$ and $\sin(\Omega t)$, it would be impossible to resolve $\cos(\Omega t)$ from $\cos(-\ \Omega t)$.

The choice of applying an RF pulse along the +x axis is somewhat arbitrary. The B_1 field can be applied along any of the +x, +y, -x, or -y directions with the difference in the phase of the applied pulse resulting in a net phase shift of the magnetization vector. When more than one spectra is acquired, application of the B_1 field is typically cycled through the (+x, +y, -x, -y) axes in a combination that results in the accrual of the signal of interest with concurrent elimination of unwanted effects due to imperfect pulses. Application of pulses in this manner is broadly referred to as phase cycling.

2.5 Relaxation

In a perfect experiment, the signal picked up by the receiver coil would oscillate, undamped, at the resonance frequency of the nucleus of interest (Figure 2.3A). In practice, magnetization is restored to equilibrium by two components: T_1 and T_2 relaxation.

2.5.1 T_1 Relaxation

T_1, or spin-lattice, relaxation is the tendency for the magnetization vector to return to equilibrium due to interactions with the surrounding lattice. Thus far, the magnetization vector has been tipped away from thermal equilibrium by applying a pulse at the resonance frequency of the nucleus of interest. This results in an energetically unfavorable state. When the energy of the system lattice matches the Larmor resonance frequency, the magnetic field associated with molecular rotations induces the high-energy spins to return to their lower energy state. Mathematically, T_1 is the time constant that governs the return of the magnetization vector to thermal equilibrium. For example, after inversion of the equilibrium magnetization, T_1 is determined by

$$M_z(t) = M_0(1 - 2e^{-t/T_1}) \tag{2.24}$$

where $M_z(t)$ is the longitudinal magnetization at a time t following the conclusion of the excitation pulse and M_0 is the amplitude of the initial magnetization vector. Smaller T_1 relaxation constants lead to a faster return to equilibrium.

T_1 relaxation is magnetic field dependent, with shorter T_1 time constants observed at lower field strengths due to the greater accessibility of lower energy fluctuations at the Larmor resonance frequency. For water protons at high field, T_1 is typically on the order of 3 to 5 seconds and the time between consecutive experiments (TR) is set to five times this value in order for the initial magnetization to fully recover before beginning the next experiment. As will be described in more detail in Chapter 4, the observed signal for xenon-based experiments is dictated by hyperpolarized nuclei. T_1 changes dramatically for xenon depending on its environment with values ranging from hours in the solid form [46] to seconds for xenon dissolved in deoxygenated blood [16]. Rather than governing the repetition time between experiments, for xenon-based experiments T_1 defines the time constant for which all experiments must be conducted before polarized xenon must be refreshed.

Measuring T_1: The Inversion Recovery Pulse Sequence

While multiple pulse sequences can be used in theory, T_1 is most often determined using an inversion recovery (IR) pulse sequence. In an IR experiment, the net magnetization is first inverted from +z to -z with a 180 degree pulse (Figure 2.4A) . A delay period, τ, is then incremented such that more of the magnetization returns to thermal equilibrium before a 90 degree readout. The time dependence of the return of a fully inverted magnetization vector to thermal equilibrium is expected to follow Equation 2.24. A simulation for a fit to the integrated signal from an IR experiment is presented in Figure 2.4B for a T_1 of 3 seconds.

2.5.2 T_2 Relaxation

T_2, or spin-spin, relaxation is the time constant that describes the loss of coherence of the net magnetization following excitation into the x-y plane. At the end of the initial excitation pulse, magnetization is fully aligned when viewed in the rotating frame. Following termination of the pulse, the magnetization vector precesses about the z-axis. In the absence of local field inhomogeneities, this vector would continue to precess about the z-axis, but its magnitude would shrink in time as T_1 relaxation returned the magnetic moment back towards the low energy state along the z-axis. In practice, local field variations due to

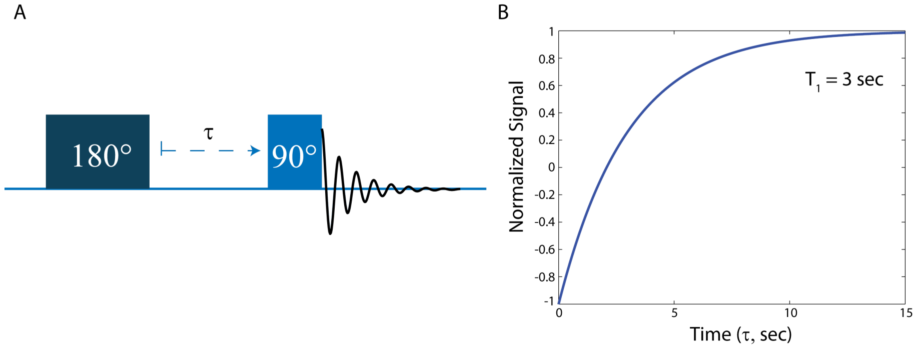

Figure 2.4: Inversion Recovery. A) Schematic for an Inversion Recovery (IR) pulse sequence to measure the T_1 of a sample. Here, a 180 degree pulse is applied to fully invert the spins, followed by an incremented delay period τ. After the delay, a 90 pulse is applied to read out the signal intensity. This signal is then integrated with a constant phase matching the case at where $\tau = 0$. B) A simulation for the fit to an IR pulse sequence for $T_1 = 3$ seconds.

random molecular motion are unavoidable. The component of these fluctuations along the z-axis will cause spins to precess at speeds that vary slightly from the Larmor frequency. As a vector model, this causes a fanning out of the magnetization vectors in the x-y plane - an effect the leads to decoherence of the net magnetization vector (Figure 2.5B). Due to these local field variations, magnetization in the x-y plane decays exponentially as

$$M_{xy}(t) = M_0 e^{-t/T_2}. \tag{2.25}$$

T_2 relaxation is a component of its more general counterpart, T_2^*. T_2^* is the combination of local field variations due to molecular motion, or the homogeneous contribution, and inhomogeneous contributions (T_2') such as magnetic field gradients, poor shimming conditions, etc. The homogeneous and inhomogeneous contributions add reciprocally as

$$\frac{1}{T_2^*} = \frac{1}{T_2} + \frac{1}{T_2'}. \tag{2.26}$$

Depending on the pulse sequence used, T_2 or T_2^* is manifested in the linewidth ($\Delta\nu$) of the resulting spectrum where

$$\Delta\nu = \frac{1}{\pi T_2(^*)} \tag{2.27}$$

Refocusing Inhomogeneities - The Spin Echo

The effect of T_2 inhomogeneity begins following a pulse along the y-axis that tips the initial equilibrium magnetization vector into the transverse plane. As described above, the spins then begin to experience dispersion in phase due to both homogeneous and inhomogeneous magnetic field fluctuations. The phase accrued during the time t following excitation is

$$\phi(x, y, z, t) = \omega_{ext}(x, y, z)t \tag{2.28}$$

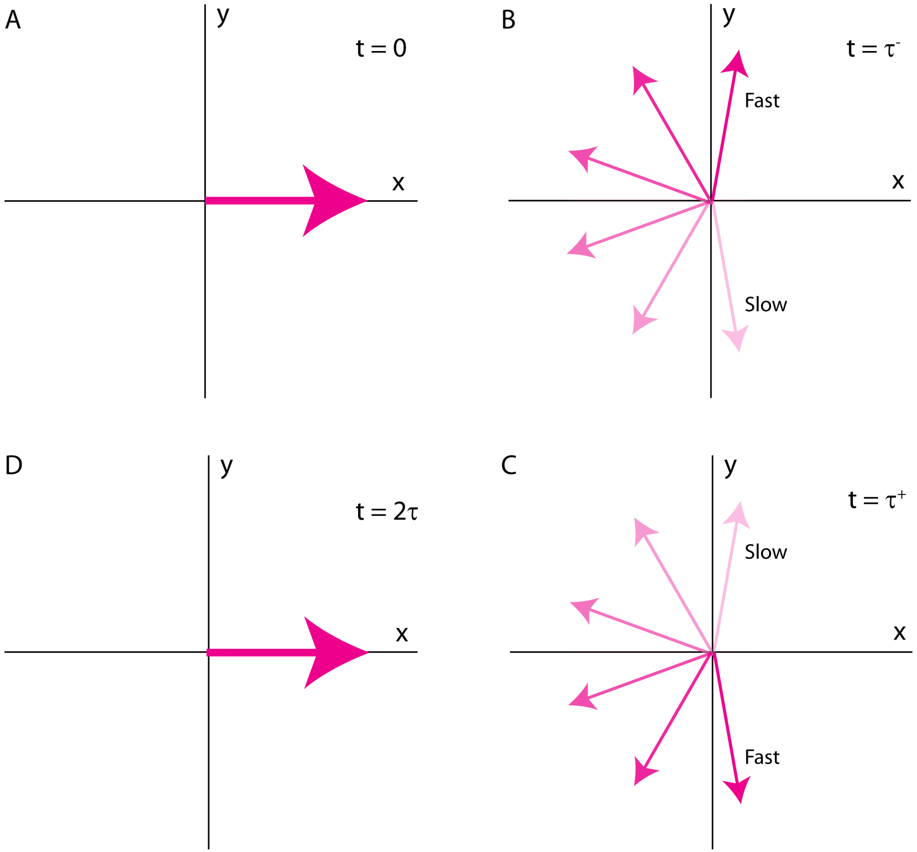

Figure 2.5: Spin Echo. A) Following application of a 90 degree pulse along the y-axis, the net magnetization vector is coherently aligned along the x-axis. B) After a time τ, the phase of the magnetization has fanned out due to local magnetic field homogeneities that add or subtract from the Larmor precession frequency. C) Application of a 180 degree pulse along the x-axis inverts the vectors about this axis. D) The magnetization vectors then precess with their original frequency and realign after a total time 2τ.

where $\omega_{ext}(x, y, z)$ are the spatially dependent resonance frequencies accounting for local magnetic field effects. After a time τ, $\phi(x, y, z, \tau)$ will have accumulated a significant dispersion (Figure 2.5). To rephrase the spins, the key element is to apply a 180 degree pulse at time τ. If this 180 degree pulse is along the x-axis, the phases are reflected about x by 180 degrees and $\phi(x, y, z, \tau^-) \to \phi(x, -y, -z, \tau^+)$. Following this pulse, the accrual of phase over the next time period τ occurs as it did previously and at a time 2τ, the result of this 'spin echo' experiment is that the spins will be exactly rephrased assuming they have not moved in the inhomogeneous field during τ. The spin echo sequence was first described by Erwin Hahn in 1950 [52] and continues to be a vital component of NMR pulse sequence development and data analysis.

Measuring T2 - Carr-Purcell-Meiboom-Gill Pulse Sequence

If instead of a single spin echo sequence an array of 180 degree pulses is applied in series, the homogeneous T_2 relaxation time constant can be extracted. This sequence was

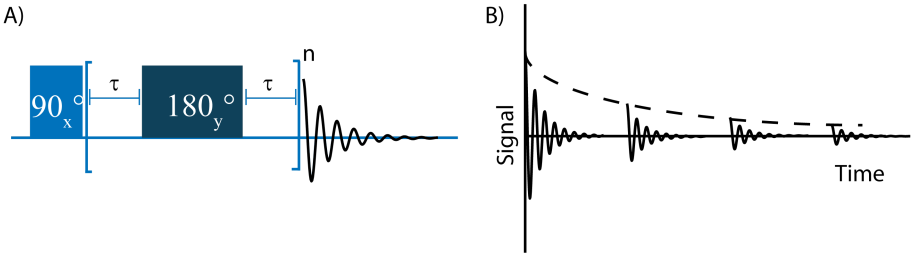

Figure 2.6: Carr-Purcell-Meiboom-Gill Pulse Sequence. A) Following a 90 degree excitation along the x-axis, a series of $\tau - 180_y - \tau$ periods are applied with subsequent readout of the signal between each period. B) Fitting an exponential decay to the resulting series of echoes results in the intrinsic T_2 time constant.

developed by a combination of Carr, Purcell, Meiboom, and Gill ([28], [91]) and is generally referred to as a CPMG pulse sequence. In a CPMG pulse sequence, a series of $\tau - 180 - \tau$ periods continuously refocus the inhomogeneous components of T_2^* (Figure 2.6A). When the individual echoes are integrated, an exponential fit to the signal gives the intrinsic T_2 relaxation time constant (Figure 2.6B).

2.6 The NMR Signal

T_1 and T_2 relaxation are very real contributions to any NMR experiment and their presence is not all bad. Without T_1 relaxation, it would not be possible to regain initial magnetization without external methods such as hyperpolarization. Furthermore, both T_1 and T_2 relaxation can be used to generate contrast in MR images. The Bloch Equations accounting for T_1 and T_2 relaxation are

$$\frac{d\mathbf{M}}{dt} = \mathbf{M} \times \gamma\mathbf{B} - \frac{M_x\mathbf{i} + M_y\mathbf{j}}{T_2} - \frac{(M_z - M_0)\mathbf{k}}{T_1}. \tag{2.29}$$

Solutions to these coupled differential equations provide a powerful predictive tool for assessing the potential for novel experiments.

2.6.1 Fourier Transform for NMR Spectroscopy

While the precessing magnetization generates a FID in the time domain, the true power of NMR spectroscopy is in the ability to resolve unique chemical species contained within a sample. This is accomplished by analyzing the collected FID following a series of RF pulses for signature sets of resonance frequencies. While more than one method for frequency analysis exists, the most common by far is the use of the Fourier Transform (FT). The Fourier Transform provides the means for mathematically transforms a time varying function $s(t)$ into its resonance frequencies ($S(\omega)$)

$$S(\omega) = \int s(t)e^{-i\omega t}\mathrm{d}t \tag{2.30}$$

where ω and t form a conjugate pair and $\omega = (\Omega + \omega_{ref})$ as in Equation 2.20. When relaxation is considered, the FID detected in quadrature is given by

$$s(t) = (\cos(\Omega t) + \imath \sin(\Omega t))\, e^{-t/T_2^*}. \tag{2.31}$$

The result of integrating Equation 2.30 using $s(t)$ in Equation 2.31 is a Lorenzian signal that depends on frequency, $\Delta\omega = \omega_{ref} - \Omega$, as

$$S(\omega) = A(\Delta\omega) - \imath D(\Delta\omega) \tag{2.32}$$

where $A(\Delta\omega)$ is the real, absorptive signal that is mathematically equivalent to

$$A(\Delta\omega) = \frac{1/T_2^*}{(1/T_2^*)^2 + (\Delta\omega)^2} \tag{2.33}$$

and $D(\Delta\omega)$ is the imaginary, dispersive component

$$D(\Delta\omega) = \frac{\Delta\omega}{(1/T_2^*)^2 + (\Delta\omega)^2}. \tag{2.34}$$

Typically, $A(\Delta\omega)$ is displayed and this real component of the spectrum is further decomposed into its individual resonance frequencies. The maximum signal $A(\Delta\omega)_{max}$ is obtained by iteratively multiplying the original signal $S(\omega)$ by a phase factor $e^{-\imath\phi}$. This phase factor cancels the imaginary component $D(\Delta\omega)$ and is commonly referred to as 'phasing' the spectrum.

2.6.2 Signal to Noise Ratio

In the early days of NMR, it was standardly assumed that detectable signal, dictated by the signal-to-noise (SNR) ratio scaled as $B_0^{3/2}$ [64]. While correct in some scenerios, the theory used to derive this value failed to account for the system noise in some limits. Adequate SNR is critical for conducting an NMR experiment and considerations for this ratio will be presented below.

Signal

As stated in Section (2.4.3), magnetization is inductively detected via Faraday's Law (Equation 2.19). When assessing the signal induced in the receiver coils, it is useful to consider the RF field produced at a point (x, y, z) per unit current in the coil, $B_1(x, y, z)$. From the principle of reciprocity, it can be shown that the EMF produced in the coil by a single magnetic dipole is [64]

$$\epsilon = -\frac{\partial}{\partial t}\left[B_1(x,y,z) \cdot \mu(x,y,z,t)\right]. \tag{2.35}$$

By integrating over the volume of the sample

$$s_r(t) = -\int\limits_{vol} \frac{\partial}{\partial t}\left[B_1(x,y,z) \cdot M(x,y,z,t)\right] dV \tag{2.36}$$

where $s_r(t)$ is the total EMF signal seen by the receiver. Assuming that $B_1(x, y, z)$ is constant along the x-y plane, the RF field is represented by B_{1xy}. In the absence of T_2 decay, the signal in an NMR experiment is given by

$$\begin{aligned} s_r(t) &= -\int\limits_{vol} B_{1xy} \frac{\partial}{\partial t} M(x, y, z, t)\, dV && (2.37) \\ &= -\int\limits_{vol} B_{1xy} M_0(x, y, z) \frac{\partial}{\partial t} e^{-\imath\omega t}\, dV && (2.38) \\ &= i\omega_0 B_{1xy} \int\limits_{vol} M_0(x, y, z) e^{-i\omega_0 t} \mathrm{d}V && (2.39) \\ &= i\omega_0 B_{1xy} e^{-\imath\omega_0 t} M_0 V_{sample} && (2.40) \end{aligned}$$

Then, if the received EMF $s_r(t)$ is mixed with the phase factor $e^{+\imath\omega_0 t}$, the processed signal described previously in Equation 2.22 is given by

$$s(t) = \imath\omega_0 B_{1xy} M_0 V_{sample}. \tag{2.41}$$

Given that $\omega_0 \equiv -\gamma B_0$ and $M_0 \propto B_0$ (Equation 2.10), for a thermally polarized sample, the signal detected by the receiver coil scales as B_0^2.

Noise

Noise in a sample can be broken up into three regimes: sample noise, coil noise, and noise due to the pre-amplifier. In all cases, the noise associated with NMR experiments is assumed to be Gaussian, white noise with a flat power spectral density function. Furthermore, noise sources are assumed to be additive. In modern spectrometers, noise from a commercially available pre-amplifier is assumed to be negligible. Therefore, sample-dominated noise and coil-dominated noise are considered in this analysis.

In the limit where sample and coil noise contribute to the total noise, the Nyquist formula for root-mean-square (rms) noise becomes

$$N_{rms} = \sqrt{4k(T_c R_c + T_s R_s)\Delta f} \tag{2.42}$$

where k is the Boltzmann constant, $T_{c,s}$ and $R_{c,s}$ are the temperature and resistance respectively of the coil (c) and sample (s) respectively. This assumes that the dimensions of both the coil and the sample are significantly smaller than the electromagnetic wave applied as the RF field. Coil noise is attributed to electron-photon interactions, where electrons virtually interact with the vibrational motion of the lattice [63]. In this regime, the skin depth for current flow over the surface of the wire contributes to the resistance of the coil. Skin depth is given by

$$\delta = \sqrt{\frac{2\rho(T_c)}{\omega_0 \mu \mu_0}} \tag{2.43}$$

where $\rho(T_c)$ is the resistivity of the conductor at a function of temperature, ω_0 is the Larmor frequency, μ is the permeability of the wire and μ_0 is the permeability of free space. Then, then for a cylindrical conductor, the coil resistance is given by [64]

$$\begin{aligned} R_c &= \frac{l\rho(T_c)^2}{p\delta} && (2.44)\\ &= \left(\frac{l}{p}\right)\left(\frac{\omega_0\mu\mu_0\rho(T_c)}{2}\right)^{1/2} && (2.45)\end{aligned}$$

where l is the length of the conductor, p is the circumference of the cylinder, and the remainder are defined in Equation 2.43. Therefore, coil noise scales as $B_0^{1/2}$ and SNR in the limited of coil-dominated noise scales as $B_0^{7/4}$.

Sample noise is a consideration in highly conductive samples such as the body. In this regime, the resistance of the sample noise is given by [63]

$$R_s = \left(\frac{e\omega\mu_0}{4\pi}\right)^2\left(\frac{C}{b}\right)\times\int_{sample}\sum_{i,j,k}\left[\oint\frac{d\mathbf{s}\cdot\hat{e}}{r}\right]^2 dV \tag{2.46}$$

where C is the concentration of ions, b is a constant proportional to the viscosity, μ_0 is the permeability of free space, ω is the Larmor frequency, and $\hat{e}$ is the principle axis pointing along (i, j, k). Substituting the sample resistance into the formula for noise, sample-dominated noise scales as B_0 and SNR scales as B_0.

For any microfluidics experiment, the dominant source of noise will be due to coil resistance. Therefore, the noise is expected to be

$$N_{\text{microfluidics}} = \sqrt{\frac{4klT_c\Delta f}{p}\left(\frac{\omega_0\mu\mu_0\rho(T_c)}{2}\right)^{1/2}} \tag{2.47}$$

2.6.3 Chemical Shift

One of the powers of NMR is the resolution of different chemical species into their individual components. In practice, the resonance frequencies detected by NMR are the offsets from the transmitter frequency. These offsets take on a particular value based on their difference from a reference resonance frequency. In proton based experiments, the reference frequency is often set to the resonance of the methyl protons on either tetramethylsilane (TMS) or trimethylsilyl proprionate (TSP) due to their single sharp peak.

Chemical shift is the result of the simultaneous interaction of the spin active nucleus with an electron and that electron's interaction with the external magnetic field. From a classical perspective, the motion of an electron results in a small current that induces a small local magnetic field. This induced field either subtracts from the external magnetic field (Landau and Langevin diamagnetism) or adds to the external field (Van Vleck, Curie, Pauli, and nuclear paramagnetism) [113]. The extent to which the spin-1/2 nucleus in a specific position on a molecule is affected by the electronic motion resulting in dia- or paramagnetism is represented by the shielding factor σ. This is manifested in a perturbation on the external magnetic field giving an effective field, B_{eff},

$$B_{eff} = B_0(1 - \sigma) \tag{2.48}$$

and concurrently an effective resonance frequency, ω_{eff}, for the site specific environment

$$\omega_{eff} = \omega_0(1 - \sigma). \tag{2.49}$$

The chemical shift of the local environment is the difference in this effective resonance frequency relative to a reference frequency and is typically on the order of Hz - kHz. In order to standardize NMR experiments across field strengths, the chemical shift, δ, is typically reported in units or parts per million (ppm),

$$\delta_{ppm} = \frac{\omega_{eff} - \omega_{ref}}{\omega_{ref}} \times 10^6. \tag{2.50}$$

2.7 Magnetic Resonance Imaging

Since its inception in 1946, NMR has primarily been used by chemists to elucidate the structure of novel compounds. Then, in 1973, Paul Lauterbur applied a linear magnetic field gradient across a sample containing two 1 mm capillary tubes of water surrounded by a bath of D_2O in order to image a system that far exceeded the diffraction limit for spatial resolution using electromagnetic radiation (at 60 MHz, an RF pulse has a wavelength of $\sim$5 m) [77]. Dubbed magnetic resonance 'zeugmatography' at the time, zeugmatography developed into the field of magnetic resonance imaging (MRI).

When a magnetic field gradient is applied across a sample the magnetic field experienced by the spins is no longer solely due to the external magnetic field B_0. For a linear gradient applied along the x-axis, $\mathrm{d}G_x = \mathrm{d}B_z/\mathrm{d}x$, the contribution of the gradient field to the total magnetic field is given by $B_0 + G_x x$. Thus, the resonance frequencies of the sample are spatially dependent

$$\omega(x) = \omega_0 + \gamma G_x x. \tag{2.51}$$

2.7.1 Fourier Transform in Magnetic Resonance Imaging

In a one dimensional NMR experiment, the FT is used to convert the inductively detected signal collected in the time domain to a form more convenient for data analysis. Similarly, when a series of gradient fields are applied during an NMR experiment, the FT can be used to assign the spatially dependent resonance frequencies to positions in image space. In its spatially dependent form, the Fourier Transform is defined as

$$F(k_x) = \int_{-\infty}^{\infty} f(x) e^{-i2\pi k_x x} \, \mathrm{d}x \tag{2.52}$$

Table 2.2: MRI Fourier Transform Pairs

f(x)	**F(k$_x$)**
1	$\delta(k_x)$
$e^{\imath 2\pi k_0 x}$	$\delta(k_x - k_0)$
$\delta(x - x_0)$	$e^{-\imath 2\pi k_x x_0}$
$f\left(\frac{x}{x_{max}}\right)$	$\lvert x_{max}\rvert F(x_{max} k_x)$
$\sqcap(x) \equiv \begin{cases} 1 & \lvert x\rvert \leq 1/2 \\ 0 & \text{otherwise} \end{cases}$	$\mathrm{sinc}(k_x) \equiv \frac{\sin(\pi k_x)}{\pi k_x}$

with

$$k_x = \frac{\gamma}{2\pi} G_x \tau \tag{2.53}$$

where x is the spatial position relative to the center of the image in cm, k_x is the image frequency spectrum in units of cycles/cm, and $f(x)$ contains the valuable spatial information. If $f(x)$ is real valued, as it is when describing physical observables, $F(k_x)$ is Hermitian and $F(-k_x) = F^*(k_x)$, where $F^*(k_x)$ is the complex conjugate of $F(k_x)$. Recovery of the image of interest requires the Inverse Fourier Transform (IFT)

$$f(x) = \int_{-\infty}^{\infty} F(k_x) e^{+i2\pi k_x x}\, \mathrm{d}x. \tag{2.54}$$

A list of FT pairs that will be used for imaging experiments in this thesis is included in Table 2.2.

In Equation 2.53, the applied gradient was constant in time. Generally, the gradient can vary with time and the image frequency spectrum is given by $k_x(t) = \frac{\gamma}{2\pi} G_x(t) t$. Furthermore, magnetic field gradients are not restricted to the x-axis and can be applied in along any combination of the three principle axes. Since the axes are orthogonal, their contributions to the Fourier Transform are separable and

$$F(k_x, k_y, k_z) = \int_{-\infty}^{\infty} \int_{-\infty}^{\infty} \int_{-\infty}^{\infty} f(x, y, z) e^{-i2\pi(k_x x + k_y y + k_z z)}\, \mathrm{d}x\, \mathrm{d}y\, \mathrm{d}z \tag{2.55}$$

From Section 2.6.2, the signal received by the spectrometer will then be

$$s_r(t) = i\omega_0 B_{1xy} \int\limits_{vol} M(x, y, z) e^{-i\omega_0 t} e^{-i\gamma \int \mathbf{G}(\tau)\cdot \mathbf{r} \mathrm{d}\tau} \mathrm{d}V. \tag{2.56}$$

As before, the time dependent term $\exp(-\imath\omega_0 t)$ does not depend on space and therefore can be brought out to the front of the integral. This frequency is also mixed out before digital recording and the signal of interest is of the form

$$s(t) = i\omega_0 B_{1xy} \int\limits_{vol} M(x, y, z) e^{-i\gamma \int \mathbf{G}(\tau)\cdot \mathbf{r} \mathrm{d}\tau} \mathrm{d}V. \tag{2.57}$$

2.7.2 Slice Selection

While imaging in three dimensions is possible, it is very time consuming. Therefore, it is often advantageous to excite a slice through the sample and subsequently acquire a two-dimensional image. Typically, an RF pulse excites all of the spins in the encoding region. If instead of a static B_1 field, a time-dependent shaped pulse, $B_1(t)$, is applied in the presence of a linear gradient, a slice can be selected corresponding to a planar volume perpendicular to the gradient axis (Figure 2.7). In this thesis, $B_1(t)$ was chosen to be a sinc pulse, as an ideal sinc pulse combined with a linear gradient results in a sharp slice through image space.

In order to simplify the mathematics involved in solving for the solution to a slice selective pulse, the small tip angle ($\theta < 30°$) approximation is commonly used. By solving the Bloch Equation for $B_1(t)$ in the presence of a linear gradient, the signal equation for a slice selective experiment becomes [97]

$$s_r(t,z) = \imath M_0 e^{-\imath\omega(z)t} \int_0^t \omega_1(s) e^{\imath\omega(z)s}\, ds \tag{2.58}$$

where $\omega(z) = \frac{\gamma}{2\pi} G_z z$ and $\omega_1(t) = \gamma\, B_1(t)$ is applied on t = $[0, \tau]$. As the sinc pulse is typically symmetric about $\tau/2$, the integral in Equation 2.58 is time-shifted about this value. Using $s' = s - \tau/2$ [97],

$$s_r(t,z) = \imath M_0 e^{-\imath\omega(z)\tau/2} \int_{\tau/2}^{\tau/2} \omega_1(s' + \frac{\tau}{2}) e^{\imath\omega(z)s'}\, ds' \tag{2.59}$$

which is the IFT of the slice-selected profile multiplied by a phase factor, exp($-\imath\omega(z)\tau/2$). In order to cancel this unwanted phase, a second, re-focusing pulse is applied immediately following the excitation pulse with a total phase of $\exp(+\imath\omega(z)\tau/2)$. This is typically accomplished using a gradient of the opposite sign $(-G_z)$ for a time $\tau/2$. Then, the refocused slice through a sample using $B_1(t) = \text{sinc}\left(\frac{\gamma}{2\pi} G_z z t\right)$ results in

$$\text{sinc}\left(k_{z,max} z\right) \overset{\text{FT}}{\longrightarrow} \frac{1}{k_{z,max}} \sqcap \left(\frac{z}{k_{z,max}}\right). \tag{2.60}$$

Then, in the ideal case, a rectangular slice is selected with a thickness Δz

$$\Delta z = \frac{1}{\frac{\gamma}{2\pi} G_z \tau}. \tag{2.61}$$

In practice, sampling a finite amount of the time varying signal leads to deviations from the ideal rectangular selection. Furthermore, the mathematics presented above use a small tip angle approximation, although the theory generally supports experimental application for pulses up to 90° [97]. Modeling large tip angles is cumbersome and for this reason, developing pulses that accurately select the spins of interest at large tip angles (eg. 180°) remains an active area of research.

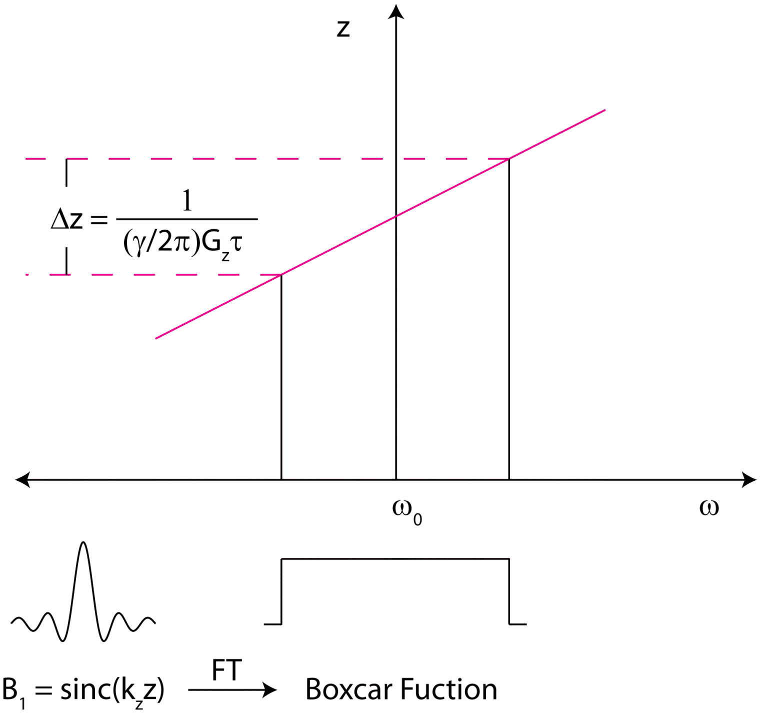

Figure 2.7: Slice Selection. Application of a sinc pulse in the presence of a linear gradient results in a rectangular slice through image space.

2.7.3 Common Magnetic Resonance Imaging Pulse Sequences

While many pulse sequences are used in MRI, only a few of the more common techniques will be used throughout this thesis. These sequences - gradient echo imaging, spin echo imaging, and chemical shift imaging - will be reviewed briefly here.

Gradient Echo Imaging

With any MRI experiment, application of a gradient pulse leads to accumulation of phase, ϕ, where

$$\phi(x, y, z, t) = \gamma \int_0^t \mathbf{G}(\tau) \cdot \mathbf{r}\, d\tau \tag{2.62}$$

If a series of pulses of opposite amplitude are applied, the total phase at time $t = \tau$ will sum to zero and a gradient echo occurs. This time is commonly referred to as the time to echo (TE) in imaging applications. In this sequence, a slice selective pulse excites spins within a defined area followed by the x- and y- gradients for a constant time t_y. Once the y-gradient is turned off, data acquisition begins in the presence of the x-gradient. For this reason, the x-gradient is dubbed the *readout* gradient.

This process reads out an entire line in k-space for each increment of t_y. Subsequent acquisitions step through G_y in order to readout lines covering all of k-space. The incremented gradient G_y is commonly referred to as the *phase encoding* gradient.

Spin Echoes in Imaging

In Section 2.5.2, a pulse sequence was described that produces a spin echo at a time $t = 2\tau$. Accumulation of phase $\phi(x, y, z, \tau^-)$ prior to the 180 pulse leads to a phase $\phi(x, -y, -z, \tau^+)$ following application of a pulse along the x-axis. In a slice selective experiment, the signal equation is given by [97]

$$s_r(\tau^+) = \int_x \int_y m(x, y) e^{-\imath\pi} e^{+\imath 2\pi [k_x(\tau)x + k_y(\tau)y]} e^{+\imath\omega_{ext}(x,y)\tau}\, dydx. \tag{2.63}$$

where $k_{x,y} = \frac{\gamma}{2\pi} G_{x,y}\tau$ and $\omega_{ext}(x, y)\tau$ is the phase acquired due to the local field inhomogeneities.

In an imaging experiment, the application of a 180 degree pulse transforms the position of a magnetization vector in k-space to its conjugate in the imaging frequency spectrum. A spin echo is typically timed to cross the k_y axis at $k_{x,y} = 0$ so that the phase accumulated is equal to zero at the origin in k-space. Unlike the gradient echo pulse sequence, both lobes of the applied gradients are positive due to the application of the 180 degree pulse.

Spin echo imaging pulse sequences have advantages and disadvantages over gradient echo images. Due to the application of a 180 degree pulse, magnetic field inhomogeneities are refocused at the peak of the echo. In general, adding a spin echo provides a way of generating T_2 constant in an image. The disadvantage of a spin echo pulse sequence is that 180 degree pulses are hard to apply homogeneously across a sample leading to imperfect refocusing and the potential for image distortion.

Chemical Shift Imaging

Chemical shift imaging is a combination of spatial and spectral imaging, where the goal is either to obtain an NMR spectrum at each spatial position or equivalently to display an image of each chemical species. In gradient echo and spin echo imaging, chemical shift is largely ignored as the image is indirectly integrated over all frequencies within the sample. When considering chemical shift, by definition the desired image depends on frequency $m(x, y, f)$ and the signal equation becomes

$$s_r(t) = \int_x \int_y \int_f m(x, y, f) e^{-\imath 2\pi (k_x(t)x + k_y(t)y + k_f(t)f)}\, df dydx \tag{2.64}$$

where f is the chemical shift offset frequency (Ω from before) with respect to the Larmor frequency f_0 and $k_f(t) = t$.

To form a two dimensional chemical shift image, k_x, k_y, and $k_f = t$ are used in a three dimensional FT reconstruction. The result is a 2D image with the third axis corresponding to chemical shift. Typically, phase encoding is performed in both the x and y directions followed by readout in the absence of gradients. Due to the nature of collecting data voxel by voxel, the downside of chemical shift imaging is that it is inherently slow. For an $N \times N$

image, the $k_x - k_y$ plane is sampled using N^2 points. When including the time required to obtain an individual experiment (TR), the total scan time is N^2TR. A trade-off between spatial resolution and time is typically made with chemical shift images to acquire data for low concentration samples in a smaller number of scans, but with poorer spatial resolution.

2.8 Remote Detection Nuclear Magnetic Resonance Spectroscopy and Imaging

Remote detection NMR (RDMR) spectroscopy and imaging is a technique that was developed in 2003 to separate the encoding and detection of the nuclear spins [94]. This technique is particularly well suited to sensitively detect chemical information in samples where the encoded spins fill only a small fraction of the volume of the encoding coil (e.g. porous bead packs and microfluidic chips). For any RDMR experiment, the primary requirement is that the gas or liquid can flow through the region of interest where the spins are encoded to an optimized detection region without significant T_1 relaxation. RDMR capitalizes on the vast number of encoding possibilities offered by NMR spectroscopy to gain chemical information about a system in its native environment while avoiding the low sensitivity of NMR detection in these regions due to the poor filling factor. Furthermore, valuable information can be obtained by analyzing the chemical species of interest as a function of the time from initial encoding through the completion of the experiment (time-of-flight, TOF).

In the first demonstration of RDMR, the authors separated encoding of hyperpolarized xenon gas flowing through porous aerogel crystal fragments in a low magnetic field (4-7 mT) from the detection of the gas in a high magnetic field magnet (4.2 T) [94]. This experiment allowed encoding of the xenon gas as it flowed through a setup that was not constrained by the geometry of the high-field magnet while taking advantage of the long T_1 of xenon in the gas phase and the increased SNR achieved by detecting at an increased field strength. Hyperpolarized xenon gas was then imaged as it flowed through a Kel-F cylinder with CAL hollowed out along the axial dimension [119]. In this experiment, both encoding and detection of the xenon gas were performed within a 7 T magnet in order to minimize the flow path between the two regions. Features on the imprinted cylinder were resolved at 0.7 mm thickness even though the hyperpolarized gas only filled 12.5% of the encoding region. Continuing the work with hyperpolarized xenon gas, McDonnell, et al. developed a probe to remotely detect the flow of xenon gas through a microfluidic chip [88]. In 500 transients, a 1% xenon gas mixture flowing at 0.3 SLM at 1 atm, 23 °C was detected with an SNR of 12.7. Furthermore, RDMR was used to interrogate the porous structure of Bentheimer sandstone rock using hyperpolarized xenon gas [50] and diffusion of xenon gas across a permeable membrane was imaged with this technique in order to circumvent the low filling factor of the sample membrane holder [131].

While the original remote detection experiments were conducted using hyperpolarized xenon gas as the probe nucleus, recent RDMR experiments have focused on the detection of water protons flowing through microfluidic chips. In 2005, Wensink, et al. used a planar microcoil to detect the formation of an imine Shiff base from the reaction of benzaldehyde with aniline in a 56 nL sample volume at 1.4 T [142]. The mixing of miscible solvents such as 0.5 mM $MnSO_4$ in water and deionized water [6] and immiscible solvents such as acetonitrile and benzene [59] have been resolved both spectroscopically and tracked through time in an imaging experiment. In the immiscible imaging experiment, information about flow through the microfluidic chip was collected for both solvents simultaneously by acquiring spectra that contained all of the proton chemical shifts. The resulting images could then be processed to assess the flow of either acetonitrile, benzene, or both solvents combined.

In addition to position and time-of-flight information, the velocity of a solvent can be tracked as the fluid flows through a microfluidic chip [101] or a porous bead pack [54]. Then, when the path of the fluid flow is known, data analysis techniques such as compressed sensing can be used to drastically reduce the amount of data necessary to acquire to obtain high resolution images [10]. Most recently, Teisseyre, et al. used remote detection techniques to monitor the chromatographic separation of small molecules in two dimensions on a novel monolith column [130].

2.8.1 Remote Detection Pulse Sequence

All of the experiments described above share similar pulse sequence details where the chemical species of interest is initially encoded, stored along the longitudinal axis during transfer to the detection region and then detected with an optimized coil. For the remote detection experiments conducted in this thesis, nuclei are initially encoded with a commercially available 30 mm dually tuned (^{1}H/^{129}Xe) probe (Figure 2.8A). For a typical microfluidic chip, the filling factor for half the volume of the channels relative to the total volume of the coil is on the order of 1%. Following encoding of the spins, the signal is then stored along the longitudinal axis so that the magnetization decays with T_1 relaxation as opposed to the much faster T_2^* time constant (Figure 2.8B). The encoded information is then stroboscopically detected using a series of 90 degree pulses with a solenoid coil to obtain time-of-flight information (Figure 2.8C). The individual FIDs are then Fourier Transformed, the spectra are integrated, and the resulting signal amplitude is plotted as a function of time following the application of the storage pulse.

2.8.2 Sensitivity Gain with Remote Detection

Granwehr and Seeley presented a comprehensive analysis of the sensitivity gain afforded by remote detection of nuclear spins over direct detection of the system [51]. Briefly, the ratio of the SNR for the encoding (direct, d) versus the detection (remote, r) coil must first be considered. This value (Λ) is defined as the ratio of the 90 times for two coils

$$\Lambda = \frac{t_{90}^d}{t_{90}^r} = \sqrt{\frac{K_r Q_r \omega_0^r / \tau_r V_c^r}{K_d Q_d \omega_0^d / \tau_d V_c^d}} \tag{2.65}$$

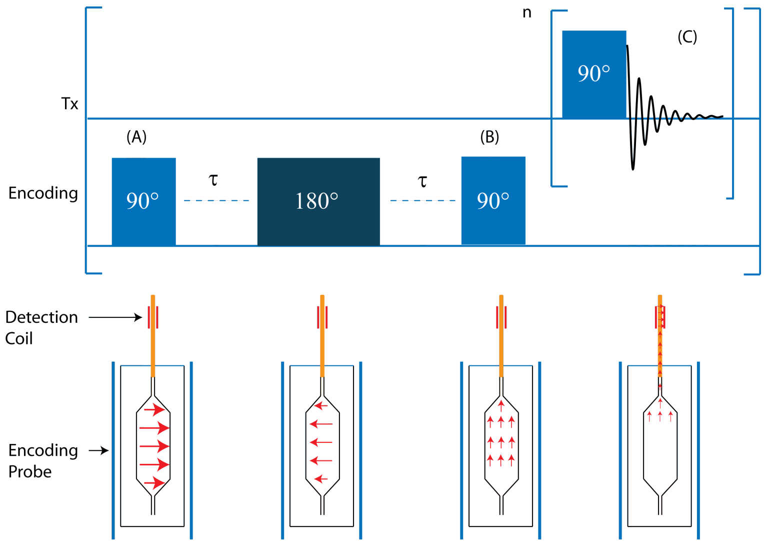

Figure 2.8: Remote Detection Pulse Sequence. A) A 90 degree pulse is used to excite nuclei within the encoding region. The excited spins can then be manipulated according to the experimental specifications. B) The excited spins are then stored along the longitudinal axis for transport to the detection region. C) The system is stroboscopically detected with a series of n 90 degree pulses.

where K is a numerical factor that is dependent on the geometry of the coils, Q is the quality factor for the coils, ω_0 is the resonance frequency, τ is the repetition time between subsequent acquisitions, and V is the volume of the coil. For the experiments conducted in this thesis, Λ is typically on the order of 150. Then, for a remote detection experiment where the volume of the coil matches the volume of the sample, the ratio of sensitivities for the remotely detected versus directly detected experiment is given by

$$\begin{aligned} \left[\frac{\Psi_r}{\Psi_d}\right] &\approx \frac{\Lambda}{\sqrt{2}}\sqrt{\frac{T_2^r}{2t_d^{max}}} \quad \text{if } t_r^{max} > T_2^r \\ \left[\frac{\Psi_r}{\Psi_d}\right] &\approx \frac{\Lambda}{\sqrt{2}} \quad\quad\quad\quad \text{if } t_r^{max} \ll T_2^r \end{aligned} \tag{2.66}$$

where Ψ is the sensitivity of the coil, Λ is the ratio of SNR for the coils given in Equation 2.65, T_2 is the spin-spin relaxation time constant, and t is the acquisition time for each collected FID. The first line in Equation 2.66 is a good approximation for continuous flow experiments, while the second line can be used for a stopped flow experiment. Thus, the total sensitivity gain scales roughly as $\Lambda/\sqrt{2}$.

In Equation 2.66, the sensitivity gain was considered for the case when the coil volume was designed to match the sample volume. While ideal for increased sensitivity, this does not allow for the acquisition of time-of-flight information. The ratio of sensitivities for detection of nuclear spins in each TOF data acquisition (t) versus the volume-matched remote detection experiment (r) is given by

$$\left[\frac{\Psi_t}{\Psi_r}\right] \approx \lambda\sqrt{\frac{\tau_r}{2nT_2^r}} \tag{2.67}$$

where λ is the SNR sensitivity ratio for the TOF and full remote detection coils, τ_r is the total repetition time split into n steps, and T_2^r is the spin-spin relaxation time constant for this system. If the sum of the signals and the relative noise are added to generate the full TOF image,

$$\left[\frac{\Psi_t}{\Psi_r}\right] \approx \frac{\lambda}{n}\sqrt{\frac{\tau_r}{2T_2^r}}. \tag{2.68}$$

Thus, for $\lambda \sim 1$, the trade-off for acquiring TOF information in n steps is a hit in sensitivity that scales rough as $1/n$.

2.8.3 Optimized Detectors

In this thesis, a solenoid coil was chosen as the optimized detector as all of the experiments were conducted using a high-field (7.05 T) magnet. Hoult and Richards eloquently compared the performance of two common inductive detectors: saddle coils and solenoids [64]. They found that the sensitivity for inductive detection with a solenoid coil is three times better than detection with a saddle coil in the limit of coil dominated noise. Furthermore, for a solenoid coil, $B_{1,xy}$ is given by

$$B_{1,\mathrm{xy}} = \frac{\mu_0 n}{2}\frac{1}{(a^2+g^2)^{1/2}} \tag{2.69}$$

where μ_0 is the permeability of free space, n is the number of turns in the coil, a is the radius of the coil, and $2g$ is the length of the coil. Since $a \approx g$ in a typical solenoid coil used the these experiments, $B_{1,\mathrm{xy}} = 0.354n\mu_0/a$. In this limit, the sensitivity (Ψ) is then

$$\Psi = \frac{B_{1,xy}}{\sqrt{R_c}} \tag{2.70}$$

$$= \frac{0.354n\mu_0^{3/4}}{a\left(\frac{\omega_0\mu\rho(T_c)}{2\pi^2}\right)^{1/4}} \tag{2.71}$$

where R_c is given by Equation 2.44 for $l = 2a$ and $p = 2\pi a$. Therefore, the sensitivity of the solenoid coil increases as the number of turns increases and as the radius of the coil decreases.

The majority of remote detection experiments to date have used solenoids for inductive detection due to their homogeneity and sensitivity at high magnetic fields, but the true power of RDMR is that this detector can be flexibly designed to achieve the highest SNR upon detection. Planar RF microcoils can be used in RDMR experiments at high magnetic fields [133] while an array of low-field detectors including super conducting quantum interference devices (SQUID) [146], anisotropic magnetoresistive (AMR) devices [135], and atomic magnetometers ([147], [79]) have been employed. With the exception of RF microcoils, all of these alternative detectors have the potential to be used extensively as portable, low-field experiments come in higher demand.

Chapter 3

Nuclear Magnetic Resonance with Xenon-129

Xenon was first discovered by William Ramsay and Morris Travers in 1898 by the residue it left behind following evaporation of all other components in air [32]. Named after the greek word for 'stranger', xenon is an inert noble gas that takes its place in the 54^{th} position on the periodic table and exists in 9 stable isotopes. Of particular interest for NMR and MRI experiments is the NMR active spin-1/2 isotope, xenon-129, that is in 26.4% natural abundance. Xenon does not naturally react with analytes in solution due to its filled outer electron shell although its highly polarizable electron cloud leads to significant, yet non-destructive chemical interactions with molecules in solution [32]. Unlike traditional protons used for imaging, xenon only exists in trace concentrations in the body. Perturbations of the nuclear spin are therefore induced on the relatively small population of gas atoms that are administered in an experiment, but these can lead to large MR signal contrast.

Qualities of xenon that make it particularly attractive for use as a probe in the combinatorial screening experiments proposed in this thesis include its solubility in aqueous environments, the ability to enhance the polarization of its spin-1/2 nucleus, and the ability to functionalize it through the use of host-guest interactions. Solubility, spin-exchange optical pumping, methods for dissolving xenon into water, and clinical applications of xenon-based NMR will be discussed below followed by a discussion of functionalization of xenon for targeted molecular imaging in Chapter 4.

3.1 Solubility of Xenon

For a gas, xenon has exceptional solubility in water. The CRC defines the amount of 1 atmosphere of xenon in water to be given by [47]:

$$\ln X_1 = A + B/T^* + C\ln T^* \tag{3.1}$$

where X_1 is the solubility or mole fraction of xenon in water, $T^* = \mathrm{T}/100$ for the temperature T in Kelvin, and the constants are empirically defined to be A = -74.7398, B = 105.210, and C = 27.4664. Using Equation 3.1, the mole fraction of xenon in water is 7.890×10^{-5} at

Table 3.1: Mole Fraction of 1 atmosphere Xenon Dissolved into Various Solvents

Solvent	**Mole Fraction**	**Temperature (°C)**
Water	9.051×10^{-5}	20
Water	7.890×10^{-5}	25
Water	5.955×10^{-5}	37
Cyclopentane [105]	2.27×10^{-2}	20
Cyclopentane [105]	2.09×10^{-2}	25
Cyclohexane [105]	2.20×10^{-2}	20
Cyclohexane [105]	2.05×10^{-2}	25
Cyclooctane [105]	2.19×10^{-2}	20
Cyclooctane [105]	2.05×10^{-2}	25
Cyclooctane [105]	2.19×10^{-2}	20
Formic acid [105]	7.14×10^{-4}	20
Acetic acid [105]	4.05×10^{-3}	20
Propanoic acid [105]	8.18×10^{-3}	20
n - Butanoic acid [105]	1.09×10^{-2}	20
n - Pentanoic acid [105]	1.27×10^{-2}	20
n - Heptanoic acid [105]	1.61×10^{-2}	20
Propanal [105]	8.41×10^{-3}	20
n - Butanal [105]	1.15×10^{-2}	20
n - Pentanal [105]	1.37×10^{-2}	20
n - Heptanal [105]	1.70×10^{-2}	20

298.15 K and 5.955×10^{-5} at 310.15 K. In general, the solubility for the noble gas decreases as the system temperature increases. Furthermore, due to the hydrophobic nature of xenon, its solubility increases as the hydrophobicity of the solvent increases as can be seen from the empirically determined solubilities referenced in Table 3.1.

Instead of evaluating solubility as the mole fraction of xenon dissolved in solution, it is often more straightforward to consider the Ostwald coefficient for xenon in an environment. This environment is not restricted to solvents (e.g. water), but can be determined for suspensions (e.g. red blood cells). The Ostwald coefficient is defined to be the ratio of the volume of xenon gas absorbed into a volume of liquid at one atmosphere. In accordance with the mole fraction of xenon in solution, the Ostwald coefficient decreases at increased temperatures and increases in hydrophobic environments (Table 3.2). Furthermore, the solubility of xenon in water is put into perspective as its Ostwald coefficient of 0.11 at 25°C is 7.4 times higher than diatomic nitrogen (0.0149 [98]) and 11.7 times higher than helium (0.00939 [144]) at the same temperature.

Table 3.2: Ostwald Coefficients. This table presents the solubility of xenon in a specified environment by its Ostwald Coeffient, or the volume of xenon gas relative to the volume of absorbing liquid.

Solvent	**Ostwald Coefficient**	**Temperature (°C)**
Water [32]	0.11	25
Water [32]	0.08	37
Hexane[32]	4.8	25
Benzene [32]	3.1	25
Fluorobenzene [32]	3.3	25
Carbon disulphide [32]	4.2	25
Dimethyl sulfoxide (DMSO) [32]	0.66	37
Saline [32]	0.09	37
Plasma [32]	0.10	37
Oil [32]	1.9	37
Intralipid (20%) [32]	0.4	37
Perflubron (PFOB) [32]	1.2	37
Erythocytes (98%) [32]	0.20	37
Human albumin (100%, extrapolated) [32]	0.15	37
Blood [32]	0.14	37
Fat tissue [32]	1.3	37
Pure gray matter [31]	0.135	37
Pure white matter [31]	0.224	37

Using Equation 3.1, the concentration of xenon in water, $[\mathrm{Xe}]_w$, is calculated from

$$[\mathrm{Xe}]_w = (\mathrm{pXe}) \left(\frac{P + 14.7}{14.7} \right) [\mathrm{H_2O}] X_1 \tag{3.2}$$

where pXe is the percentage of xenon the in gas mixture, P is the over-pressure of the gas mixture in psig, $[\mathrm{H_2O}]$ is the concentration of water, and X_1 is the solubility of xenon in water at one atmosphere for a given system temperature. For a typical experiment conducted in this thesis, pXe = 0.02, P = 60 psig, and T = 20 °C resulting in 511 μM xenon in water. Other values of interest include the same gas mixture and pressure at 25 °C (446 μM) and 37 °C (337 μM). Relative to protons at 110 M, xenon-based NMR experiments inductively detect signal from a very small number of spins. If more signal is required, it can be obtained by increasing the percentage of xenon in solution (expensive!), increasing the over-pressure of the gas mixture (limited by experimental design), or decreasing the system temperature (sample limited). As mentioned above, the solubility of xenon increases in hydrophobic solvents. Therefore, if the samples can tolerate hydrophobic solvents, the initial signal can also be increased in this way.

3.2 Laser-Polarized Xenon-129

Until the mid-1990s, clinical MR research had focused on detecting differences in the proton Larmor resonance frequency. In addition to the added RF hardware considerations, this thermal magnetization of the proton signal exceeds that of xenon by a factor of 10^4 (enriched, gaseous xenon-129), 10^5 (enriched, aqueous xenon-129), or 10^6 (aqueous xenon at a natural abundance of xenon-129).

As in Equation 2.5, the initial magnetization is $M_0 = \frac{1}{2} N_s \gamma \hbar P$, where γ is the gyromagnetic ratio, $\hbar$ is Planck's constant divided by 2π, N_s is the number density of spins in the detection region, and P is the polarization of the sample. With the exception of void spaces such as the lungs where there are only very low concentrations of protons, the initial magnetization of water protons is very much larger than thermal xenon magnetization for each of the variables in Equation 2.5. First, at 42.576 MHz/T, the gyromagnetic ratio of protons is approximately 4 times the gyromagnetic ratio of xenon at -11.777 MHz/T. Then, at 37°C and 7 T, thermal polarization as described in Chapter 2 of water protons is approximately $2.5 * 10^{-5}$ or 25 parts per million, while the thermal polarization of xenon is approximately 6 parts per million. Water protons are at a concentration close to 110 M under natural conditions, while at 37°C, the solubility of xenon in water at 1 atmosphere is 3.3 mM. Finally, the natural abundance of the spin-1/2 active nucleus is 99.99% for ^{1}H relative to 26.4% for ^{129}Xe. Therefore, the ratio of initial magnetization for water protons to aqueous xenon is

$$|M_{0,\mathrm{H}}/M_{0,\mathrm{Xe,na}}| \approx 2 * 10^6 \tag{3.3}$$

$$|M_{0,\mathrm{H}}/M_{0,\mathrm{Xe,enr}}| \approx 5 * 10^5 \tag{3.4}$$

where $M_{0,\mathrm{H}}$ is the initial magnetization of water protons, $M_{0,\mathrm{Xe,na}}$ is the initial magnetization of aqueous xenon using a gas mixture with a natural abundance of xenon-129, and $M_{0,\mathrm{Xe,enr}}$ is the initial magnetization for aqueous xenon using a gas mixture enriched to 100% xenon-129. The, given an Ostwald coefficient of 0.08 for xenon dissolved in water at 37°C, the ratio of initial magnetization water protons relative to gaseous xenon is approximately $1.6{*}10^5$ for natural abundance xenon or $4{*}10^4$ for an enriched sample.

Detecting thermal xenon dissolved in water is impractical due to the time it would take to collect this data. In order to overcome the low initial magnetization at thermal equilibrium, spin exchange optical pumping is used to increase the polarization of xenon to 2-5%. With this technique, the initial magnetization of xenon approaches that obtained for water protons, making experiments using hyperpolarized xenon viable.

3.2.1 Spin Exchange Optical Pumping

Spin exchange optical pumping (SEOP) has been used for the past two decades to enhance the polarization of noble gases such as xenon and helium for use in exotic NMR and atomic magnetometry studies. This technique relies on creating a non-equilibrium population of electronic spins and transferring the resulting polarization to the nuclei of interest. Non-equilibrium populations of atomic ground and excited states were first introduced by Kastler in 1950 [69] - work for which he was granted the Noble Prize in Physics in 1966. SEOP was re-introduced by William Happer in the 1970s [57] since which time magnetic resonance studies with xenon-129 and helium-3 have been developed. The theory and applications of spin exchange optical pumping in the context of magnetic resonance experiments have been reviewed by many authors ([136], [49],[15]) and are briefly presented below.

In SEOP, a laser tuned to the D1 transition of the valence electron of an alkali metal is used to drive the selective population of one of the ground spin states thereby creating a population imbalance relative to thermal equilibrium. This electronic polarization is then transferred to the nucleus of the noble gas via hyperfine interactions. In theory, any alkali metal can be used to optically pump noble gases, but traditionally rubidium or cesium are used due to their high vapor pressures and the accessibility of diode lasers to drive the electronic transition of the ground state electron to its first excited state. For the remainder of this section, the alkali metal is assumed to be rubidium and the noble gas is assumed to be xenon.

3.2.2 Optical Pumping

Alkali metals are used in optical pumping experiments because their ground state is spherical (s shell), the valence electron is easily polarized because there is only one transition available, lasers operating at the D1 transition wavelength are readily available, and the number density of atoms in a vapor is large at relatively low temperatures. To prepare for SEOP, an optical cell is scrubbed of paramagnetic impurities, often coated with silane to reduce collisions of the vapor atoms with the wall, filled with roughly 1 gram of rubidium

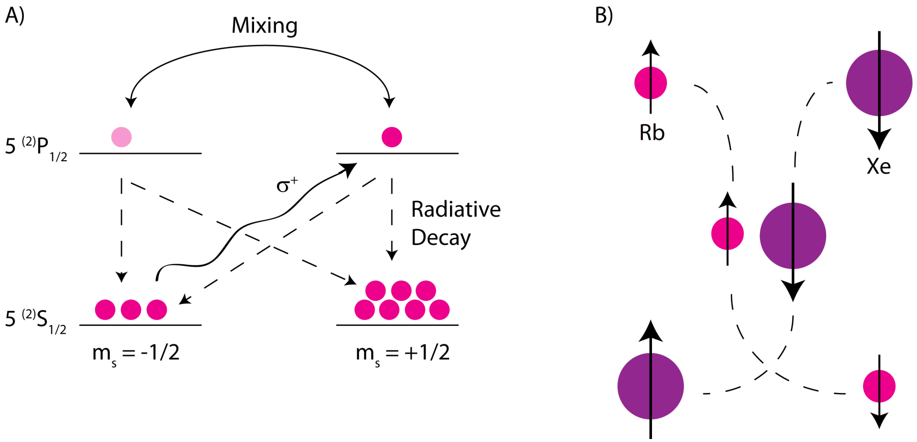

Figure 3.1: Spin Exchange Optical Pumping. A) Optical pumping of the valence electron of rubidium is achieved by selectively driving its D1 transition with circularly polarized light. B) Spin exchange via hyperfine interactions transfers the polarization from the valence electron on the rubidium atom to the nucleus of xenon.

metal, and heated to 80 - 130 °C to ensure a sufficient vapor pressure of the alkali metal [136]. This cell is then placed in a small magnetic field, typically 10 - 100 gauss, to lift the degeneracy of the $m_s = \pm\frac{1}{2}$ spin states. High power, left-circularly polarized light tuned the D1 transition of rubidium at 794.7 nm is focused on the heated cell containing the rubidium vapor. A photon, containing +1 units of angular momentum, excites an electron from the $m_s = -1/2$ ground state to the $m_s = +1/2$ level of the first excited state (Figure 3.1A). While in the first excited state, collisions between the electron and other gas molecules allow for transitions between the $m_s = \pm 1/2$ states effectively mixing the two states. In time, the electron decays back into the ground state with a probability of decay given by [49]

$$\omega_\gamma = \frac{3}{\left(3 + 7.5\frac{p_{N_2}}{kPa}\right)} \tag{3.5}$$

where p_{N_2} is the partial pressure of nitrogen gas in the buffer in units of kPa [49]. Over time, the continuous cycle driving transitions from the $m_s = -1/2$ ground state to the $m_s = +1/2$ first excited state will result in many more ground state electrons with $m_s = +1/2$. This non-equilibrium population creates an electron spin polarization of the rubidium vapor, P_{Rb}, is given by [49]

$$P_{Rb} = \frac{\rho_{OP}}{\rho_{OP} + \rho_{SD}} \tag{3.6}$$

where ρ_{OP} is the rate at which the rubidium vapor becomes polarized via optical pumping and ρ_{SD} is the spin relaxation rate of the alkali metal atoms. This electronic polarization is typically on the order of 90-95%.

3.2.3 Spin Exchange

Polarization of the valence electron of rubidium is ultimately transferred to the xenon nucleus through collisional hyperfine interactions (Figure 3.1B). At the multiatmospheric pressures used in this thesis, collisions are thought to be through two-body interactions [136] where polarization exchange is described by [49]

$$\alpha \mathbf{S} \cdot \mathbf{I} = \frac{\alpha}{2}[S_+ I_- + S_- I_+] + \alpha S_z I_z \tag{3.7}$$

where S is the electron spin, I is the nuclear spin, and α is the probability of finding an unpaired electron at the nucleus given by

$$\alpha = \frac{8\pi}{3}\gamma_S \gamma_I \hbar^2 \delta(r) \tag{3.8}$$

where $\gamma_{S,I}$ are the gyromagnetic ratios of the electron (S) and nucleus (I), $\hbar$ is Planck's constant divided by 2π, and $\delta(r)$ is the Dirac delta function depending on the relative distance r between the electron and the nucleus.

Given the rubidium electron polarization (P_{Rb}) from Equation 3.6, the total nuclear polarization, P, following optical pumping for a time, t is given by

$$P = \frac{\rho_{SE}}{\rho_{SE} + \rho_0} P_{Rb}[1 - e^{-(\rho_{SE}+\rho_0)t}]. \tag{3.9}$$

where ρ_{SE} the rate of spin exchange between the xenon and rubidium electron and contributions to the longitudinal relaxation are reflected in ρ_0. Xenon nuclear polarizations of 2-5% are typically obtained with the hyperpolarizers used in the Pines lab. Xenon polarization of 14-16% can be obtained on a similar homebuilt polarizer when the rubidium cell temperature is closely regulated and monitored (personal communication with Leif Schröder) and can achieve a commercial record of 69% using a continuously recirculating system by William Hersmann at the University of New Hampshire ([112], [75]).

The buffer gases contained in the xenon gas mixture are important when optically pumping xenon. Nitrogen is typically added to quench the energy before it can be released in radiative decay, dissipating the energy within the many vibrational levels available in the N_2 molecule. Without nitrogen present in the system, the randomly polarized energy released by the excited electrons would re-equilibrate the polarized ground state. Additionally, helium gas is added to pressure broaden the laser profile so that the alkali metal hyperfine structure is unresolved.

In this thesis, the working gas mixture is 1-2% natural isotope abundance xenon, 10% nitrogen, with a balance of helium. The price of the xenon gas mixture increases substantially as 1) the percentage of xenon is increased and 2) the percentage of Xe-129 is increased. At the time this thesis was written, the cost of a gas cylinder containing approximately 50 liters of 2% of natural abundance xenon, 10% nitrogen, 88% helium was $2250 or $3950 depending on the purchasing agreement. While $45 - $79 per liter of this 2% xenon gas mixture is expensive, the price for helium-3 continues to rise due to its diminishing production as a byproduct of tritium decay. While it is possible to achieve higher polarization with helium-3, the process takes longer due to its smaller collisional cross-sectional area and the rising cost and scarcity of the gas make developing MR techniques utilizing Xe-129 especially interesting.

3.2.4 Commercial Xenon Hyperpolarizers

Hyperpolarization of xenon is practically achieved with either a home-built polarizer or on with one of a few commercial products. In 1996, Magnetic Imaging Technologies Incorporated (MITI) was spun-out of the William Happer lab at Princeton University, taking with it the extensive knowledge of spin-exchange optical pumping from its founding lab [100]. After refining its product for the polarization of ^{3}He ($>$ 35%) and ^{129}Xe (5-7%), MITI was bought by Nycomed Amersham in 1999 during which time FDA approval was sought for clinical studies using hyperpolarized ^{3}He. MITI was later acquired by General Electric in 2004 at which time the focus changed from hyperpolarized ^{3}He to ^{129}Xe. During this last acquisition, GE also obtained the rights to the original Princeton patent. To date, a commercial xenon hyperpolarizer has not come out of the labs at GE.

An alternative hyperpolarizer was developed in the William Hersman lab at the University of New Hamphire. In this model, the noble gas is flowed towards the laser light used for spin exchange optical pumping [100]. By recirculating the xenon gas mixture through a cell under optimized flow conditions, this polarizer is capable of hyperpolarizing ^{129}Xe to 69% [75]. While capable of achieving enormous polarizations, the Hersmann polarizer has not been used extensively due to continued patent battles with GE.

Unless otherwise noted, all of the experiments conducted in this thesis used an Amersham MITI polarizer.

3.3 Dissolution of Xenon

Three methods commonly used to dissolve xenon into water are: batch-mode, bubble-mode, and continuous flow. In batch-mode experiments, hyperpolarized xenon gas is collected in a cold finger directly following spin exchange with the polarized rubidium vapor. The cold finger is kept within the field of a permanent magnet in order to preserve spin order and is submerged in liquid nitrogen to freeze out hyperpolarized xenon while allowing the nitrogen and helium to pass through. Batch-mode collection of hyperpolarized xenon typically takes 30 - 45 minutes [81] after which the cold finger is evacuated of any remaining gases. The frozen hyperpolarized xenon has a T_1 hours [46] and can be stored in this form until required for use. Xenon-based NMR experiments are then conducted by either adding a chip of frozen hyperpolarized xenon to a de-gassed sample, adding an over-pressure of hyperpolarized gas to a de-gassed sample, or injecting a sample with pre-dissolved xenon in solution. The samples are then quickly mixed and inserted into the magnet for immediate data collection as the T_1 of xenon in water is approximately 60 seconds [16].

Although high signal-to-noise ratios can be achieved by using batch-mode polarization, experiments are limited to signal shot data acquisition or sacrificing SNR for obtaining multiple acquisitions within the lifetime of the hyperpolarized signal. Additionally, the benefits of acquiring multiple averages for the same sample cannot be obtained with this method. In 2005, Han, et al. devised a way to efficiently bubble xenon into water [55]. In bubble-mode experiments, hyperpolarized xenon gas is transported directly from the hyperpolarizer to a modified NMR tube containing an inlet port through which xenon gas can flow through capillary tubing into a sample and an outlet port through which the gas mixture can exit the system (Figure 3.2A). In the Pines lab, the distance from the MITI hyperpolarizer to the NMR tube is 2 - 3 m. Then, for a typical gas flow rate of 0.45 SLM, the time for xenon gas to reach the sample through 1/8 inch tubing is approximately 0.5 seconds. When a pressure gradient is created across the sample, the gas mixture will bubble homogeneously through the sample. Over time, typically 15 - 20 seconds for the experiments presented in Chapters 5 and 8, the sample is saturated with xenon gas. If this pressure gradient is then eliminated, the flow of xenon gas will stop, bubbles will settle, and an FID can be acquired. The process of bubbling xenon into solution, bypassing the gas flow around the sample, waiting for bubbles to settle, and acquiring data will furthermore be referred to as 'stopped-flow' data collection. Experiments utilizing stopped-flow data collection gain the advantages of reduced shot-to-shot noise, full signal acquisition via 90 degree pulses, and same sample signal averaging relative to batch-mode data collection. Furthermore, the total time to acquire experiments is reduced due to the elimination of the long polarization cycle required with batch-mode experiments.

Finally, the act of bubbling xenon directly into the sample can be eliminated if the sample is compatible with a continuous flow of water. In the original application of continuous flow mode [62], hyperpolarized xenon gas was bubbled into solution directly above an NMR phantom specifically designed for liquid flow compatibility. Over the course of doing the work described in this thesis, this setup was replaced by dissolution of xenon gas into solution using hydrophobic gas exchange membranes obtained from Membrana®([114], [152]). In either a commercial cassette (Membrana Micromodule®) or with a home-built gas exchange system (Chapter 6), xenon gas flows counter to the direction of fluid flow in order to maximally saturate the fluid with hyperpolarized xenon (Figure 3.2B). Furthermore, by keeping the pressure of xenon gas below the pressure of the fluid, xenon gas dissolves into solution without the formation of bubbles. A direct comparison of the signal-to-noise ratio for xenon bubbled into solution versus delivered via hydrophobic membranes shows that saturating a solution via bubbling results in four times the SNR for membrane dissolution [114]. While using hydrophobic membranes in continuous flow systems is less efficient than bubbling xenon directly into the solution, this method is advantageous in systems where physical space restricts the accessibility of full bubbling systems.

3.4 Xenon Chemical Shift

The chemical shift range of xenon is extensive due to its highly polarizable electron cloud. Relative to the 14 ppm chemical shift range typical for protons, xenon's chemical shift range

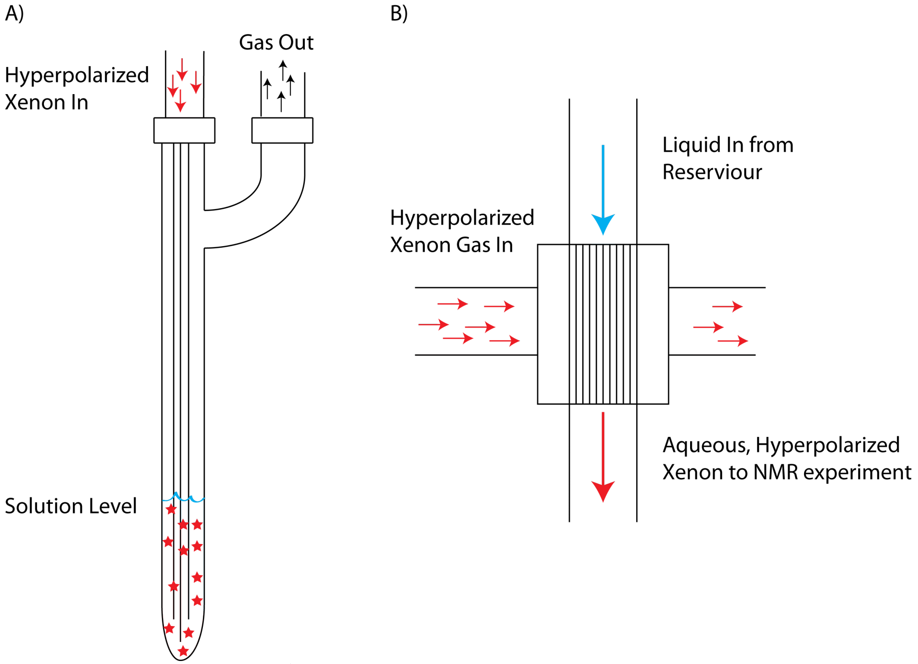

Figure 3.2: Xenon Dissolution. A) Bubble-mode dissolution is achieved by delivering hyperpolarized xenon gas to a sample through capillary tubing. The outlet arm can either be open to atmospheric pressure creating a pressure gradient across the sample or closed to stop the flow of xenon gas. B) Continuous flow mode is achieved by flowing xenon gas orthogonal to liquid flowing through hydrophobic membranes. If the pressure of gas is lower than the pressure of liquid, the gas will dissolve into the liquid without bubbling.

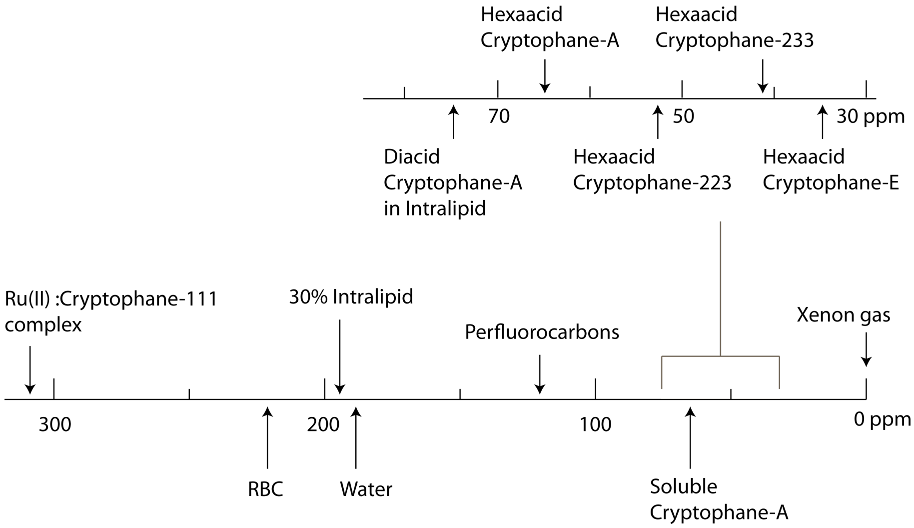

Figure 3.3: Xenon Chemical Shift in Aqueous Environments. The chemical shift for xenon in the reported solvents and aqueous cryptophane cages are taken from references [116], [16], [134], [92], [66], [40].

extends to 216 ppm for dissolution in biological solvents (Figure 3.3). The extent of this range provides the means to selectively perturb or evaluate xenon in one environment over another. Relative to gaseous xenon referenced to 0 ppm, xenon dissolved in water is typically around 192 ppm [116]. For xenon dissolved in blood, the blood plasma resonance is also around 192 ppm and xenon associating with the red blood cells is at 216 ppm [16]. Other solvents of interest include xenon dissolved in a perfluorocarbon blood substitute at 110 ppm [134] and xenon dissolved in Intralipid with a chemical shift ranging from the reported water resonance at 189 ppm to 195 ppm for 30% Intralipid [92].

3.5 Laser Polarized Xenon-129 in Biomedical Imaging and Spectroscopy

Clinical applications of xenon NMR do have precedent. Xenon has been used as a general anesthetic in the clinic since the 1950s and has been shown to be well tolerated when administered below its anaesthetic limit of 35% [71]. Thus, xenon is largely FDA approved for human studies thereby relieving one regulatory hurdle for novel *in vivo* experiments . The first MR images using hyperpolarized xenon-129 took advantage of the relative insensitivity of xenon for local field inhomogeneities in the lungs [8]. In that study, the lower gyromagnetic ratio for xenon-129 proved itself worthwhile for probing void spaces such as the excised mouse lungs in MR imaging applications. Since that time, xenon has been used to image the void space of the lungs at higher resolution in rats[37] and humans [95]. Additionally, due to the solubility of xenon in aqueous environments, valuable information about the lung endothelium and epithelium can be obtained ([111], [37]). Such information has applications to evaluating lung diseases such as emphysema [86].

Table 3.3: T_1 Relaxation of Hyperpolarized Xenon.

Solvent	**Field Strength**	**T1 Relaxation Time Constant**
Solid Xenon	0.1 T	500 hours [46]
Liquid Xenon	0.5 - 2.5 T	17.5 minutes (339 amagats, 273 K) [67]
Gaseous Xenon	5 G	33 minutes [148]
Water	7 T	45 - 60 seconds [16]
Saline		66 seconds [16]
DMSO		100s of seconds [49]
Intralipid (20%)	9.4 T	40 seconds [16]
Intralipid (30%)	2 T	25 seconds [?]
Liposomes	4.7 T	116 seconds [134]
PFOB (20%)	4.7 T	83 seconds [134]
Venous blood	4.7 T	4 seconds [7]
Arterial blood	4.7 T	13 seconds [7]
Liposomes in blood	4.7 T	47 seconds [134]
PFOB (20%) in blood	4.7 T	33 seconds [134]

In addition to assessing lung function, xenon has been used to image the brain ([127], [38]). Xenon brain imaging stems from the work of several authors to model the rate of xenon uptake into the brain as a function of time when delivered by both inhalation and intravenous injection ([102], [78], [73]). Due to its relevance in biomedical research, a full range of studies have been conducted to determine the signal lifetime which is determined by T_1 relaxation for xenon in various solvents including arterial and venous blood (Table 3.3). Due to the short T_1 relaxation time constant for xenon in venous blood, alternative delivery methods such as injection in biocompatible lipid suspensions have been considered. These studies suggest that the appropriate delivery mechanism depends strongly on experimental design.

At the cellular level, xenon was first shown to diffuse freely in and out of red blood cells in 1996 [16]. Due to the presence of paramagnetic hemoglobin within the erythrocytes, the xenon spectra contained two unique resonance frequencies in solution: one at 192 ppm attributed to xenon within the blood plasma and a peak at 216 ppm attributed to xenon in fast exchange with hemoglobin within the erythrocyte cells. The residence time for xenon in the two environments was determined by selectively exciting the plasma-associated xenon peak and monitoring the recovery of both peaks. From this information, the residence time of xenon was determined to be 20.4 ms within the red blood cells and 29.1 ms in the blood plasma.

Furthermore, in 2011, Boutin, et al. showed that for eight different cell populations (five eukaryotic, two bacteria, and one yeast) xenon NMR spectra contain two unique aqueous peaks at 277 K for cell densities above 100 million/mL [21]. In this study, the first solution peak was attributed to the standard aqueous xenon peak, while the second peak ranging from a shoulder to a well-resolved peak 7.5 ppm downfield was attributed to the aqueous intracellular space. When correcting for the internal volume of the cell population used, a peak attributed to the intracellular space was observed for populations as small as 42 million/mL. While the data was not shown, the authors claim that the two peaks were distinguishable over the full 277 - 310 K temperature range evaluated. While suggested as a method for quantification at the cellular level, the observation of two unique solution peaks has not been reproduced in our lab except for red blood cells. None-the-less, this experiment is valuable as it suggests that the exchange of xenon in and out cells originally observed with red blood cells probably occurs consistently over a wide range of cell lines.

Chapter 4

Xenon-based Molecular Sensors as Magnetic Resonance Contrast Agents

Magnetic resonance imaging (MRI) is one of the leading clinical tools for visualization of soft tissue and tumors, in addition to accessing dynamic parameters such as blood flow. In spite of the high spatial resolution achievable with conventional ^{1}H MRI, applications in molecular imaging are limited by the inability to detect small concentrations of a target molecule in comparison to positron emission tomography and simultaneous photon emission computed tomography ([141], [36]). Therefore, research efforts guiding the development of agents such as xenon-based molecular sensors that have the potential to improve the sensitivity of MRI for detection of specific molecules are very attractive.

Contrast agents for MR experiments fall into one of three categories: T_1 relaxation agents, T_2 relaxation agents, and chemical exchange saturation transfer (CEST) agents. In this chapter, each type of agent will be reviewed briefly in the context of proton-based experiments followed by a more extensive review of xenon-based molecular sensors.

4.1 Traditional Magnetic Resonance Contrast Agents

4.1.1 T_1 Relaxation Agents

T_1 relaxation contrast agents exist in two forms - those endogenous to a system and exogenous agents added to a sample prior to conducting an imaging experiment. In experiments that exploit T_1 relaxation, a pulse sequence such as a T_1-weighted gradient echo sequence or a T_1-weighted inversion recovery gradient echo sequence is used to generate positive signal intensity in regions with short T_1 time constants, or equivalently fast T_1 decay rates, since magnetization returns to thermal equilibrium more quickly in these regions. Positive contrast agents are generally preferred over negative contrast agents where decreases in signal intensity are hard to conclusively correlate with an agent over signal losses due to susceptibility mismatches or magnetic field inhomogeneities.

Endogenous T_1 contrast is generated in samples that contain more than one T_1 relaxation rate. In the brain, for example, the T_1 time constant is longer for gray matter than white matter, both of which are longer than fat [97]. Therefore, in a T_1 weighted image, fat and white matter tracks will appear brighter than the surrounding gray matter.

Exogenous T_1 contrast agents are predominantly lanthanide(III) chelates, the most prominent of which is gadolinium(III) due to its seven unpaired electrons. The electron T_1 relaxation rate of the paramagnetic metal ion (T_{1e}) contained within these contrast agents increases the relaxation rate of the endogenous ^{1}H signal as water protons transiently coordinate with a metal chelate inducing contact and pseudocontact interactions. Furthermore, T_{1e} modifies the T_1 relaxation time constant for water protons as they diffuse around the agent. T_1 relaxation is the basis for a novel class of xenon-based molecular sensors currently in development and will therefore be discussed in more detail in Chapter 5.

T_1 relaxation in the presence of exogenous agents with MRI depends on the inherent relaxivity of the agent(r_1) and the total concentration of the agent ([CA]) as

$$\begin{aligned} \frac{1}{T_{1,obs}} &= \frac{1}{T_{1,d}} + \frac{1}{T_{1,p}} \\ &= \frac{1}{T_{1,d}} + r_1[CA] \end{aligned} \tag{4.1}$$

where $T_{1,obs}$ is the observed T_1, $T_{1,d}$ is the naturally occurring diamagnetic contribution to relaxation, and $T_{1,p}$ is the additional paramagnetic component. Typically, relaxivity is reported in units of (mM s)$^{-1}$ and consequently the concentration of agent used is given in mM. As seen in Equation 4.1, the total $T_{1,obs}$ relaxation rate varies linearly with the concentration of the agent accumulated in the region of interest.

The threshold for detecting the presence of exogenous T_1 agents with MRI depends strongly on the relaxivity of the agent, where higher values of r_1 require smaller concentrations of the agent to result in a detectable change in T_1. Clinical gadolinium contrast agents typically have a relaxivity of 3-5 (mM s)$^{-1}$ [84]. Consequently, $\sim$mM concentrations of the agents are required to generate distinguishable contrast. One way to improve the relaxivity of T_1 agents is to change the chelating ligand such that the number of coordinated water molecules is increased. While it is theoretically possible to generate relaxivities that are 60 times higher when coordinating three water molecules at a time versus one water molecule, care must be taken to avoid destabilizing the chelate as free gadolinium is quite toxic (LD_{50} = 0.2 mg/kg in mice) [143]. Additional parameters that can be modified to improve the relaxivity of these agents are increasing the exchange rate of the coordinated water molecules, increasing the rotational correlation time of the agent by tethering it to a bulky protein, and loading the agents onto molecular scaffolds ([143], [84]). Such improvements push the threshold for detecting the presence of the agents into the μM regime for *in vitro* experiments [150].

4.1.2 T_2 Relaxation Agents

While T_1 contrast agents generate positive MR image contrast, detection of low concentrations of these agents is limited by the ability of water molecules to interact with the paramagnetic metals [9]. Superparamagnetic nanoparticles, on the other hand, most often decrease the local transverse ^{1}H signal through both T_2 and T_2^* relaxation and are therefore used as negative contrast agents. These particles typically contain either an iron oxide monocrystalline (monocrystalline iron oxide nanoparticle, MION) or polycrystalline (superparamagnetic iron oxide nanoparticle, SPIO) core ranging from 5 - 30 nm in diameter that is subsequently coated with a polymer such as dextran for solubility and biocompatibility [9]. Traditionally, T_2 contrast agents are detected with a CPMG pulse sequence in low-field magnetic relaxometry experiments [35] or with a T_2^*-weighted gradient echo pulse sequence for imaging applications.

T_2 relaxation in the presence of SPIOs is primarily due to the saturation magnetization (M_s) of the nanoparticle, volume fraction of particles in solution (V), inter-echo spacing (τ_{CP}), and the total size of the particle. For strongly magnetized spheres, T_2 relaxation is given by [25]

$$T_2 = \frac{1000\,(1 + (4/9)^2(\tau_D/\tau_{CP})^2\alpha^5)}{(4/9)V\tau_D(\Delta\omega)^2} \tag{4.2}$$

where T_2 is in ms, $\tau_D = r^2/D$ is the time for water to diffuse around a particle of radius r, D is the self-diffusion coefficient of water, $\Delta\omega$ is the Larmor frequency shift at the surface of the particle that depends linearly on M_s, and

$$\alpha = \left[\frac{\Delta\omega\tau_{CP}}{a + b\Delta\omega\tau_{CP}V}\right]^{1/3} \tag{4.3}$$

where a and b were experimentally determined to be 1.34 and 0.99 respectively.

SPIOs are currently being used to build commercially viable low-field assays based on T_2 relaxation switches at T2 Biosystems in Lexington, MA. In these experiments, SPIOs can be conjugated with antibodies that recognize small multivalent molecules [35]. When both the SPIOs and small molecules are in solution, the particles will form larger clusters resulting in a change in T_2. Depending on the properties of the nanoparticle being used, the T_2 contrast can either be positive or negative.

In addition to T_2 effects, the superparamagnetic core of an SPIO generates significant local magnetic field inhomogeneities. These inhomogeneities lead to decreases in T_2^* [84]

$$\frac{1}{T_2^*} = \frac{1}{T_2} + \gamma\Delta B_0 \tag{4.4}$$

where γ is the gyromagnetic ratio of the detected nucleus and ΔB_0 is the induced change in the local magnetic field. Practically, T_2^* is often determined as a function of particle concentration

$$\frac{1}{T_2^*} = r_2[\text{SPIO}] + \text{constant} \tag{4.5}$$

where r_2 is the relaxivity of the agent in $(\text{mM s})^{-1}$, [SPIO] is the concentration of the agent in mM, and the constant is empirically determined. The large decrease in T_2^* generated by SPIOs is often exploited in high-field applications and is detected using a T_2^*-weighted pulse sequence.

The relaxivities of T_2 agents are much larger than T_1 agents and usually range from 100 - 200 $(\text{mM s})^{-1}$ [84] and micelles containing clusters of SPIOs have been detected in picomolar concentrations *in vitro* [72]. Typically, clinical T_2 agents generate negative contrast on an MR image. As described in the previous section, this signal depletion can be hard to distinguish from other sources of signal depletion in the sample. Positive contrast can be generated by selectively exciting spins off-resonance from the primary water resonance [34] or by utilizing pulse sequences that only refocus the dipole field produced by a SPIO [85], but these techniques typically have a lower sensitivity than T_2^*-weighted pulse sequences [84].

4.1.3 Chemical Exchange Saturation Transfer Agents

Chemical exchange saturation transfer (CEST, [138]) is a method of generating MR contrast based on the exchange of nuclei between two unique chemical environments. Unlike the more general magnetization transfer scheme that includes both chemical exchange and additional dipolar effects [42], contrast in a CEST experiment is generated solely by chemical exchange of a spin active nucleus between the two sites. The CEST effect is nicely reviewed by Zhou and van Zijl [151] and Hancu, et al. [56], and is the basis for many of the xenon experiments presented in this thesis.

In a CEST experiment, the resonance frequency of an exchangeable species (A) is saturated with a RF pulse (ω_1) for some amount of time after which the bulk water resonance (B) is detected. In order for this effect to be observable, exchange between the two sites should be slow on the NMR timescale. This condition is met when the lifetime of a proton in species A (τ_A) and separation of the resonance frequencies ($\Delta\omega = \omega_A - \omega_B$) meet the criteria

$$\tau_A \Delta\omega > 1. \tag{4.6}$$

As the signal from species A is depleted by the saturation pulse, its exchange back into the bulk pool B results in a net decrease in signal intensity in pool B. This signal depletion can be predicted by solving the McConnell-Bloch equations ([87], [151])

$$\begin{aligned}
\frac{dM_{xA}}{dt} &= -\Delta\omega_A M_{yA} - R_{2A} M_{xA} - k_{AB} M_{xA} + k_{BA} M_{xB} && (4.7)\\
\frac{dM_{xB}}{dt} &= -\Delta\omega_B M_{yB} - R_{2B} M_{xB} + k_{AB} M_{xA} - k_{BA} M_{xB} && (4.8)\\
\frac{dM_{yA}}{dt} &= \Delta\omega_A M_{xA} + \omega_1 M_{zA} - R_{2A} M_{yA} - k_{AB} M_{yA} + k_{BA} M_{yB} && (4.9)\\
\frac{dM_{yB}}{dt} &= \Delta\omega_B M_{xB} + \omega_1 M_{zB} - R_{2B} M_{yB} + k_{AB} M_{yA} - k_{BA} M_{yB} && (4.10)\\
\frac{dM_{zA}}{dt} &= -\omega_1 M_{yA} - R_{1A}\left(M_{zA} - M_{0A}\right) - k_{AB} M_{zA} + k_{BA} M_{zB} && (4.11)\\
\frac{dM_{zB}}{dt} &= -\omega_1 M_{yB} - R_{1B}\left(M_{zB} - M_{0B}\right) + k_{AB} M_{zA} - k_{BA} M_{zB} && (4.12)
\end{aligned}$$

where $M_{x,y,z}$ are the x, y, and z components of the magnetization following a pulse tipping the initial magnetization, M_0, out of the z-axis, $R_{1,2} = 1/T_{1,2}$, $\omega_1 = \gamma B_1$ is the saturation pulse in Hz applied along the x-axis in the rotating frame, k_{AB} is the rate of exchange from pool A into pool B, k_{BA} is the rate of exchange from pool B into pool A, and $\Delta\omega = \omega - \omega_{A,B}$ is the offset from the applied saturation frequency (ω). Typically, the resonance frequency of the saturation pulse is swept over a broad range containing both pools of interest. When the signal from pool B is integrated and plotted as a function of the saturation frequency, the plot is dubbed a ‘z-spectrum’. When species A is detectable, two regions of signal depletion are expected in the z-spectrum - a large depletion at the resonance frequency of the bulk pool B and a smaller dip around the resonance frequency of species A.

CEST agents can either be diamagnetic or paramagnetic in nature. Diamagnetic CEST (DIACEST) agents are typically small molecules with exchangeable -NH or -OH groups [138]. Of note, sensors can be designed to monitor the pH of a solution ([89], [137]) with applications targeting tumor imaging. While generally useful, the exchangeable sites are usually within 5 ppm of the bulk water signal in DIACEST experiments. Designing DIACEST agents where the exchange of protons is slow on the NMR timescale and pulse sequences to specifically saturate the resonance frequency of interest without indirectly influencing the water resonance can be challenging.

Paramagnetic CEST (PARACEST) agents are typically chelated lanthanide (III) metals with a large chemical shift anisotropy such as europium, terbium, and dysprosium ([17], [56]). These chelates can result in unique proton resonance frequencies out to 800 ppm [150]. The basis for the PARACEST is the same as for DIACEST with a much larger chemical shift range and agents have been developed for targeted molecular imaging applications [5].

4.2 Cryptophanes for Xenon Host-Guest Interactions

In addition to its direct biomedical uses reviewed in Chapter 3, hyperpolarized xenon-129 has a long history of use in biophysical experiments. Due to its lipophilic nature, xenon can be used to investigate hydrophobic cavities on proteins such as myoglobin and hemoglobin [132], lipoxygenase [23], and maltose binding protein [110]. Furthermore, due to its exquisite sensitivity to its local environment, NMR studies using xenon-129 can detect conformational changes in maltose binding protein [110] and chemotaxis Y protein [82] even though specific interactions have a relatively low binding affinity ($\mathrm{K} \leq 200\ \mathrm{M}^{-1}$ [81]).

In part due to this low affinity for natural targets such as hydrophobic pockets on proteins, researchers sought to develop specific hosts for xenon. Among the first organic host molecules evaluated were self-assembling dimers [24] and α-cyclodextrin ([12], [123]). In each of these cases, xenon was in slow exchange with the host molecule yielding a unique chemical shift, but association was still relatively weak ($\mathrm{K} < 20\ \mathrm{M}^{-1}$) at room temperature.

A study by Mecozzi and Rebek concluded that the optimal ratio for host-guest association is for the guest to occupy 55% of the internal volume of the host [90]. For xenon, with a van der Waals volume of 43 $\mathring{A}^3$, the optimal volume of the host molecule should be close to 76 $\mathring{A}^3$. Hemicarcerands such as fullerenes [128] and zeolites [68] were evaluated as hosts due to the size of their internal cavities. These molecules showed strong affinities for xenon, but exchange of xenon with the molecules is very slow thereby limiting their applicability using hyperpolarized xenon as a MR contrast agent.

Cryptophanes are a class of cage-like molecules consisting of two cyclotriveratrylene caps connected by three alkoxy linkers of varying length (Figure 4.1) that were first synthesized by Gabard and Collet in 1981 [44]. These molecules are classified by the number of methyl groups in the bridging linkers and whether they adopt an *anti* or *syn* conformation ([33], [65]). Cryptophane-A, or cryptophane-222 in the *anti* conformation, is most commonly used in the Wemmer and Pines labs at UC Berkeley and will be referred to as cryA for the remainder of this thesis. This molecule has several nice properties: its internal volume at 95 $\mathring{A}^3$ is large enough to host one and only one xenon atom at a time [33], it has relatively fast exchange kinetics for xenon in and out of the cage [30], a high binding affinity for xenon in both tetrachloroethane and water when made soluble ([11], [65],[60]), and its synthesis has been worked out by multiple groups thereby reducing cost and the synthetic lag time.

4.2.1 Thermodynamic Properties

The holy-grail for a xenon-based molecular sensor is for it to have the highest binding affinity possible, thereby creating a strong NMR signal for the sensor-associated signal, while maintaining exchange of xenon in and out of the sensor that is fast enough to replenish the hyperpolarized sensor-associated xenon signal, yet slow on the NMR timescale to maintain a unique resonance frequency. Binding affinities for xenon-based molecular sensors are compared described by their equilibrium constant

$$K = \frac{[\mathrm{Xe@cryA}]}{[\mathrm{Xe}]_w[\mathrm{cryA}]} \tag{4.13}$$

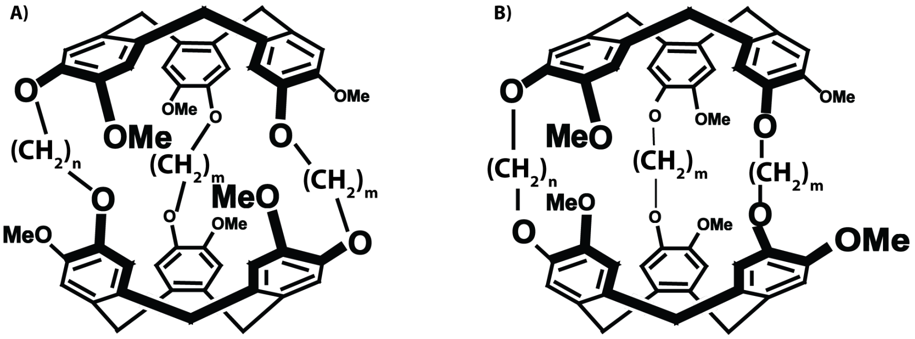

Figure 4.1: Cryptophanes. Cryptophane-nmm cage molecules can be synthesized in either the *anti* or *syn* conformation. A) *Anti* isomers have D3 symmetry and are named according to the number of methyl spacers are present. Cryptophanes -111, -222 (A), -223, -233, -333 (E) have all been synthesized and are presented in more detail in this thesis. B) *Syn* isomers have C3 symmetry and are likewise named according to their bridge structures (-222 (B) and -333 (F)). The *Syn* isomers are presented here for completeness, but will not be discussed further.

where [Xe@cryA] is the concentration of xenon complexed with the cryptophane cage construct, $[\mathrm{Xe}]_w$ is the concentration of xenon in solution, and [cryA] + [Xe@cryA] is the total concentration of cage in solution.

The binding affinity for xenon with a cryptophane cage depends strongly on the solvent used in the study, the number of solubilizing groups substituted for methoxys for studies conducted in water, and temperature. In 1998, Bartik, et al. measured an equilibrium constant $K = 3900\ M^{-1}$ for the xenon-cryA complex in tetrachloroethane at 278 K by integrating the area of the sensor-associated resonance relative to the area for the bulk xenon resonance. This association is 10 - 100 times stronger than dichloromethane, dibromomethane, and chloroform with cryptophane-A at the same temperature [33]. Changing the physical size of the cage by modifying the length of the bridging linker has a linear effect on the binding affinity [26] (Table 4.1). Cryptophane-111, the smallest possible cryptophane at 81 cubic angstroms, has the highest equilibrium constant in tetrachloroethane with $K = 10{,}000\ M^{-1}$ [41], but the slow exchange of xenon with this molecule ultimately make it less appealing for targeted molecular imaging with hyperpolarized xenon-129.

In addition to changing the physical size of the cryptophane cage, the surface chemistry of cryA can be modified to increase the binding affinity of xenon with the host molecule. Huber, et al. modified cryptophane-A such that one methoxy group on each of the six benzene rings was substituted with OCH_2COOH [66]. Their group calculated $K = 6800\ M^{-1}$ at 293 K for xenon associating with the hexaacid cryA in water by integrating the signal intensities for the aqueous and caged xenon peaks. The highest binding affinity reported for a xenon-cryptophane complex is for cryA modified such that the methoxy on each of the three benzene groups on one of the two cyclotryveratrylene caps was substituted with an acid group [61]. This molecule is both soluble in water and also contains a net dipole moment. In that study, the authors used isothermal calorimetry (ITC) to determine $K = 17{,}400\ M^{-1}$ at 293 K and $K = 30{,}000\ M^{-1}$ at 310 K for xenon with this triacid complex in

Table 4.1: Properties of Cryptophane Molecules

Cryptophane	Solvent	Size ($\mathring{A}^3$)	Temperature (K)	K (M^{-1})
111	Tetrachloroethane-d_2	81 [41]	278	10000 [41]
222	Tetrachloroethane-d_2	95 [26]	278	3900 [11]
223	Tetrachloroethane-d_2	102 [26]	278	2800 [26]
233	Tetrachloroethane-d_2	117 [26]	278	800 [26]
224	Tetrachloroethane-d_2	110 [26]	278	9.5 [26]
333	Tetrachloroethane-d_2	121 [26]	278	5-10 [65]
Hexaacid 222	Water	95 [26]	293	6800 [66]
Triacid 222	Water	95 [26]	293	17400 [61]
Triacid 222	Water	95 [26]	310	30000 [61]

water. Furthermore, the ITC results suggest that entropic rather than enthalpic effects drive complexation of xenon with this version of a cryptophane cage. For a list of cryptophane constructs and their relevant properties, see Table 4.1.

Chemical exchange of xenon with a cryptophane cage can either be measured directly with an inversion recovery pulse sequence that selectively monitors the cage-associated xenon peak or it can be indirectly inferred from the linewidth ($\Delta\nu$) of the cage-associated resonance frequency since

$$k_{ex} = \pi\Delta\nu \tag{4.14}$$

in the limit where chemical exchange dominates the observed linewidth. The exchange rate, k_{ex}, for xenon with a soluble cryA in water very similar to the construct used in Chapter 5 was empirically determined to be[30]

$$k_{ex} = 0.738e^{0.147T} \tag{4.15}$$

where T is the system temperature in degrees Celsius. Therefore, exchange times ($1/k_{ex}$) for the systems studied in this thesis are expected to be around 72 ms at 20°C, 34 ms at 25°C, and 6 ms at 37°C.

4.2.2 Chemical Shift for Xenon-Cryptophane Complexes

In addition to providing a broad range of chemical shifts in biological solvents (Chapter 3), the highly polarizable electron cloud of xenon is sensitive to the composition of the cryptophane construct in solution (Figure 3.3, Table 4.2). Relative to gaseous xenon referenced to 0 ppm, the hexaacid cryA described above has a resonance frequency at 64 ppm in water [66]. The resonance frequency of the hexaacid cage shifts upfield to 52 ppm for cryptophane-223, 42 ppm for cryptophane-233, and 35 ppm for cryptophane-E. The upfield shift with increasing internal volume for water soluble cryptophanes matches the shift in resonance frequency for the unmodified cage in tetrachlorethane [66] and is attributed to a relative shielding of xenon's electronic cloud as the cages become increasingly larger in

Table 4.2: Xenon-Cryptophane Chemical Shifts

Cryptophane	Solvent	Temperature (K)	Xenon Chemical Shift (ppm)
	Xenon Gas	na	0
111	Tetrachloroethane-d_2	293	31 [41]
222	Tetrachloroethane-d_2	293	68 [26]
223	Tetrachloroethane-d_2	293	60 [26]
233	Tetrachloroethane-d_2	293	47 [26]
333	Tetrachloroethane-d_2	293	30 [65]
Hexaacid 222	D_2O	293	64 [66]
Hexaacid 223	D_2O	293	52 [66]
Hexaacid 233	D_2O	293	42 [66]
Hexaacid 333	D_2O	293	35 [66]
Monoacid 222	D_2O	298	70 [125]
Monoacid 222	2% Intralipid	293	71 [92]
6Ru+ 111	D_2O	293	308 [40]

internal volume.

The sensitivity of xenon for its local environment is high enough to detect changes in the chemical environment of the cryA solely due to the substitution of deuterium atoms on the ethylene bridges or methoxy groups [27]. In that study, a linear upfield chemical shift ($\Delta\delta$) of

$$\Delta\delta(Xe@cryA - Xe@cryA_{subs}) = 0.048N_b + 0.034N_m \tag{4.16}$$

was empirically determined for cryA substituted with $N_b = [8, 12]$ deuterium atoms on the ethylene bridges and $N_m = [3, 6, 9, 12, 15, 18]$ deuterium atoms on the methoxy groups. The largest chemical shift for a xenon-based molecular sensor is for cryptophane-111 complexed with six ruthenium(II) chelates [40]. The presence of the diamagnetic metal close to the cage induces a chemical shift of 308 ppm relative to xenon gas.

Interestingly, the electron cloud of xenon is sensitive enough to detect chiral splittings within a construct multiple bonds away. The original functionalized xenon biosensor consisted of a racemic mixture of cryA conjugated to a solubilizing peptide (Cys-Arg-Lys-Arg) with a maleimide linking the soluble cage to enantiomerically pure biotin [124]. This construct has two chiral centers which resulted in four unique resonances in a xenon spectrum due to the four diastereomers in solution: RLL, RLR, LLL, and LLR. A splitting of 0.15 ppm was observed for the addition of the solubilizing peptide chain with a ∼1 ppm splitting due to the addition of the maleimide.

4.3 Indirect Detection of Xenon-based Molecular Sensors

Xenon-based molecular sensors with cryptophane cages as the host have great potential as MR contrast agents. While direct detection of the cage-associated resonance frequency serves as a mechanism for generating positive contrast, it requires μM - mM concentrations of the cage depending on the composition and polarization of the xenon gas mixture used in the experiment. High concentrations are required due to the relatively small population of polarized xenon occupying a cage at any given time. Occupancy of the cage can be determined by the equilibrium condition described in Equation 4.13. Assuming an equilibrium constant K = 10,000 M^{-1}, the xenon occupancy of the cage

$$\begin{aligned} \text{occupancy} &= \frac{[\text{Xe@cage}]}{[\text{cage}] + [\text{Xe@cage}]} \qquad (4.17) \\ &= \frac{K[\text{Xe}]_w}{1 + K[\text{Xe}]_w} \qquad (4.18) \end{aligned}$$

is approximately 80% for a 2% xenon gas mixture dissolved into water at 25°C. The solubility of a 2% xenon gas mixture in water at 25°C, 65 psi is approximately 390 μM. With a realistic single-shot SNR of 50 for xenon dissolved in water, direct detection of the cage at 80% occupancy with an SNR of 5 is >30 μM as this value does not correct for the increased linewidth expected for xenon in the caged environment. In order to detect submicromolar concentrations of the cage, the initial polarization of xenon can be enhanced, a cage construct with a higher equilibrium constant can be used, or an indirect method of detection can be employed.

4.3.1 Hyper-CEST

In 2006, an indirect detection scheme based on traditional proton-based CEST - chemical exchange saturation transfer of hyperpolarized nuclei (Hyper-CEST) was developed in the Pines and Wemmer labs at UC Berkeley[116]. Hyper-CEST takes advantage of the chemical exchange of xenon in and out of the caged environment. As described above, due to the extensive chemical shift range of xenon, this exchange of xenon with cryA, typically on the order of 10 milliseconds, is slow enough on the NMR timescale to have a unique resonance frequency relative to the aqueous xenon peak. In a Hyper-CEST experiment, a RF pulse is applied at the resonance frequency of the caged xenon for 1 - 20 seconds. The population of hyperpolarized xenon within the cage environment at any time during the pulse will be depolarized by this pulse, with 100 - 2000 atoms potentially experiencing the saturation pulse. After application of the pulse, detection of the aqueous xenon peak results in a lower signal intensity when compared to the signal acquired without a pulse at the caged xenon resonance.

Instead of comparing the signal depletion observed following a saturation pulse to the case where a pulse is not applied, signal depletion due to the presence of the cryptophane cage construct is typically compared to an experiment where a saturation pulse is applied equidistant, but on the opposite side of the aqueous xenon signal. While not expected to contribute to the depolarization of the aqueous xenon signal, application of this off-resonance pulse corrects for indirect effects of applying a pulse at the cage-associated xenon resonance frequency. Using the Hyper-CEST technique, detection of 10 nM of a soluble cryptophane construct is possible [118]. This will be discussed in full detail in Chapter 5.

4.4 Functionalized Xenon-based Molecular Sensors

A group of students in the Pines and Wemmer labs, in collaboration with Peter Schultz at the Scripps Research Institute, developed the first functionalized, water soluble version of cryptophane-A in 2001 [124]. Since this time, a few research labs, namely the Pines and Wemmer labs at UC Berkeley, Ivan Dmochowski's group at the University of Pennsylvania, and Patrick Berthault and colleagues in France have taken this first construct and developed a novel class of MR sensors for targeted molecular imaging.

4.4.1 Optimization of Functionalized Xenon-based Molecular Sensors

The advent of water soluble cryptophane cages in 2001 [124] brought with it the possibility for using xenon-based molecular sensors as targeted MR contrast agents. In that initial targeted study, cryA was modified such that one of the methoxy groups was substituted with acetic acid (monoacid cage). Through standard solid-phase peptide synthesis, a solubilizing peptide sequence (Cys-Arg-Lys-Arg) was coupled through the acetic acid group. Following cleavage of the soluble construct, TMPEO-Maleimide activated biotin was added in solution. Not only did that construct have four unique resonance frequencies arising from its chiral centers were clearly distinguishable in water, but it was possible to detect binding of the biotinylated construct to avidin via a downfield change of ∼4 ppm in the xenon chemical shift (Figure 4.2, [125]).

While surprisingly useful for assessing the chiral nature of the sensor, the spectral splittings result in a decreased SNR for the sensor in solution. Based on this observation, an array of sensors was screened for optimization of the sensor given experimental parameters [83]. In that optimization study, the original maleimide was replaced with a lysine such that the biosensor construct had only two diastereomers when linked to biotin (RL and LL). The linker was made in different lengths such that the spectral properties could be assessed upon binding to the avidin target. Both chemical shift and the linewidth of the cage-associated xenon resonances were found to relate inversely with linker length upon binding to avidin. Hence, short linkers resulted in broad resonances that shift farther downfield upon binding. For long linkers no shift was observed upon target binding, but the diastereomers have a narrow linewidth.

In addition to linker length, the rigidity of the linker was evaluated in that study [83]. When a poly-glycine chain was used instead of a flexible polyethylene glycol linker, the correlation time for the biosensor construct approached that of the much larger avidin protein.

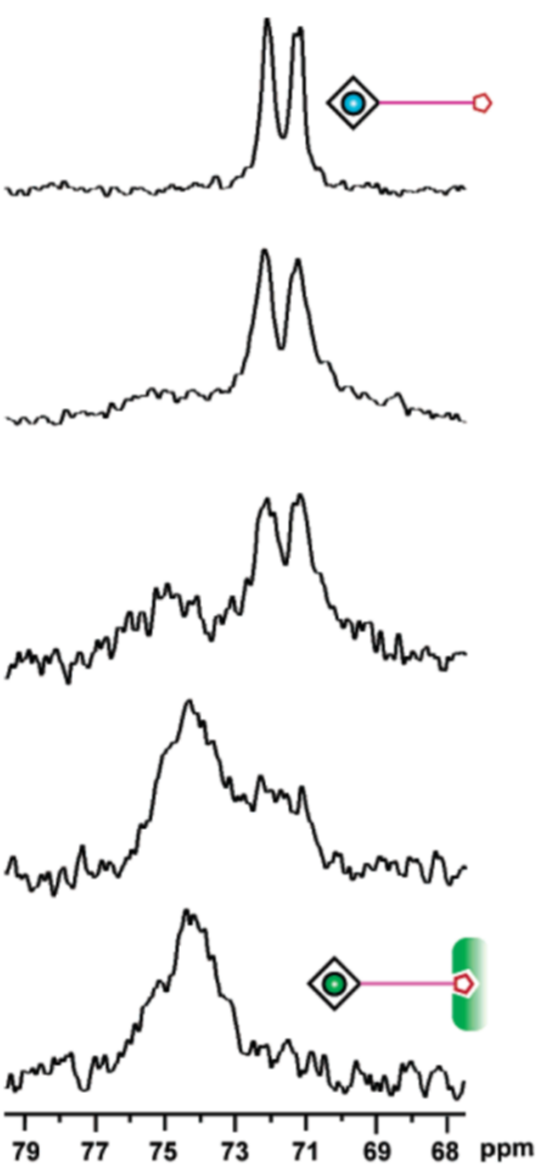

Figure 4.2: Functionalized Xenon-based Molecular Sensor. This figure is taken from a paper that expands on the work utilizing the first xenon-based molecular sensor [125]. In this study, the biosensor [cryA-(Cys-Arg-Lys-Arg)-maleimide-linker-biotin] was titrated from the top picture with 0%, 10%, 20%, 60%, and 120% avidin relative to the concentration of cage in solution. As the concentration of avidin increases, the sensor-associated resonance frequencies shift downfield and broaden.

Table 4.3: List of Xenon Biosensors Developed for Targeted Applications

Reference	**Sensor**	**Target**	**Change in Chemical Shift (ppm)**
Spence, et al. 2001	Biotin	Avidin	4
Roy, et al. 2007	ssDNA (20-mer)	ssDNA (20-mer)	1.5
Wei, et al. 2006	MMP-7 Substrate	Matrix Metalloproteinase	0.5
Schlundt, et al. 2009	13aa sequence	Major Histocompatibility Complex II	1.0
Chambers, et al. 2009		Carbonic Anhydrase (I/II)	3-7.5
Garimella, et al. In Process	Peptide	Rhodamine G6	2
Seward, et al. 2008	Tetra(RGD)	Integrin	NA
Boutin, et al. 2001	Transferrin	Transferrin Receptor	NA

The increased rigidity led to an enhanced broadening of the cage-associated resonance upon binding to avidin. Furthermore, additional cage-associated resonances were observed that were attributed to interaction of neighboring constructs with each other. The authors implied that a flexible linker is preferred over a rigid linker for a more homogeneous sampling of the sensor's environment.

4.4.2 Targeted Sensors

Since the successful development of a targeted xenon biosensor, a number of research groups have begun to develop targeted sensors (See Table 4.3). Roy, et al. conjugated monoacid cryA with a 20-mer of single-stranded DNA and was able to distinguish between the sensor and its hybridized complex [109]. A xenon-based molecular sensor based on the enzymatic cleavage of a known matrix metalloproteinase (MMP) peptide substrate generated a detectable 0.5 ppm shift upon addition of MMP for one of its diastereomers and a 0.3 ppm shift for the second [140]. In 2009, cryA was conjugated to a hemagglutinin peptide that produced a 1 ppm chemical shift upon binding to its target, the major histocompatibility complex class II protein [115]. Around this same time, carbonic anhydrase II, a marker for polycystic kidney disease, was detected through a 7.5 ppm shift in the xenon resonance frequency using a xenon-based molecular sensor [29].

Most recently, label-free detection of an optical dye was detected by a 2 ppm chemical shift of cryA conjugated to a peptide selected to specifically bind to the optical target [45]. This dye-binding cryptophane biosensor is especially promising, as the combinatorially generated peptides comprised a library of sensors that were originally screened for their optical binding capabilities rather than for xenon chemical shift. If the peptides in that library could be assessed for their signature in a xenon-based NMR experiment, they could have great potential for combinatorial screening on a microfluidic chip.

4.4.3 Cell Targeting

Of important note are the cell targeted studies that have been published thus far. In a study by Seward, et al., cryA was separately conjugated with poly-arginine, residues 48-60 of the HIV-1 TAT protein, and the $\alpha_v\beta_3$ receptor targeting sequence $(RGD)_4$ [120]. While xenon-129 NMR spectra were not acquired, the cellular uptake and toxicity of these three constructs on HFL-1 human diploid lung fibroblasts, AsPC-1 and CAPAN-2 human pancreatic carcinoma cell lines, and human red blood cells were assessed. The constructs were taken up in all of the cell lines except for the red blood cells as monitored by cage-fluorescent versions of the constructs. Furthermore, low cytotoxicity was observed even the cells were subjected to a 100 μM concentration of the construct.

In a study conducted by Boutin, et al., five cryA molecules were attached to holo-transferrin due to its biocompatibility, surface targeting receptor, and high receptor density ($1.6*10^5$ external, $8*10^5$ total) on the surface of the cell line chosen [22]. For this study, a second sensor was developed that had two cryptophane-A molecules and two fluorescent Rhodamine green molecules bound to transferrin. One-dimensional xenon-129 spectra of the non-fluorescent probe revealed two cage-associated peaks: one at 68-69 ppm for the aqueous cage-associated xenon peak and another at 79 ppm attributed to the cage in a lipid environment based on the results of Meldrum, et al. [92]. The xenon experiments were correlated with fluorescence microscopy for cells that were prepared by the same protocol. The fluorescence experiment revealed that the xenon biosensor was located within the intracellular space as well as on the surface of the cell.

At the time this thesis was written, the above mentioned experiments were the only targeted cell-based studies utilizing a xenon biosensor published in the literature. Personal communication with colleagues at Berkeley, competitors at UPenn, and conference proceedings suggest that this field is about to explode. Clinical applications such as cancer cell targeting are near publication and extensions into animal models are being planned. I personally cannot wait to see the results of all of these challenging experiments.

4.4.4 Multiplexing and Multivalent Sensors

The development of different cryptophane cages with an array of targeting groups offers the potential for multiplexing, or targeting different chemical environments through the unique chemical shift of xenon for these cages, within a solution. While originally proposed in the first paper by Spence, et al. 2001, multiplexing was first realized by Berthault and colleagues [14]. In their study, 300 μM cryptophane-111 in deuterated tetrachloroethane was added to the bottom of the NMR tube and 300 μM of hexaacid cryptophane-222 dissolved in water was added on top. As these solvents are immiscible, they are capable of separating the different cages to unique positions in space. A fast gradient echo image with a frequency selective pulse was used to distinguish the constructs separated in space.

Multivalency of the cage was first achieved through acid-base and hydrophobic interactions of cryptophane-A with two types of water soluble dendrimers, polypropylene imine

(PPI) and polyamidoamine (PAMAM) [96]. The cage was purposefully complexed rather than bound to the dendrimers in order to average the diastereomeric splittings in the xenon NMR spectra. In this study the cage to dendrimer ratio was titrated such that a linearly increasing number of cages could be associated with the complexes. The PAMAM complexes were found to more adequately solubilize the cage with 4-5 PAMAM molecules complexing 7-11 cage molecules. Direct detection of an avidin bound dendrimer complex with two cages associated resulted in eight times the SNR for the cage-associated xenon resonance relative to the same concentration of biosensor in solution. This signal enhancement was attributed to the contribution of two cages per dendrimer, the absence of diastereomer peaks, and a reduced linewidth (1/2) for the dendrimer associated peaks.

In addition to direct amplification of the cage resonance, multivalent sensors can significantly decrease the threshold for indirectly detecting xenon-based molecular sensors. In collaboration with the Matt Francis lab at UC Berkeley, approximately 125 cryptophane cages were attached to the interior of a MS2 viral capsid [93]. Using this loaded construct, the threshold for detecting a xenon-based molecular sensor was reduced from 10 nM (the details for which will be described in Chapter 5) to 0.7 pM of the MS2 viral capsid. Additional amplification of the contrast achieved through indirect detection of the xenon biosensors with the Hyper-CEST can be achieved by grafting the cage onto the surface of an M13 bacteriophage [126]. In a study using M13, approximately 1000 cages were bound to the exterior of the bacteriophage, pushing the threshold for detection to 230 fM *in vitro*. When functionalized with antibodies for cancer cell lines, these types of multivalent constructs have huge potential for pre-clinical development of xenon-based molecular sensors for potential clinical applications.

Chapter 5

The Effect of Temperature on Detecting Xenon-based Molecular Sensors

Indirect detection of xenon-based molecular sensors with the Hyper-CEST technique opened the door to the possibility of detecting concentrations of sensors in the range of biologically relevant targets. With Hyper-CEST, magnetization from encapsulated xenon can be labeled by a selective RF pulse that induces depolarization of the net nuclear magnetization. Depending on the exchange rate, hundreds to thousands of nuclei per second per cage experience this pulse resulting in a depletion of the magnetization of free, dissolved xenon in the vicinity of the cage. This ensemble of uncaged xenon serves as a reservoir to detect the flow of saturated spins from the functionalized cage where the magnetization change is encoded.

At the time this research was conducted, a kinetic model had been developed to describe the effect of the interaction of xenon with the sensors. In this model, hyperpolarized xenon could exchange in and out of the cage freely and the hyperpolarized xenon could relax to thermal equilibrium by T_1 relaxation in the bulk solution, T_1 relaxation in the presence of the cage, and due to a saturation pulse applied at the resonance of the xenon and cage signal. While the depletion of magnetization was later shown to be fully modeled through the use of the McConnell-Bloch equations with a term correcting for inhomogeneous linebroadening [107], this simple four-state model can be used as a conceptual tool for developing ways to manipulate system parameters to indirectly detected of lower concentrations of cages (Figure 5.1).

The parameters that affect the response to the Hyper-CEST technique are the binding affinity of the xenon-cage complex, exchange rates of xenon in and out of the cage, strength of the saturation pulse, and length that the saturation pulse is applied. Increasing the saturation power and time have a positive effect on generating contrast [30], but the use of these options should be minimized to avoid future SAR issues if the sensors are to be used *in vivo*. As described in Chapter 4, researchers have synthesized cages with a variety of binding affinities where the highest affinity is found for cryptophane-111 due to the tightness of the

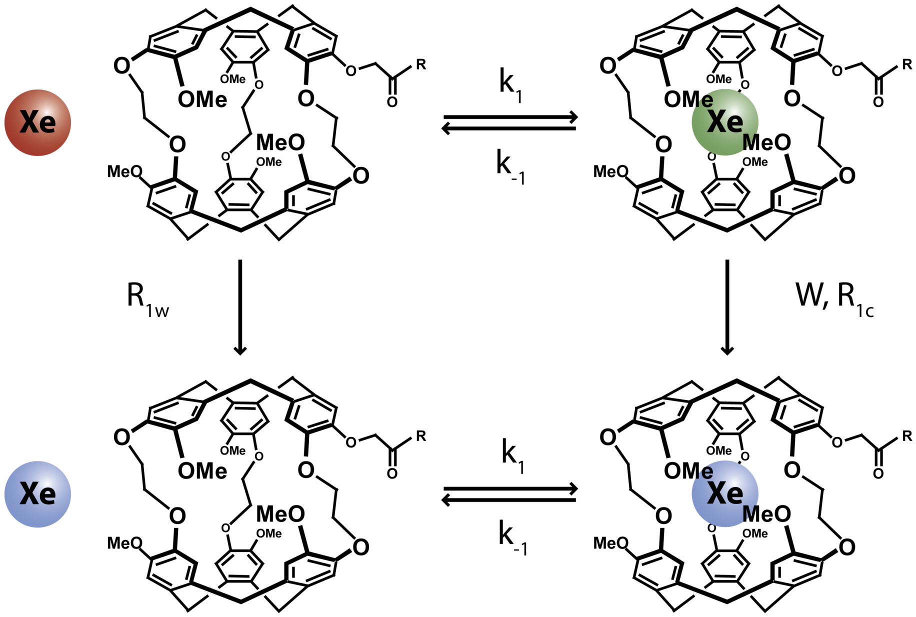

Figure 5.1: Four-state Model for Chemical Exchange of the Xenon-Cage System. Hyperpolarized xenon (red) can freely exchange in and out of the cryptophane cage. When a hyperpolarized xenon atom is contained within the cage (green), it can lose its polarization (blue) due to the application of a saturation pulse (W) or T_1 effects while within the cage ($R_{1,c}$). Furthermore, free hyperpolarized xenon can relax to thermal equilibrium due the bulk T_1 relaxation effects ($R_{1,w}$).

cage environment [41]. Other methods used to vary the affinity for xenon with the cage are additional adjustments to the linker length [65], varying the hydrophobicity of the cage itself ([66], [60]), and using a non-cryptophane host ([24] , [12], [123], [128], Naoko Kotera (unpublished data)).

In reality, a trade-off must be made between binding affinity and chemical exchange in order to detect small concentrations of the sensor. Since the exchange rates are very sensitive to temperature, varying this parameter provides an opportunity to interrogate its effect on the system. Using temperature to control depolarization transfer has three advantages: increasing temperature increases the exchange rate of xenon with the cage molecules ([11], [83], [66]), the binding constant of the xenon-cage complex tends to increase as temperature increases [60] making more xenon susceptible to selective saturation, and the solubility of xenon in water decreases with increasing temperature [47] resulting in a smaller reservoir pool that is easier to saturate. In the following sections, three methods for monitoring the effect of temperature on the contrast generated with the Hyper-CEST technique will be presented: bulk xenon magnetization as a function of the length of the applied saturation pulse, saturation as a ramped function of temperature [118], and depolarization due to the presence of a sensor in an imaging experiment [117].

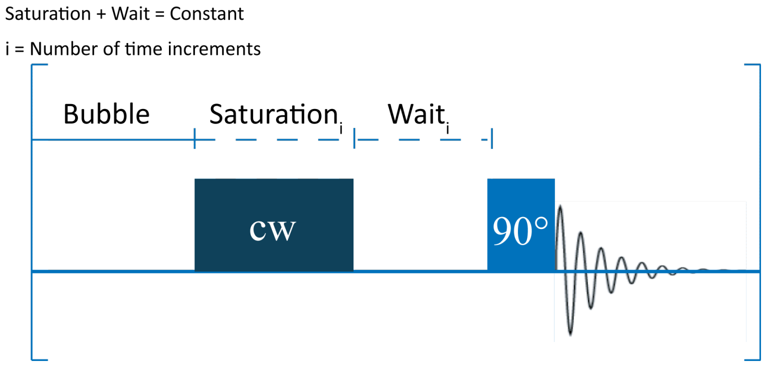

Figure 5.2: Saturation Pulse Delay Sequence. A saturation pulse is applied for increasing lengths of time followed by a wait period adjusted to keep the total length of time constant. Signal is generated using a 90 degree pulse.

5.1 Saturation Curves as a Function of Temperature

One way to monitor the effectiveness of increasing temperature on the contrast generated is to monitor the decrease in signal as the length of the saturation pulse is increased. Figure 5.2 gives a schematic of a pulse sequence that can be used to generate this type of ‘saturation curve’. In this experiment, fresh hyperpolarized xenon is bubbled into a solution containing the sensor. A continuous wave pulse is then applied on resonance with the sensor-associated xenon frequency for increasingly longer periods of time. Following application of the saturation pulse, a wait period is adjusted such that the total length of time from the beginning of the saturation pulse to the detection of xenon in solution is kept constant. Co-adjustment of the length of the saturation pulse and wait period corrects for any signal decay attributed to T_1 relaxation of the hyperpolarized xenon in water. After the wait period, a 90 degree pulse is applied and the free induction decay is collected. To analyze a saturation curve, the FID is Fourier transformed, the area under the bulk xenon in water peak is integrated, and the amplitude is plotted as a function of the length of the applied saturation pulse.

Saturation curves have been studied in great detail by Chavez [30] and have been generated by the author and others to guide development of a full model for the signal depletion expected by applying the Hyper-CEST pulse sequence [107]. In the studies presented below, a 1% xenon gas mixture with natural abundance xenon-129 was bubbled into solution at 65 psi at 20 °C, 25°C, and 37 °C at a variety of concentrations of tetra-glutamate cryA in water. As shown in Figure 5.3A, for a constant concentration of cage in solution, increasing the system temperature depolarizes the aqueous xenon signal more efficiently. Here, the time constant describing the exponential signal depletion as a function of saturation time (T_{sat}) decreased from 1.87 seconds at 20 °C to 0.11 seconds at 37 °C for 150 μM of tetra-glutamate cryA in water. This effect is reflected in Figure 5.3B where 30 μM of the sensor is detectable with a saturation rate constant $T_{sat} = 0.57$ seconds at 37 °C. This effect is encouraging for future experiments conducted *in vivo*.

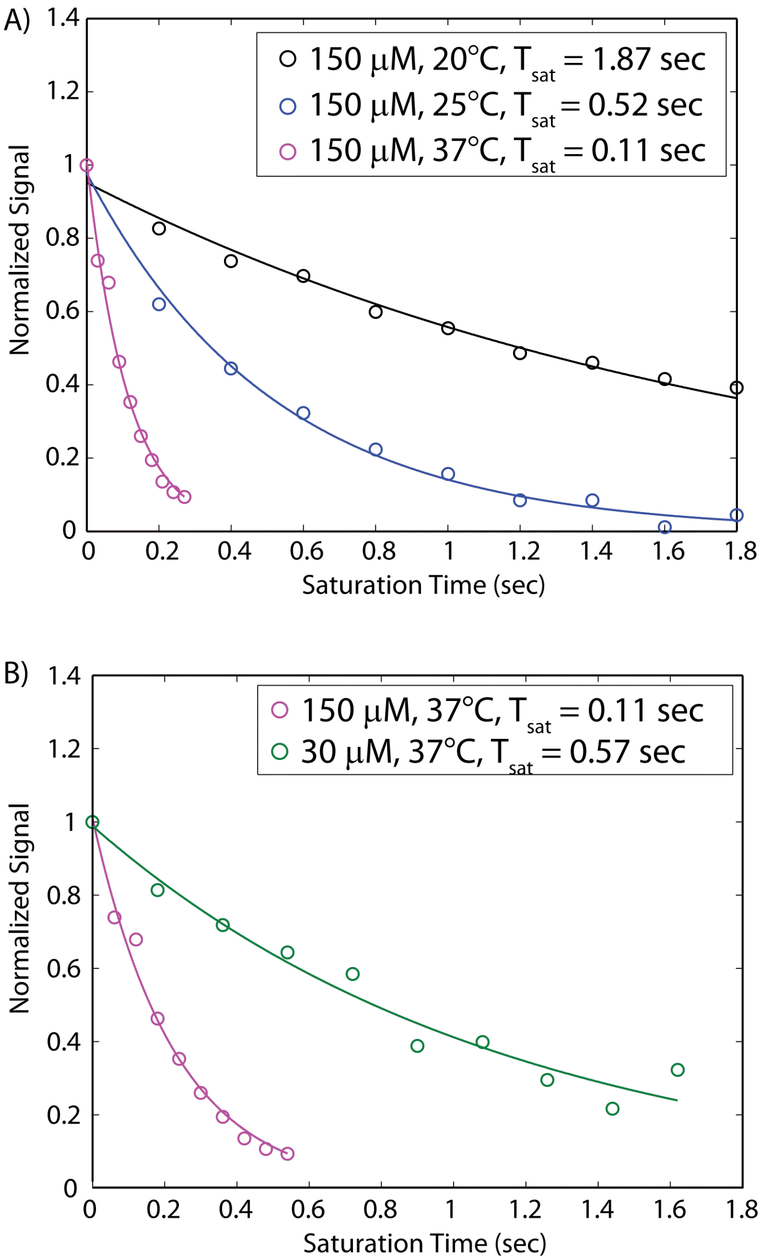

Figure 5.3: Saturations Curves. A) Aqueous xenon signal depletion as a function of the length of saturation time for 150 μM of tetra-glutamate cage in water at 20 °C, 25 °C, and 37 °C. An exponential fit to the data gives the saturation time constant T_{sat} = 1.87 seconds for 20 °C, 0.52 seconds for 25 °C, and 0.11 seconds for 37 °C. B) Aqueous xenon signal depletion as a function of saturation time at 37 °C for 150 μM and 30 μM. The saturation time constant increases from T_{sat} = 0.11 seconds at 150 μM to 0.57 seconds at 30 μM.

5.2 Monitoring the Bulk Xenon Signal as a Function of Temperature

The effect of temperature on the signal depletion generated with the Hyper-CEST technique can be determined by monitoring the bulk xenon resonance frequency following a predefined saturation time as a function of the temperature of the system. In the studies presented here, temperature was kept constant by use of the Varian variable temperature controller associated with the Unity Inova spectrometer. To begin this experiment, 33 μM of a tetra-glutamate biosensor construct in D_2O (Figure 5.4B) was directly detected by bubbling a 1% xenon gas mixture containing a natural abundance of xenon-129 into solution. The gas flow was then pinched at both the inlet and outlet to allow bubbles to settle, followed by application of a 90 degree hard pulse. In 8 averages, both the solution and cage resonance frequencies were detectable: the bulk xenon resonance frequency at 193.8 ppm was detected with a SNR of 185 and the cage-associated peak at 62.7 ppm had SNR = 11 at 295 K (Figure 5.4A). Through direct detection of the spectra at incrementally increased temperatures, the bulk xenon signal was also shown to shift downfield at a rate of 3.0 Hz/K. Furthermore, the xenon at cage resonance is found to shift linearly downfield at a rate of 26.6 Hz/K and the linewidth increased due to exchange broadening with increasing temperature. This downfield shift for the cage-associated xenon resonance frequency with increased temperature confirms the shift seen in Lowery, et al. for a positively charged sensor [83].

In addition to directly monitoring the xenon spectra as a function of temperature, the xenon at water peak was assessed following a Hyper-CEST pulse sequence with a constant saturation pulse as a function of temperature. The saturation pulse implemented in this study had an amplitude of $B_1 = 6.48\ \mu T$ with a bandwidth of 0.93 ppm as estimated by $1/\tau_{\text{pulse}}$ and was varied in frequency to match the sensor-associated resonance at each temperature as described above. A 1% xenon gas mixture was bubbled into solution followed by a short wait period to allow bubbles to settle. The saturation pulse was applied for a constant 500 ms at the cage resonance frequency followed by a 90 degree hard pulse. For each experiment, the system temperature was changed by adjusting the variable temperature parameter on the spectrometer and a total of 7 minutes per temperature increase was used as an equilibration period. Starting at $T = 287$ K, the temperature was increased in steps of 2 K to 313 K (Figure 5.5A). The sample was then cooled to 287 K at twice the rate that it was heated, followed by adjustment to room temperature. Exchange line broadening associated with increased temperature (Equation 4.14) causes the linewidth for temporarily bound xenon to increase from 40 Hz at 295 K to 74 Hz at 313 K. Therefore, the signal of the xenon in water peak was integrated over 70 Hz in order to correct for this variation in linewidth at different temperatures. The signal response, $I_{res}(t)$, is clearly the inverse of the input function $T(t)$ (Figure 5.5B) corresponding to increased depolarization transfer upon increasing temperatures and vice versa.

In order to calibrate the temperature sensitivity of this biosensor construct, the data from Figure 5.5B were used to plot I_{res} versus T as shown in Figure 5.6A where the signal intensity from an acquisition without a saturation pulse was used to normalize the data. The

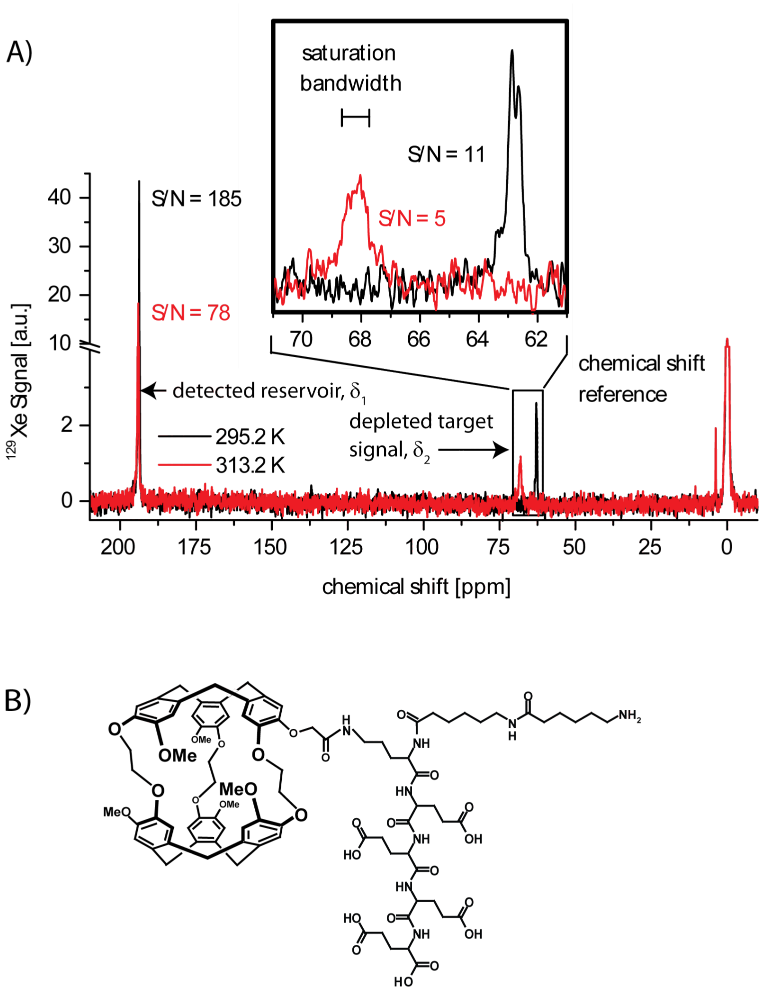

Figure 5.4: Direct Detection of Temperature Effects. A) ^{129}Xe NMR spectrum illustrating that only a small fraction of xenon is associated with a functionalized cryptophane cage at 33 μM cage concentration. Increasing T from 295 K (black spectrum) to 313 K (red spectrum) shifts the signal of encapsulated xenon by ca. 5.5 ppm and induces accelerated chemical exchange that causes line broadening and decreases S/N. B) Chemical structure of the functionalized cryptophane cage used in this study, which we refer to as tetra-glutamate cage.

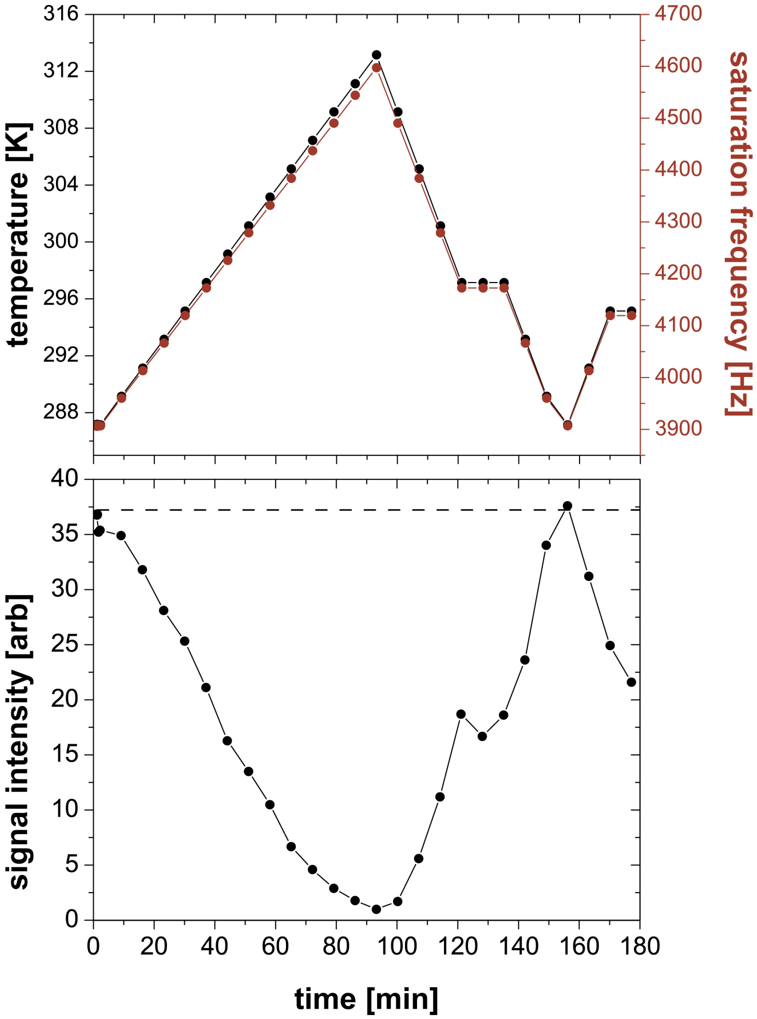

Figure 5.5: Hyper-CEST Response to Temperature Ramping. A) Input function $T(t)$ (black solid line) for Hyper-CEST signal transfer using the tetra-glutamate construct. The saturation frequency offset (red dashed line) is adjusted according to the resonance shift of 26.6 Hz/K. Bars indicate the bandwidth of the saturation pulse of $\Omega = 76.7$ Hz (0.925 ppm). B) Response $I_{res}(t)$ to $T(t)$. Varying the temperature changes ^{129}Xe signal transfer through the cage that is present at 27.2 μM. The reference signal for no saturation transfer is illustrated by the dashed line.

temperature dependence of the signal can be modeled by the sigmoidal Boltzmann function

$$I_{res} = A_1 + \frac{A_2 - A_1}{1 + e^{(T-T_0)/dT}}. \tag{5.1}$$

The constants were empirically determined to be $A_1 = 0.04 \pm 0.04$, $A_2 = 1.00 \pm 0.05$, $T_0 = (297.5 \pm 0.5)$ K, and $dT = (3.9 \pm 0.6)$ K^{-1}. Taking the derivative of this function yields the differential temperature sensitivity dI_{res}/dT plotted in Figure 5.6B (solid line), showing a maximum sensitivity of 6%/K near 297.5 K.

The differential sensitivity is controllable to some extent by adjusting certain system parameters. For example, lower cage concentrations, shorter saturation pulses, or lower saturation power would all yield less efficient saturation transfer at a given T, thus shifting the Boltzmann function to higher temperatures. This was demonstrated with a solution of 11.2 μM cage concentration. As seen in Figure 5.6A, the overall saturation is decreased and the Boltzmann transition stretched over a wider temperature range. In addition, the range of maximum sensitivity is shifted by 6.2 K to give a high-T sensitivity (Figure 5.6B, dashed line).

The significant increase in saturation transfer upon increasing temperatures as shown in Figure 5.6A can be used to detect very low concentrations of caged xenon. To determine the detection threshold for this construct at body temperature, a solution of 10 μM cage was prepared. Figure 5.7 illustrates that Hyper-CEST induces a signal decrease of 16% with this concentration after a 20 second saturation pulse $B_1 = 25.8\ \mu T$ (544 Hz) where the standard deviation of the signals detected with off-resonance saturation was 3.6%.

Estimation of the sensitivity gain using a Hyper-CEST pulse sequence compared to direct detection as shown in Figure 5.4 is summarized in Table 5.1. The xenon occupancy of the cage calculated using the equilibrium constant K = 6000 M^{-1} [55] is 53%. Cryptophane cage occupancy should be considered when designing cages with different affinities for the noble gas [66]. The saturation transfer observed in Figure 5.7 is caused by a concentration of caged ^{129}Xe that is only 1.4 nM. Even through the SNR of direct detection at 310 K will be slightly higher than that at 313 K (ca. 6 instead of 5.1), this comparison still yields a 4000-fold sensitivity enhancement with respect to direct detection.

Under the conditions described in this section, exchangeable, hyperpolarized xenon NMR is much more sensitive than optical methods in this specific case. Conventional, benchtop UV-visible absorbance detection of the cryptophane-A cage ($\epsilon = 8000 M^{-1} cm^{-1}$), requires a minimum concentration of ∼1 μM for detection of the construct. Thus temperature-controlled depolarization transfer using the Hyper-CEST technique is very promising for new applications of high-sensitivity NMR with functionalized biosensors.

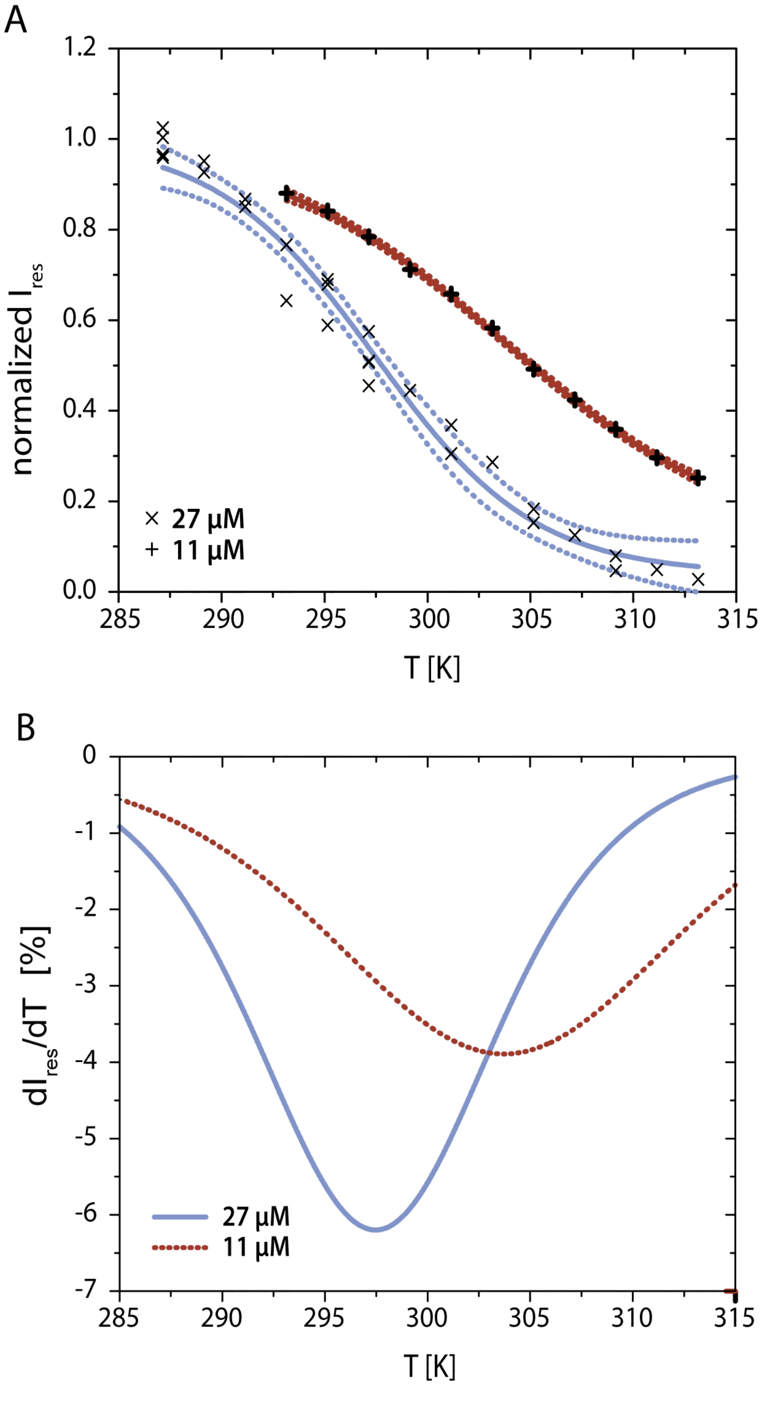

Figure 5.6: Temperature Sensitivity. A) Calibration for temperature sensitivity of I_{res} shown in Figure 5.5B at 27.2 μM cage concentration (x) and for 11.2 μM cage concentration (+). The signal intensity is normalized to a control experiment without saturation pulse. Data are fitted to Eq.5.1 and shown with a 95% confidence band (dashed lines). B) The differential sensitivity of ^{129}Xe signal, intensity change per kelvin, is given by the first derivative of the fit results in (A). Reducing the concentration of the cage construct shifts the maximum sensitivity to higher temperatures. Since the experimental SD in determining I_{res} is 3.6%, the temperature resolution is limited to ca. 0.6 K for the 27.2 μM solution.

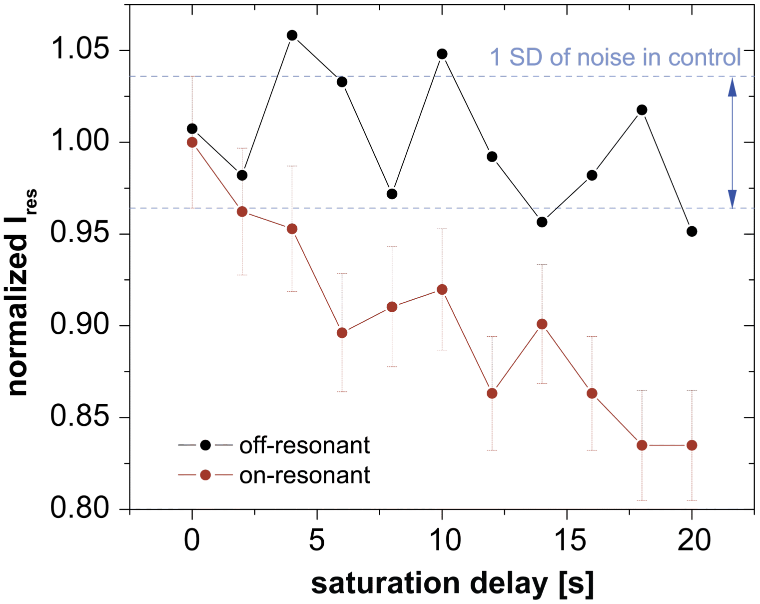

Figure 5.7: 10 nM Sensor Detection. High-sensitivity detection of 1.4 nM encapsulated xenon signal (10 nM cage present) in D_2O at 310 K. The SD in the control data set is 3.6% and is systematic noise due to imperfections in xenon delivery. Maximum signal depletion is 16% of a resonance that was detected with a SNR of 110. However, the limiting factor for the Hyper-CEST detection is the variability of 3.6% in the off-resonance experiment, so SNR for indirect sensor detection is 16.5/3.6 = 4.6.

Table 5.1: Sensitivity Enhancement with Hyper-CEST. Experimental parameters for comparison of direct and indirect detection. The amount of detectable, encapsulated xenon, i.e., $[^{129}\mathrm{Xe}]_{cage}$, is determined by the concentration of the cryptophane cage, the abundance of the isotope ^{129}Xe (26%), and the xenon partial pressure of the gas above the solution. The final acquisition time is determined by the number of scans and the repetition time TR.

	Direct Detection	**Hyper-CEST Detection**
[cage] [nM]	33,500	10
$[^{129}\mathrm{Xe}]_{cage,max}$ [nM]	8710	2.6
$[^{129}\mathrm{Xe}]_{cage}$ at 58.4 mbar [nM]	4616	1.38
No. of scans	8	2
TR [s]	33	53
S/N	5.1	4.6
T [K]	313.2	310.2

5.3 Imaging Temperature Effects with Hyper-CEST

In addition to the spectroscopic effects described thus far, the utility of these sensors as potential contrast agents *in vivo* was tested by conducting a magnetic resonance imaging experiment. Here, datasets were conducted on a 7.05 T NMR spectrometer (Varian Inova) with a 10 mm probe tuned to both xenon (83 MHz) and protons (300 MHz) at this field and a gradient coil assembly for spatial encoding. A two-compartment phantom, one containing avidin-labeled agarose beads (Immobilized Avidin, Pierce Biotechnology, Rockford, IL) and the other containing the biosensor bound to the beads at a 50 μM effective concentration, was perfused with water at a steady 6 mL/min. This water was heated before entering the magnet with a 60 cm heating cable (BH Thermal Corporation, Columbus, OH) and was saturated by the hyperpolarized gas mixture at 0.65 SLM immediately before entering the phantom. A thermocouple attached to the outlet channel of the phantom was used to read the temperature of the water directly leaving the bead volume. The maximum achievable temperature of the water was 305 K owning to the need to keep the heating cable outside of the magnet and because of poor thermal conductivity of the tubing guiding the water.

A two-channel continuous water flow phantom was prepared in a similar fashion to the initial Hyper-CEST experiments [116]. Here, the base of an 8 mm NMR tube was divided into two regions by folding transparency paper into an ’S’ configuration. One of the resulting sections was filled with 6% cross-linked agarose beads while the other section was filled with the same volume of agarose beads grafted with 50 μM cage. Xenon dissolved in water flowed through the system at 6 mL/min as monitored manually by timed collection in a graduated cylinder. ^{129}Xe Hyper-CEST images were acquired using a 1.5 second cw-pulse of 1.6 μT amplitude and a slice selective 90 degree pulse along the z-dimension (2 ms sinc shape, 10 mm slice thickness) with subsequent two-dimensional phase encoding (12 × 12 mm^2 field-of-view, matrix size 8 × 8 FIDs, 10.8 min acquisition time). Each point in k-space was read out once for 64 ms with 100 kHz spectral width.

In this experiment, a saturation bandwidth of only $\Omega \approx 30$ Hz was used to depolarize xenon nuclei within the cage. A saturation pulse with this bandwidth should yield ineffective saturation at $T \approx 300$ K but effective depletion transfer at slightly increased temperatures. ^{129}Xe MRI datasets were collected using a chemical shift imaging pulse sequence. Figure 5.8A shows a coronal ^{1}H MR image of the system with two samples of agarose beads, one sample labeled with the biosensor. The signal of xenon at 193.6 ppm (aqueous solution with agarose) can be detected in a single-shot slice-selective spectrum (Figure 5.8A) and allows the spatial distribution of the microscopic beads to be displayed selectively (Figure 5.8B). In contrast, substantial line broadening (Figure 5.8D) and low concentration make the biosensor signal around 65 ppm undetectable without substantial signal averaging (Figure 5.8E).

Figure 5.9 illustates the expected temperature-gated amplification for sensor detection. At 299 K, the Hyper-CEST depletion is less effective, as demonstrated by the signal-to-noise ratio in a spectrum from the sensor-labeled compartment - when comparing on-resonant with off-resonant saturation, the SNR changes only by 8%, which is within the noise level for this experiment. Increasing T by 3 K results in a significant rise in flow through the gate

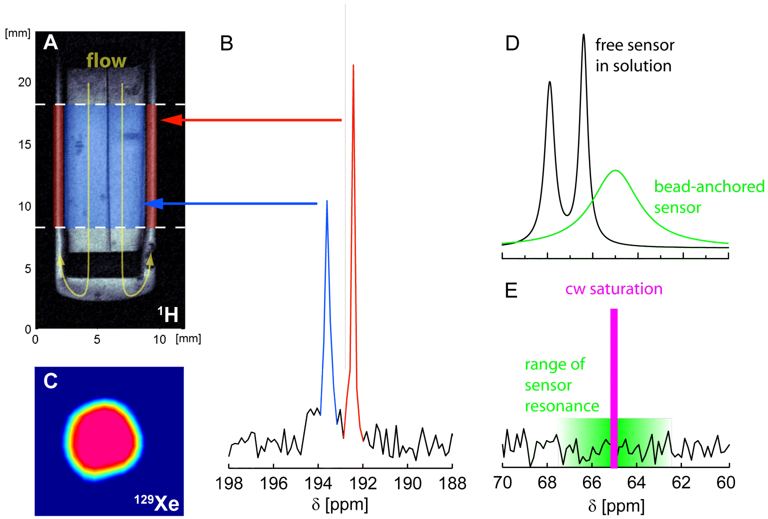

Figure 5.8: Conditions for ^{129}Xe MR imaging of functionalized cryptophane cages targeting microscopic beads. A) ^{1}H coronal image (12 x 24 mm^2 field of view) of the perfusion phantom showing the 10 mm transverse slice for xenon imaging (colored overlays). The center volume with the agarose beads is split into two compartments, only one of which contains the functionalized cryptophane-A cage. The agarose-filled part of the slice (blue) is the source of the resonance at $\delta = 193.6$ ppm, and the surrounding part of the outlet gap (red) is the source of the peak at $\delta = 192.5$ ppm. B) Single-shot slice-selective ^{129}Xe NMR spectrum showing the signals from the two colored regions in (A). C) Transverse ^{129}Xe image (12 x 12 mm^2 field of view) generated from the peak at $\delta = 193.6$ ppm showing distribution of the agarose beads. D) Lineform changes of the biosensor signal upon immobilization to microscopic structures such as agarose beads (schematic spectra with representative line widths reported in [83] and [116]). E) The biosensor resonance of ca. 210 Hz linewidth at $\delta = 65$ ppm (green box) is below the noise threshold (high-field part of the spectrum in (B)). However, a low-power saturation with $B_1 = 1.6\ \mu$T (corresponding to a saturation bandwidth of about 30 Hz; pink bar) will yield efficient saturation transfer at high temperature (see Figure 5.9).

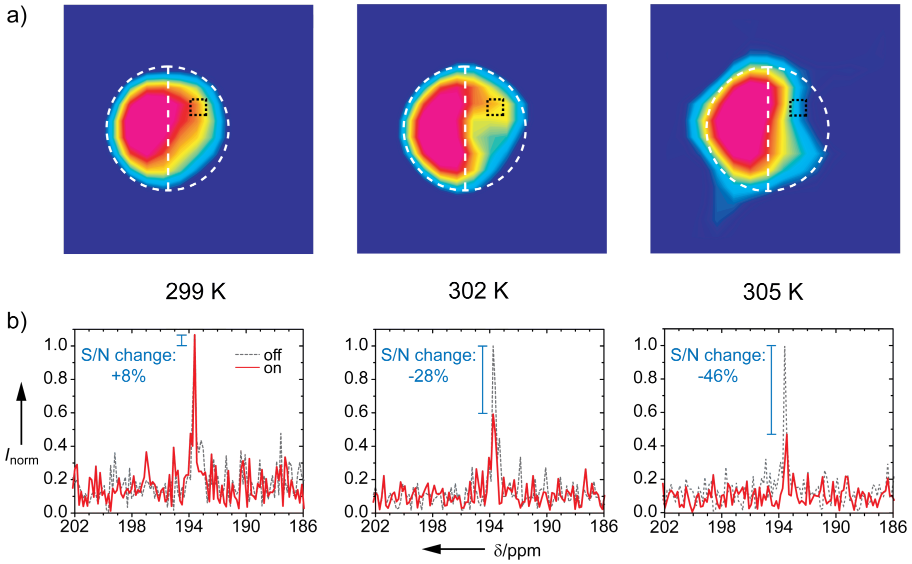

Figure 5.9: Application of the transpletor concept for temperature-sensitive molecular imaging. Compartments are indicated by white dotted lines. A) Transverse ^{129}Xe images show increasing contrast when the temperature is raised from 299 K to 305 K. The right compartment contains the biosensor with the functionalized cryptophane-A cage that responds only weakly to on-resonant saturation with $B_1 = 1.6\ \mu T$ for 1.5 seconds at 299 K. A higher temperature enhances the Hyper-CEST contrast and leads to significantly more efficient saturation. B) Corresponding spectra from the center of the right compartment (black dotted square) show the signal change for on-resonant saturation (red spectra; compared to black data for off-resonant saturation) at different temperatures. Whereas the SNR ratio is almost unchanged at 299 K, a signal decrease of 46% can be achieved after increasing the sample temperature by 6 K.

and consequently a 46% signal depletion, clearly emphasizing the sensor-free compartment on the left.

These data illustrate that despite the reduced exposure time of nuclei to the cage environment, there is a significant increase in signal contrast at higher temperatures. Substantial line broadening of the bead-associated sensor is not an issue in this case as inhomogeneous line broadening, caused by immobilization, does not impede efficient saturation. Detecting structures of micrometer size becomes feasible with this technique, whereas conventional NMR readout fails to acquire even sufficient proton signal for localization of macromolecules.

5.4 Acknowledgements

The results of these temperature-dependent experiments were published in two peer-reviewed journal articles ([117], [118]) and are presented here with permission by the authors.

Chapter 6

Remote Detection of a Xenon-based Molecular Sensor

Remote detection of MR signals has expanded the range of NMR spectroscopy beyond the standard experiment. Traditionally, signal in an NMR experiment is both encoded and detected with the same coil. As described in Section 2, it is advantageous to separate these steps in flow-based experiments were the sample is mass-limited or where the filling factor for detecting the sample is low relative to the total volume of the encoding region.

A natural extension of the proton and xenon gas experiments is to remotely detect xenon dissolved in water. This would make interrogating systems such as xenon-based molecular sensors bound in high concentration to polystyrene beads possible and is a necessary step towards the detection of sensors on a microfluidic chip. In order for aqueous xenon experiments to succeed, a remote detection probe tuned to the resonance frequency of xenon was required that took advantage of design advances put in place since the initial gas experiments in 2005. Furthermore, a method to dissolve xenon into gas in close proximity to the encoding region was required. This chapter describes the construction of a remote detection probe for aqueous xenon experiments and methods developed for dissolving xenon into water. Furthermore, the first time resolved remote detection travel curves of xenon dissolved in water and remote detection of a xenon-based molecular sensor are presented.

6.1 Remote Detection of Aqueous Xenon

6.1.1 Single Resonance Detection Probe Construction

The first constraints to be considered for this system were physical in nature. Although the commercial 30 mm probe used for encoding has an open bore, the single resonance probe built for this experiment was inserted from the top of the magnet due to space restrictions when inserting the chip and electronics from the bottom. Additionally, it is advantageous to exchange xenon into solution within the bore of the magnet in order to preserve polarization - a condition met with a top-down probe. The physical configuration of the Unity Inova 7 T magnet is given in Figure 6.1. Here, the commercially available 30 mm probe (45 mm O.D., 30 mm I.D.) used to encode the aqueous xenon was placed within a gradient stack (73 mm O.D., 45 mm I.D.) which was itself placed within the system's shim stack (89 mm O.D., 73 mm I.D.). From the top of the bore of the magnet, the distance to the shim stack is 23.25 inches, the distance to the gradient stack is 23.5 inches, and the distance to the top of the 30 mm probe is 27.5 inches.

The design for the single resonance probe was based on the proton-based remote detection studies described by Harel [59]. Originially, a solenoid microcoil was wound around a 500 μm silica sleeve that allowed passage of 360 μm capillary tubing and acted as a rigid support for this tubing. To wind the microsolenoid, one end of the 500 μm silica sleeve was attached to a hand-held drill, while the other was held loosely in place with a vice. The silica was slowly rotated while holding tension on 34 gauge copper wire, such that the wire slowly wound itself around the silica sheath. Following winding, the solenoid was glued in place on the silica support using quick-dry epoxy. Finally, the microsolenoid was carefully reduced to 13 turns, matching the specifications used in Harel, et al.'s proton-based experiments [59]. The 13 turn coil made for this experiment had a total length of 6 mm. This coil was housed in a sealed container that could be filled with Fluor-Inert, a fluid susceptibility matched to water, to avoid extensive line-broadening due to the air-liquid interface surrounding the coil.

Due to problems with initially detecting an aqueous xenon signal described below, the coil and fluid holder were replaced with a four turn coil made of 22 gauge wire wrapped around 1/16 inch tubing in order to increase the number of spins within the detection probe. Using Equation 3.2, for a 2% xenon gas mixture with a natural abundance of xenon-129 and xenon pressurized to 65 psi at 293 K, the concentration of xenon-129 in water is 145 μM. Therefore, switching from the microcoil to the 1/16 coil tubing increased the number of spin active nuclei from $9.26*10^{12}$ to $3.49*10^{14}$.

The leads of the copper wire were soldered onto a printed circuit board (PCB) designed to place a 1 - 40 pF variable tuning capacitor (Johanson) in parallel with the inductive solenoid and a matching capacitor in series [59]. This circuit was firmly mounted to a thick Teflon base that fit into a copper hat used to shield the electronics in the detection region from cross-talk due to pulsing at the same frequency with the encoding probe. Power was delivered to the circuit by splitting one end of a BNC cable such that the active lead was soldered to the copper pad of the PCB directly connected to the matching capacitor, and the grounding braid was soldered to the grounding plate. Finally, the circuit was tuned by adding chip capacitors in parallel with the inductive solenoid coil and the tuning capacitor.

Matching the design from Harel [59], the Teflon base holding the electronics was mounted to a brass support with through holes for the BNC cable to power the system and 1/8 inch G-10 rods for tuning and matching the circuit. A new method for making the tuning rods was devised where a 7/64 inch hole approximately 1/4 inch deep was drilled into the rods (Note: wear a mask when doing this! G-10 is a fiberglass and consequently is not very nice to inhale). Drilling the holes can be accomplished using a lathe or carefully by hand using a mount and a hand drill. Ceramic tips (Aven) were glued into the holes using a small amount of quick-dry epoxy. This design overcame previous issues with tapered G-10 tips wearing

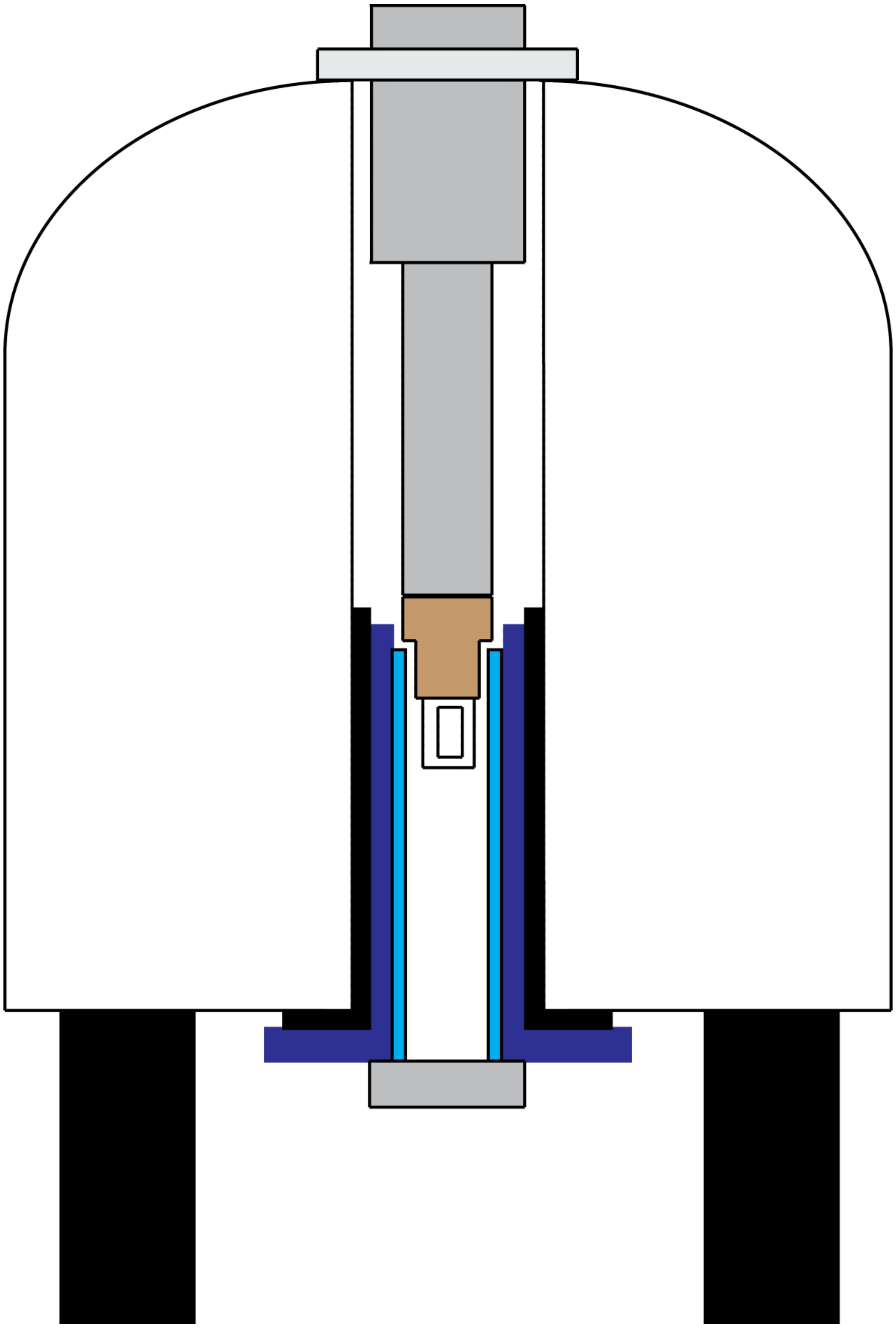

Figure 6.1: System Schematic

down over time and tips breaking off of the tuning rods.

The brass support and Teflon base were housed in an aluminum can that was connected by 2-56 screws to both the brass support and to the copper hat surrounding the RF electronics [59]. This can acted both as a spacer and as an effective means for grounding the electronics. Finally, the brass support was attached to a three-slotted aluminum bird cage to which a sliding aluminum disk could be held in place with 6/32 inch screws. This piece allowed for fine adjustment of the positioning of the encoded sample into the sweet spot of the magnet.

6.1.2 Xenon Dissolution

Aside from constructing a remote detection probe tuned to the resonance frequency of xenon, one of the first challenges was devising a method for dissolving xenon into water close to the encoding region. The necessity of the close proximity of the dissolution to the encoding region is due to the non-negligible 45-60 second T_1 of xenon in water. The first system for dissolution of xenon into water considered involved the use of Membrana Micromodules®. These commercially available membrane cartridges contain hydrophobic polypropylene X-50 fibers that have a 300 μm OD, 220 μm ID, are 40% porous, and are available in a variety of bundle sizes. The drawback of the cassette was that it was too large in diameter to fit into the gradient stack once Swagelok connections were made to attach the gas lines in and out. For this reason, the Membrana cassettes were initially abandoned as a viable option.

Due to the physical space restrictions of the detection probe in the bore of the magnet above the detection region, a home-built gas-exchange system was initially designed to fit within the bore of the 30 mm encoding probe. This was quite the challenging feat! In time, an intricate design was decided upon that was fabricated by Jim Breen, the glassblower for the College of Chemistry. Membrana kindly donated a mat of X-50 fibers for this and similar projects that consisted of individual X-50 fibers woven together in regular intervals. The gas-exchange design consisted of a short ∼2 cm piece of 1/8 inch glass tubing with standard number 7 Chem-thread fittings at either end through which a bundle of 50 X-50 membranes could be passed (Figure 6.2). The glass inlet and outlet ports where attached to the 1/8 inch tubing and then bent at right angles to keep within the space constraints. After passing the Chem-thread for the liquid in connection, the gas lines were tapered in so that the functional segment of Wilmad high pressure/vacuum NMR tubes could be attached. These connectors have a threaded gas tight Teflon adapter with Swagelok connectors for the gas in/out lines. As in the larger Membrana gas-exchange membrane systems, the gas flow was driven counter to the direction of the water flow and the gas pressure was kept below the water pressure in order to avoid bubbling. A thin copper hat that fit over the gas-exchanger was made to avoid depolarization of xenon during the encoding pulses as the exchanger was intended to sit inside of the encoding probe. The hat was constructed so that it could be screwed onto a Teflon microfluidic chip holder. For the experiments planned using this gas exchanger, the final assembly from the top of the magnet consisted of the detection probe attached to the microfluidic chip holder which was itself attached to the xenon gas exchanger.

This setup may have worked in time, but the initial experiments did not succeed due to a number of expected and unexpected problems. First, the glass exchange system was incredibly fragile. Making pressure-tight membranes by gluing bundles cut from the mat of Membrana X-50 fibers at both ends was challenging due to the strict space constraints, only one set of membranes could be made at a time, and the glass inlet and outlet ports for the gas mixture were constantly at risk of snapping. Then, the copper hat initially included to shield the polarized xenon from pulsing at the aqueous xenon resonance frequency induced large eddy currents when placed in the magnet making the assembly hard to insert. Furthermore, use of this hat changed the resonance frequency of the encoding probe past the range for which it could be tuned to protons for shimming. Finally, the Teflon screws connecting the gas exchanger to the microfluidic chip holder were not strong enough to bear the weight of the copper shield plus the membrane system. Unfortunately, brass screws could not be used as they would quickly strip the threads on the chip holder rendering it unusable after only a small number of experiments. Therefore, the copper hat housing the gas exchange system was glued to the chip holder with care taken to glue it parallel to the long axis. At this time, the system was deemed impractical and alternative methods for dissolving xenon into water were re-evaluated.

For a short amount of time, Membrana MicroModule®gas exchange membranes were reconsidered for use in dissolving xenon into water close to the encoding region. Here, pressure driven water flowed longitudinally through the membranes while xenon gas passed orthogonally over the membranes. The Membrana MicroModule®membranes worked well for short periods of time, but there were a number of problems associated with their use. First, the cassettes were only rated to 45 psi, but for the experiments described herein water was typically pressurized to 70 psi with xenon at 60 psi. Consequently, the cassettes were prone to cracking. As described above, when Swagelok connectors were attached to the original gas inlet and outlet ports, the system was too wide to fit within the bore of the gradient stack when attached to the remote probe. Therefore, it was necessary to cut off half of the sidearm ports and connectors were glued rather than swaged on. These sites were inflexible and often lead to leaks.

Shortly after the first Membrana runs, a homebuilt membrane system was re-designed and constructed. A separate series of experiments with bundles of the X-50 membranes showed that the aqueous xenon signal detected following dissolution of xenon into water with a bundle of membranes was approximately 25% of the signal detected by bubbling xenon directly into solution [114]. While not as efficient as saturating water with hyperpolarized xenon, the membranes were a reasonable alternative given the system's space constraints. The new gas exchange system was designed to match the Membrana MicroModule®gas to liquid volume ratio. Given the ratio of the MicroModule interior to exterior volumes, the gas to liquid ratio

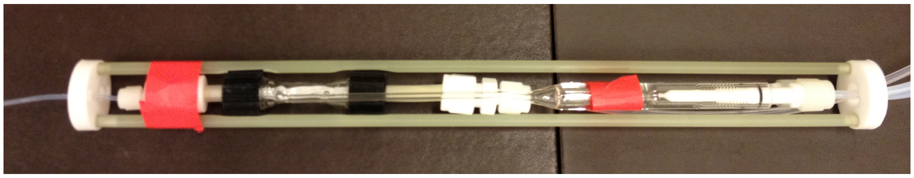

Figure 6.2: Initial Gas Exchange Membrane System

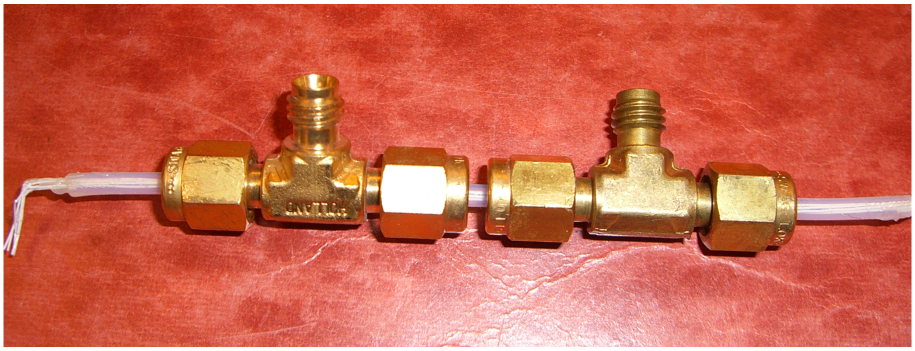

Figure 6.3: Home-built Gas Exchange Membrane System

for this system was approximately 2:1. In a separate, larger Membrana system, the gas to liquid volume ratio is reported to be 1.6:1. For the new homebuilt gas exchange membrane system, 10 membranes were carefully cut away from the mat and were strung through a piece of 1/8 inch teflon tubing resulting in a gas to liquid volume ratio of 1.79. The tubing these membranes passed through was kept short, typically 2-3 cm, to maximize the surface area to volume ratio and minimize the transit time through the membranes and to the detector (Figure 6.3). Both ends of the membranes were then passed through 1/8 inch brass Swagelok T style connectors and another short piece of 1/8 inch tubing. The membranes were potted at each end with epoxy with care taken to avoid clogging the interior of the membranes. After allowing the epoxy to cure, the membranes were pressure and leak checked by allowing pressurized water to flow axially through the membranes with the opposite end terminated. Leaks were typically visible within the first 5 minutes of pressurizing the inlet water line where liquid would begin to fill the region designated for xenon gas. After pressure-checking the new membranes, the gas inlet and outlet lines were connected such that hyperpolarized xenon gas flowed counter to the direction of the longitudinal liquid flow, thus creating a concentration gradient for xenon dissolving into water as it flows through the membranes.

6.1.3 Detection of Xenon in Water

Remotely detecting xenon in water proved to be much more challenging than originally anticipated. The first experiments attempted used the complex xenon gas exchange membranes with a xenon pressure 65 psi and water flowing at a wide range of flow rates. Immediately after passing through the glass gas exchanger, the water was channeled through 3 cm of 1/16 inch tubing which stepped down to 360 μm capillary tubing through the detection region. This experiment was overly ambitious for a first pass, as the probe was not yet calibrated, the resonance frequency needed to be located, and the detection region shimmed. Eventually, a 4 turn solenoid wrapped around 1/16 inch tubing was using to locate the aqueous xenon signal. At this time, the Membrana cassettes were used to exchange xenon into water and 1/16 inch tubing ran from the cassette, through the coil, and out of the magnet. For the initial experiments where an aqueous xenon signal in the detection region alone was sought, the copper hat was not used for shielding RF noise. Here, the water was pressurized to 80 psi and was set to flow at 350 μL/min. Using the MITI polarizer set at

60 psi with xenon flowing at 0.43 SLM, the aqueous xenon signal was localized and using 64 averages with an SNR of 20. A pulse width array was used to calibrate the 90 time which was determined to be 2.0 μs at 52 dB.

6.1.4 Aqueous Xenon Travel Curves

Before the aqueous xenon signal could be remotely detected an external amplifier with 82.9 MHz in its range was calibrated to match the power input of the internal amplifier traditionally used to drive NMR experiments. First, the 180 time was determined to be 240 μs at 52 dB for the 30 mm probe using this internal amplifier. The pulse was then connected through a high power 50 dB attenuator plus a variable series of attenuators that could be switched on or off with a maximum of 30 dB to an oscilloscope and triggered such that the pulse was constantly visible. The peak-to-peak voltage using the internal amplifier with 80 dB total attenuation (300 mV) was used as a reference. The input of the pulse was then connected to the external amplifier and using the same pulse width the power was ramped up from 20 dB until the peak-to-peak voltage on the oscilloscope matched 300 mV at 56 dB. This occurred with a 3 dB attenuator connected directly to the output of the external amplifier in addition to the 80 dB attenuation used to originally calibrate the system.

Following calibration of the external amplifier, the copper hat was attached to shield the detection probe electronics and a microfluidic chip holder was used as a place setting for 1/16 inch tubing wound through the encoding region (Figure 6.4). In this experiment, the output from the membrane cassette was stepped down over a short distance to 360 micron tubing to transfer hyperpolarized xenon to the encoding region as quickly as possible before it was expanded to 1/16 inch tubing at the top of the chip holder. Approximately 10 cm of 1/16 inch tubing was arranged in a serpentine fashion to extend the total aqueous xenon flow path. At a water flow rate of 0.8 mL/min, it was predicted that the aqueous xenon would take four seconds to clear the encoding region - enough time to see well defined features in a travel curve.

The first aqueous xenon travel curve was collected in a ‘stopped flow’ experiment where the 0.8 mL/min water flow was stopped using a solenoid valve placed before the needle valve controlling the flow of water. Xenon gas pressurized to 60 psi was delivered to the membranes. After stopping the flow of the water, a 180 degree pulse was applied in the encoding region. The water flow was then turned on and the aqueous xenon signal was stroboscopically detected in the detection probe. Here, the aqueous xenon signal was collected every 200 ms for a total of 10 seconds. This entire process was repeated 64 times over which the signal was averaged (Figure 6.5A).

Xenon travel curves were processed in a standard manner [53] by cropping the series of FIDs into individual segments. These segments were each multiplied by an exponential function for line broadening, left-shifted if necessary to correct for external, quickly decaying signals, baseline corrected for DC offset, zero-filled to twice the next power of 2 for processing, Fourier Transformed, and finally phased such that the first time point had full, positive

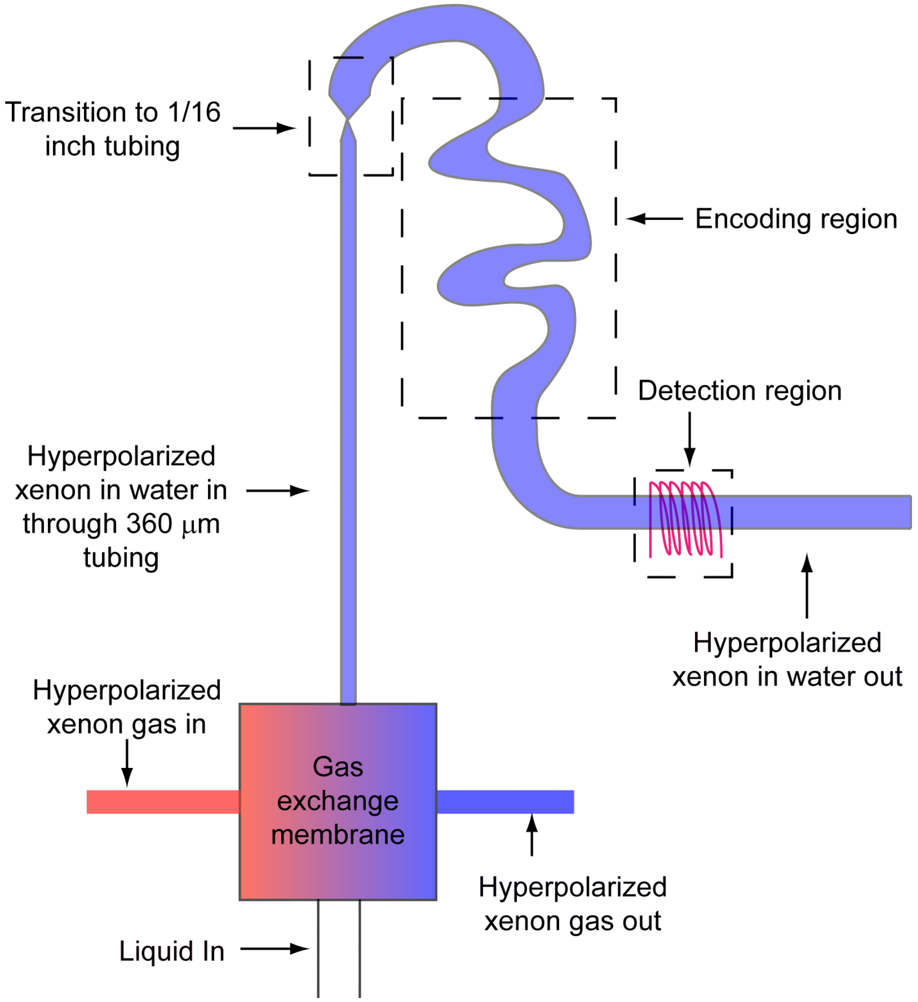

Figure 6.4: Macroscopic Flow Schematic. Hyperpolarized xenon gas is exchanged into water through a gas-exchange membrane system. The aqueous xenon flows through 360 μm tubing to the top of the encoding region where it is expanded to 1/16 inch tubing. The liquid serpentines through the encoding region and then out to the 1/16 inch detection coil.

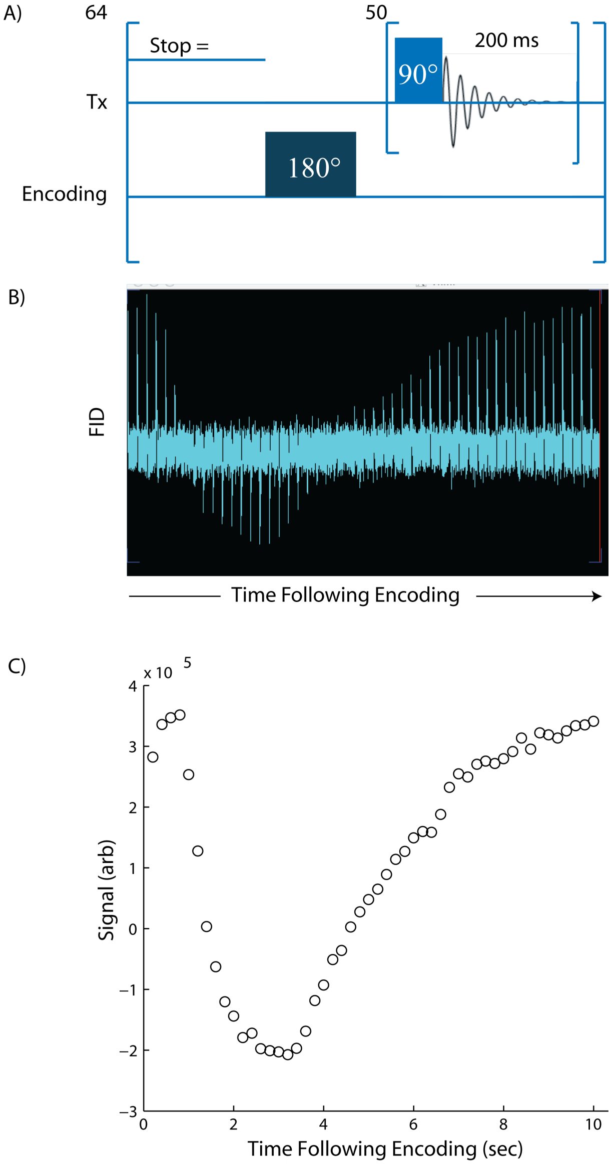

Figure 6.5: Aqueous Xenon Travel Curve. A) A 180 degree pulse in the encoding region was applied following a wait period to allow the water flow to diminish. Following application of the pulse, the encoded xenon was flowed to the detection region where it was detected 50 times in 200 ms increments. This process was repeated 64 times. B) The resulting FIDs indicate a region where spins have been inverted by the 180 degree pulse. C) Processing the FIDs clearly shows the first aqueous xenon signal at full intensity. One second following application of the 180 pulse, the signal begins to decrease in intensity corresponding to regions where the spins that were inverted are averaged into the collected signal. From 2 - 3.8 seconds following application of the 180 degree pulse, a region of fully inverted spins is visible. Around 8.5 seconds following application of this pulse, the integrated signal regains full intensity.

signal intensity. The signal under the resulting curves was integrated over a constant range of the approximate full width at half maximum for the first time point. The FIDs collected in this experiment suggest a region where spins have been inverted by the 180 degree pulse (Figure 6.5B). Processing the FIDs clearly shows the first aqueous xenon signal at full intensity as this signal corresponds to aqueous xenon that was not in the encoding region during the 180 degree pulse (Figure 6.5C). One second following application of the 180 pulse, the signal begins to decrease in intensity corresponding to regions where the spins that were inverted are averaged into the collected signal. From 2 - 3.8 seconds following application of the 180 degree pulse, a region of mostly inverted spins is visible. Finally, around 8.5 seconds following application of this pulse, the integrated signal regains full intensity signaling the end of inverted magnetization.

6.2 Remote Detection of a Xenon-based Molecular Sensor

6.2.1 Macroscopic Xenon-based Molecular Sensor

With an aqueous xenon signal detected, effort was put into detecting a xenon-based molecular sensor remotely. A fellow graduate student attached mono-acid cryA to Advanced Chem Tech TentaGel S-OH beads via a glycine linker. The polystyrene beads had an average diameter of 130 μm and were loaded with approximately 1.3 mM cryA. Sixty microliters of a concentrated bead slurry was loaded into a short piece of 1/16 inch tubing with a syringe. As depicted in Figure 6.6, two 1/16 inch Upchurch unions were used to trap the biosensor beads in this region with the assistance of small pieces of scrubber mesh that blocked the beads at the inlet and outlet from flowing out of the encoding region. During the experiments, the beads were localized near the outlet union due to the pressure driven direction of water flow.

6.2.2 Saturation Travel Curves

In order to remotely detect the presence of the xenon biosensor, the resonance frequency of the cage-associated xenon in the encoding region needed to be identified. Previous studies using a similar sensor in water suggested that the resonance frequency should have been approximately 11 kHz upfield of the xenon at water resonance frequency [118]. For this experiment, the MITI polarizer was set to pressurize the xenon-containing gas mixture to 59 psi at a flow rate of 0.48 SLM and the water at a pressure of 75 psi, was set at 580 μL/min using a needle valve at the outlet. The pulse sequence was made to consist of a short refresh delay period, a saturation pulse loop applied by the encoding probe, and stroboscopic detection using the transmit channel connected to the detection probe (Figure 6.7). Here, a 1000 Hz dsnob pulse was used to saturate incremented resonance frequencies for one second. This saturation frequency was varied in 750 Hz increments around the expected cage-associated xenon resonance until maximum signal depletion was observed.

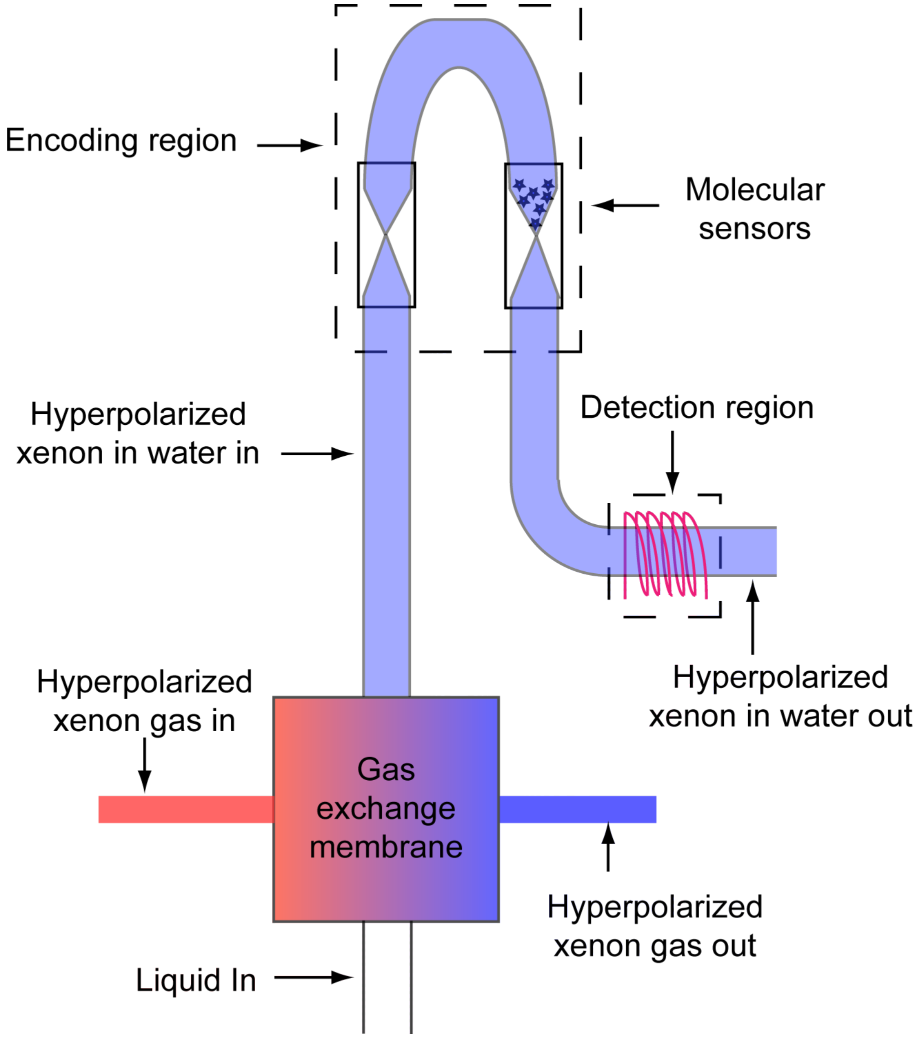

Figure 6.6: Biosensor Bead Schematic. Hyperpolarized xenon gas is exchanged into water through a gas-exchange membrane system. The aqueous xenon flows through 1/16 inch tubing to the base of the encoding region where two Upchurch unions trap the polystyrene beads in the encoding region. Xenon dissolved water flows out of this region to a 1/16 inch solenoid coil.

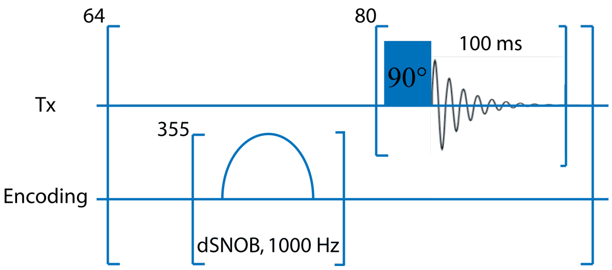

Figure 6.7: Pulse Sequence for Remote Detection of a Xenon Biosensor. A 1000 Hz dsnob pulse is applied for one second at the sensor associated xenon resonance frequency followed by stroboscopic detection of the aqueous xenon signal.

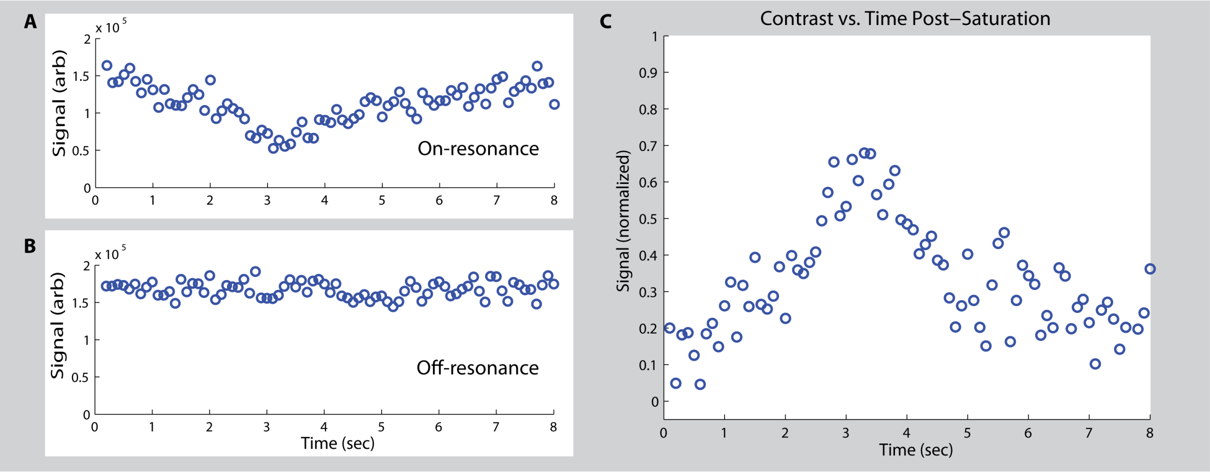

Figure 6.8: Remote Detection of a Xenon Biosensor. A) On-resonance saturation. A 1000 Hz dsnob pulse was applied for one second at the sensor-associated xenon resonance frequency followed by detection of the aqueous xenon signal following termination of this pulse. B) Off-resonance saturation. The same sequence in (A) was implemented applying the saturation pulse equidistant from the aqueous xenon resonance frequency. C) Contrast was generated by subtracting the on-resonance signal from off-resonance case and was normalized to the off-resonance signal at each point in time following the end of the saturation pulse. A region ∼1 second in duration from 2.7 - 3.7 following termination of the saturation pulse displays a maximum of 65% contrast.

As in the Hyper-CEST experiments detailed in Chapters 4 and 5, the dsnob pulse tuned to the resonance frequency of xenon associated with the sensors selectively saturates spins within the bandwidth of the pulse. Subsequent exchange of saturated xenon out of the sensor into the pool of free xenon then decreases the aqueous xenon signal. A 1000 Hz pulse was applied for one second at the sensor-associated xenon resonance frequency (3250 Hz) in the encoding region, followed by eight seconds of stroboscopic detection with the microcoil (on-resonance). This process was repeated 64 times and the averaged free induction decays were processed as described above in MATLAB®. This scheme was then executed with the saturation pulse applied equidistant downfield of the aqueous xenon peak (25,250 Hz) in order to compensate for indirect RF effects (off-resonance).

The integrated signal intensities for the remotely detected spectra over the 8 seconds of acquisition following completion of the saturation pulse indicate regions of aqueous xenon signal depletion using one second of saturation at the sensor-associated resonance frequency (Figure 6.8A) when compared to the off-resonance signal (Figure 6.8B). Maximum signal depletion is expected when the signal in the detection region is in the presence of the sensors for the full duration of the saturation pulse. This corresponded to a travel time of 2.7 - 3.7 seconds following the termination of the saturation pulse. Contrast was generated by taking the difference between the off resonance and on resonance signal intensities, normalized to the off resonance signal (Figure 6.8C). Using the normalized signal intensities, 65% contrast was observed following one second of saturation.

6.3 Discussion

In this chapter a remote detection probe tuned to the resonance frequency of xenon at 7 T was constructed and methods for dissolving xenon into water close to the encoding region were designed and fabricated. Furthermore, the first experiments for remotely detecting aqueous xenon and indirectly detecting a xenon-based molecular sensor were detailed. At an effective concentration of 1.3mM cryA, 65% contrast is obtainable with one second of saturation at the sensor-associated resonance frequency. Additional contrast is expected to be gained upon optimization of flow conditions and reduction of shot noise. These results were encouraging and suggested that remote detection of a xenon-based molecular sensor on a microfluidic chip might be possible.

6.4 Acknowledgements

Membrana kindly donated a mat of X-50 fibers that was used extensively throughout this thesis. Furthermore, a lot of the work presented in this Chapter was accomplished with assistance from (Dr.) Tyler Meldrum to whom I would like to give thanks.

Chapter 7

Towards Remote Detection of a Xenon-based Molecular Sensor on a Microfluidic Chip

In the previous chapter, a single resonance probe tuned to the resonance frequency of xenon at 7 T and a gas exchange system compatible with the physical constraints of the remote detection setup were constructed and assembled to remotely detect the presence of a xenon-based molecular sensor grafted to polystyrene beads trapped in 1/16 inch tubing. This was accomplished by monitoring the aqueous xenon signal depletion following a RF pulse at the caged xenon resonance frequency. Following this proof-of-principle experiment, a plan was devised to detect the presence of sensors on a microfluidic chip as a precursor to the long-term vision of developing a platform for combinatorial screening using xenon-based molecular sensors. Short-term goals included:

* Design and construct a double resonance remote detection probe tuned to both protons and xenon
* Devise a system compatible with adhering xenon-based molecular sensors to a microfluidic chip

7.1 Double Resonance Remote Detection Probe

7.1.1 Design

A double resonance remote detection probe was desired to provide the capability of correlating aqueous xenon time-of-flight information with proton MR images. This functionality is critical as acquiring an aqueous xenon image is not feasible with the 2-5% polarization achievable with the MITI hyperpolarizer. Furthermore, with a probe capable of tuning to both protons and xenon, it is possible to shim the external magnetic field in the region containing the resonance coil. This coil is specifically constructed with a fluid volume slightly smaller than the volume of a microfluidic chip in order to gain time-of-flight information from a remote detection experiment. For a typical microfluidic chip, the fluid volume is

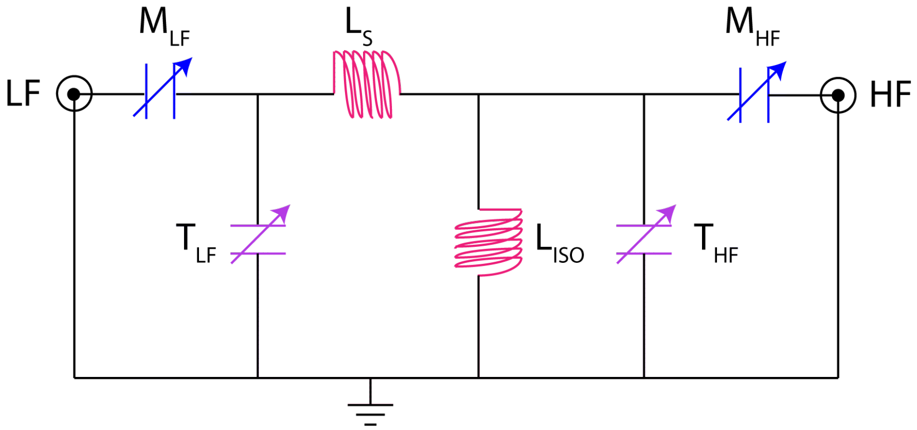

Figure 7.1: Schematic of the resonance circuit used to construct the double resonance remote detection probe used in this thesis. The design is taken from Reference [149].

~100 nL and therefore a microcoil is required to detect the signal of interest.

Multi-resonance circuits compatible with a single microcoil have been implemented by researchers interested in studying NMR on mass-limited samples ([129], [139], [149]). While many circuits for a dually-tuned single microcoil exist, the circuit depicted in Figure 7.1 was selected due to its efficiency and compatibility with the system's physical constraints [149]. Here, a single microcoil was connected the high frequency and low frequency channels to which variable capacitors were placed in parallel for tuning and in series for matching the individual resonances. In place of either transmission lines or a full LC tank circuit, a single inductor was used to isolate the two channels. As long as the inductance of this solenoid (L_{iso}) was much less than the inductance of the sample solenoid (L_s), most of the RF energy was deposited into the sample. Furthermore, the power efficiencies (η) for the high frequency (HF) and low frequency (LF) channels were given by [149]

$$\eta_{HF} = \frac{Q_{iso}L_{iso}}{Q_{iso}L_{iso} + Q_s L_s} \tag{7.1}$$

$$\eta_{LF} = \frac{Q_{iso}L_s}{Q_{iso}L_s + Q_s L_{iso}} \tag{7.2}$$

where

$$Q = \frac{R}{\omega L} \tag{7.3}$$

is the quality factor (Q) for the resonance circuit with parallel coil resistance R at the angular resonance frequency ω. From Equations 7.1 and 7.2, the power efficiency for the low frequency xenon channel is increased with for decreasing values of L_{iso} while maintaining the simultaneously tuned resonance conditions. Zhang, et al. reported quality factors ~200 for circuits using this layout.

The overall layout for the double resonance probe was analogous to the single resonance probe (Figure 7.2). A Teflon base was designed to mount the electronic components to

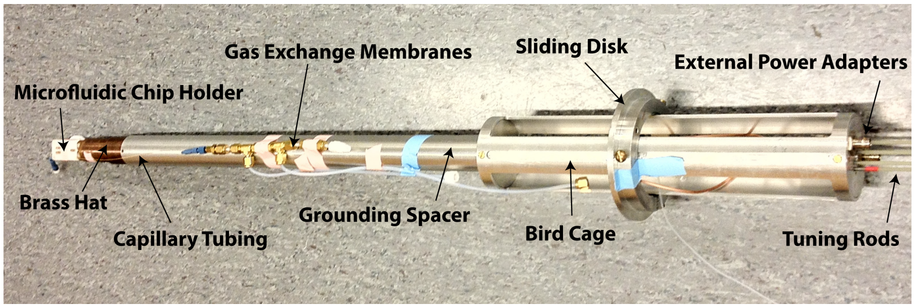

Figure 7.2: Double resonance remote detection probe developed for the work in this thesis.

printed circuit boards as well as allow passage of the input power cables and tuning and matching rods. This base was attached to a brass support that acted as a spacer for physical length over which a hollow aluminum can was attached for grounding. The electronic components in the detection region were shielded from RF pulses applied in the encoding region by a copper hat that was attached to the aluminum can for additional grounding. Then, the brass support was attached to a slotted aluminum bird cage over which an aluminum disk could slide freely, ultimately allowing for fine adjustment of the encoding region within the magnet. Finally, the gas exchange membranes were attached to the exterior of the aluminum can such that the full assembly fit within the 30 mm encoding probe and gradient stack.

In the first layout for this probe, the high frequency and low frequency channels were mechanically isolated by a 1/16 inch Teflon base (Figure 7.3). To test the design of this layout, an 8 turn, 32 gauge copper wire solenoid wrapped around 1/16 inch tubing was used as the sample inductor with 1 - 30 pF Johanson variable capacitors in parallel for tuning the circuits and in series for matching to 50 ohms. A variety of isolation inductors made from winding 4 - 8 turn solenoids made of 22 gauge copper wire wrapped around 1/8 inch tubing were placed in parallel with the sample inductor on the high frequency circuit to electronically isolate the two channels. The circuits were ultimately tuned to 299.76 MHz and 82.9 MHz by adding 20 pF chip capacitors (Johanson) in parallel with the high frequency channel and 25 pF in parallel with the low frequency channel using a 4 turn isolation inductor.

For each frequency, power was delivered to the circuit by threading a BNC cable through the brass support and soldering the active lead to the copper pad on the printed circuit board to which the matching capacitor was attached and the grounding braid to a grounding copper strip on each board. The ends of the BNC cables were terminated at an inline BNC bulkhead mounted to the aluminum plate at the base of the bird cage in order to fully ground the circuits and to isolate the detection probe from the necessary adjustments (tuning, placement, etc.) that would be performed outside of the magnet. Once the circuit was tuned, 1/16 inch tubing was strung from the base of the aluminum birdcage, through the solenoid coil, and then guided through a 1/16 inch through hole in the top of the copper hat such that aqueous xenon could flow in the reverse direction from the encoding region, through the sample inductor, and then out to waste.

This first layout for the double resonance probe proved to be flawed at multiple points.

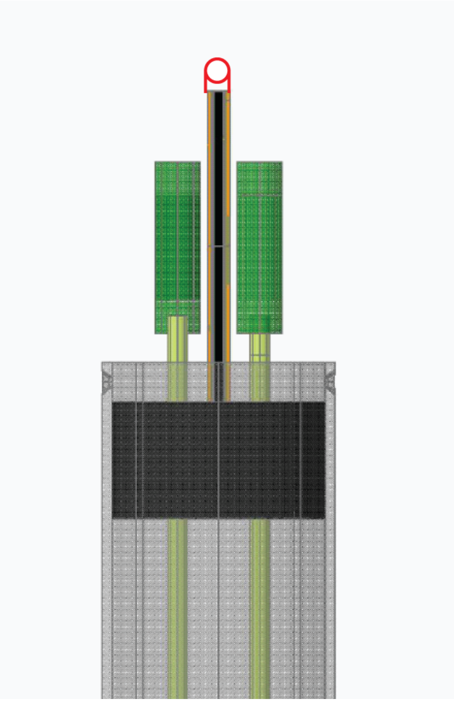

Figure 7.3: First Design - Double Resonance Probe. In this design, the high and low frequency electronic components were separated in space by a thin 1/16 inch Teflon base. A printed circuit board was attached to each side of this base to which the circuit elements were mounted.

First, the lack of a common grounding plate near the RF electronics led to problems calibrating the equipment used to tune and match the resonance circuits, which ultimately resulted in instabilities when tuning the probe. Soldering copper tape around the 1/16 inch Teflon base helped relieve this problem, but care was required to avoid contact of the strip with the copper hat used to shield the electronics. Then, the 1/16 inch inner diameter solenoid was ultimately unsupported and could not hold its orientation perpendicular to the external magnetic field when the 1/16 inch tubing was strung through it. Aside from the lack of orientation, the free-standing coil resulted in observable noise due to mechanical vibrations. Finally, the circuit could not be tuned when housed within the copper hat. Upon further inspection, the 1/16 inch Teflon base was not firm enough to withstand the forces placed on it when tuning and matching the circuit from above. The act of tuning or matching the probe would bend the base, resulting in contact between the variable capacitors and the copper hat. Contact in this manner dramatically changed the capacitance of the circuit and therefore the resonance frequency when tuning relative to the stationary assembly. Thus, the resonance circuits could not be tuned with confidence when placed in the magnet.

The second version of the double resonance probe was designed with all of these considerations in mind. Instead of separating the high and low frequency channels in space, all of the components were fit onto one face of a 1 mm printed circuit board that was originally copper-clad on both sides (Figure 7.4). The layout for the circuit components was designed such that the copper pads on the front face were minimized to avoid additional parasitic ca-

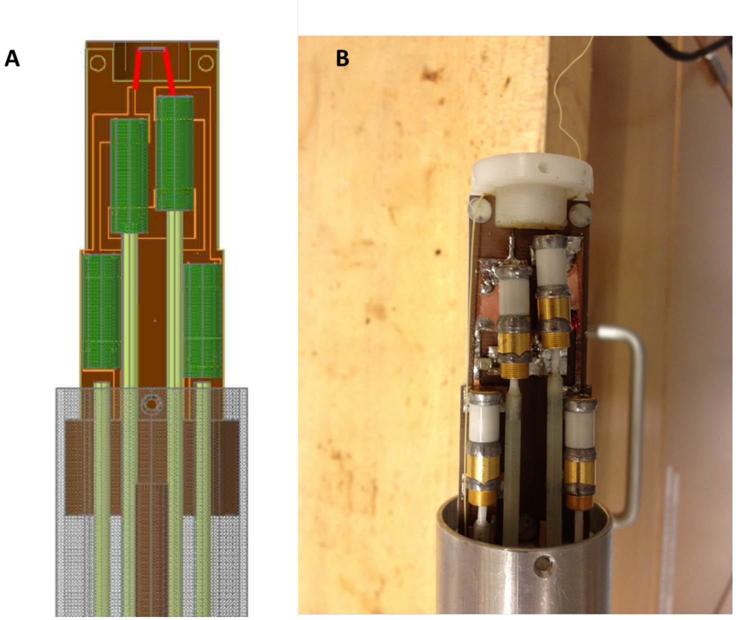

Figure 7.4: Second Design - Double Resonance Probe. A) The AutoCAD layout for the circuit elements such that all components fit onto the same face within the physical constraints of the system. B) The final physical circuit based on this design.

pacitance. Furthermore, all strip-lines on the board were chosen to be 2 mm wide to match a 50 ohm load. This board was ultimately fixed to a solid Teflon base for stability.

7.1.2 Specifications

Similar to the single resonance probe constructed by Harel [59], a well was constructed at the top of the Teflon base to hold a Delrin container supporting a microsolenoid coil (Figure 7.4B). The support for the microsolenoid was made from rigid silica with 500 μm O.D. and 360 μm I.D., through which 360 μm capillary tubing could be threaded. Winding of the microsolenoid was loosely based on the solenoids constructed in Webb, et al. 1996 [139]. In order to wind the microsolenoid, one end of the 500 μm silica support was attached to a hand-held drill, while the other was loosely held in place by a vice. The silica was slowly rotated using the drill while holding tension on 32 gauge copper wire, such that the wire slowly wound itself around the silica support. Following the initial winding, the solenoid was glued in place on the silica using quick-dry epoxy. After allowing the epoxy to dry, the microcoil was reduced to 18 turns - within the goal of 15 - 20 turns that was based on the construction of the single resonance xenon remote detection probe described in Chapter 6.

Once the microsolenoid was wound, the full circuit was constructed by tuning and matching the high frequency channel, adding the isolation inductor, and tuning the low frequency resonance. Once the circuit was in place, the inductance of the microsolenoid was experimentally determined to be ~195 nH using an impedance meter. Using the condition for resonance,

$$f = \frac{1}{2\pi\sqrt{LC}} \tag{7.4}$$

where L is the sample inductance, C is the parallel capacitance, f is the resonance frequency in Hz, and f if the resonance frequency in Hz, the sample inductance combined with the 1 - 30 pF variable tuning capacitor gave a resonance range of 65 - 360 MHz, making additional chip capacitors unnecessary for tuning the high frequency channel to 299.76 MHz. The isolation inductor was made by winding 4 turns of 16 gauge copper wire around 1/8 inch tubing resulting in a measured inductance of 15 - 25 nH. Following addition of the isolation inductor, the low frequency channel required a 20 pF chip capacitor placed in parallel with the sample inductor to tune the channel to 82.9 MHz with the assistance of the variable capacitors. By design, both circuits were attached to a common ground on the back-plate of the copper-clad printed circuit board. Finally, edge-mount SMA connectors (Newark) were used to connect power via SMA cables rather than split BNC cables.

7.1.3 Performance

The performance of the double resonance remote detection probe was measured using an Agilent network analyzer. The quality factor, determined from the 3 dB bandwidth from the tuned and matched resonance

$$Q = \frac{f_0}{f_2 - f_1} \tag{7.5}$$

where f_0 is the resonance frequency, f_1 and f_2 are the frequencies that corresponds to a 3 dB increase in reflected power relative to the on-resonance condition on either side of the resonance on an S11 plot, was determined to be ∼1400 for the high frequency channel and ∼3200 for the low frequency channel. While these numbers are much higher than the expected value of 200, neither ring-up problems such as skewed pulse width arrays nor ring-down problems such as early receiver ringing were obvious in the subsequent spectra. Furthermore, the isolation, or power loss due to leakage of the applied resonance frequency onto the other channel, between the two channels was very good: -33 dB for the high frequency channel and -16 dB for the low frequency channel. Using the power conversion $P_{isolation} = 10\log(P_{out}/P_{source})$, this corresponds to trace leakage on the high frequency line and ∼2.5% on the low frequency channel.

The high frequency channel was tested first by arraying the time that a hard pulse was applied. As discussed in Chapter 2, the 90 degree time occurs when the signal intensity is at a maximum and 180 degree time when the signal sums to zero. A representative result of this type of study is given in Figure 7.5. Here, the pulse width was varied from 0 μs to 7 μs in 0.25 μs increments at 50 dB. The 90 degree time was determined to be 3.375 μs and 180 degree time was 6.75 μs. For a single shot of protons in water, the SNR at 3.25 μs was 324.

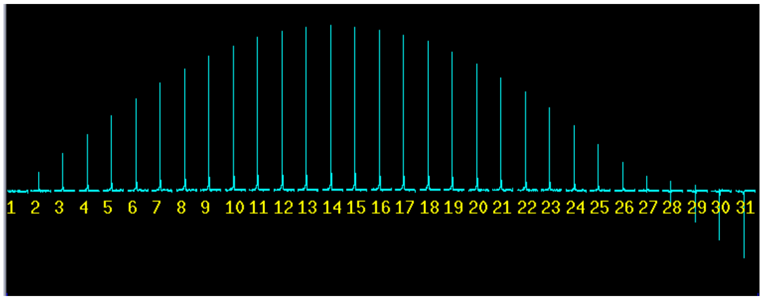

Figure 7.5: Pulse width array for proton channel of double resonance probe. The pulse width is varied from 0 μs to 7 μs in 0.25 μs increments at 50 dB. From this plot, the 90 time is determined to be 3.375 μs.

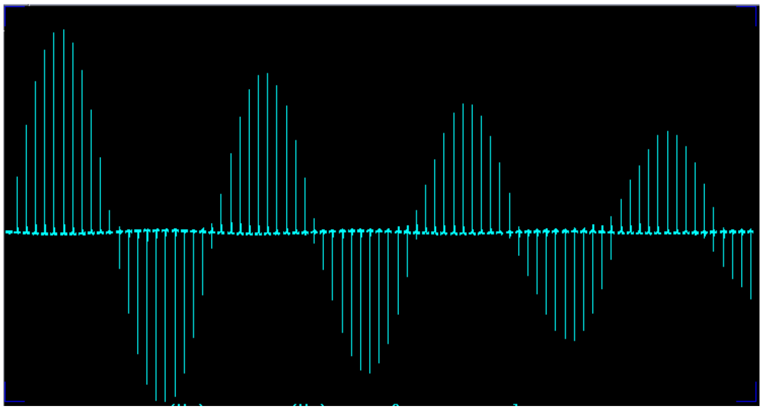

Figure 7.6: The homogeneity of the solenoid microcoil is given by the ratio of signals following a 90 degree and 810 degree pulse. Here, the homogeneity is ∼0.58.

Furthermore, the homogeneity of the coil was tested by comparing the SNR at the 90 degree time to the SNR for an 810 degree pulse (Figure 7.6). For this experiment, the water flow was stopped, and therefore a 10 second wait time was inserted between successive scans to allow the water protons to relax back to thermal equilibrium. Here, the pulse width was arrayed from 0 to 40 μs at 52 dB in 0.5 μs increments. The SNR at the 90 time (3 μs) was determined to be 528, while the SNR at the 810 time (24.5 μs) was 306. Thus, the homogeneity, commonly reported as the ratio of these values was ∼0.58.

Due to the low expected xenon signal in the microcoil, the low frequency channel was first tested using a saturated salt water solution. Sodium-23 is a spin-3/2 nucleus and is 100% naturally abundant in simple table salt. The absolute value of the gyromagnetic ratio of sodium-23 (70.808 rad s^{-1} T^{-1}) is close to that of xenon-129 (74.521 rad s^{-1} T^{-1}) and its resonance frequency at 79.4 MHz is well within the tuning range of the double resonance probe. Salt water was inserted into the detection region by injecting a bolus at the inlet to the detection probe. Using 16 averages, a clear nutation curve was observed for sodium-23 on the low frequency channel (Figure 7.7). Here, the pulse width was arrayed from 0 to 4 μs in 0.2 μs increments at 52 dB. The 90 degree time was determined to be 1.3 μs with an SNR of 27.

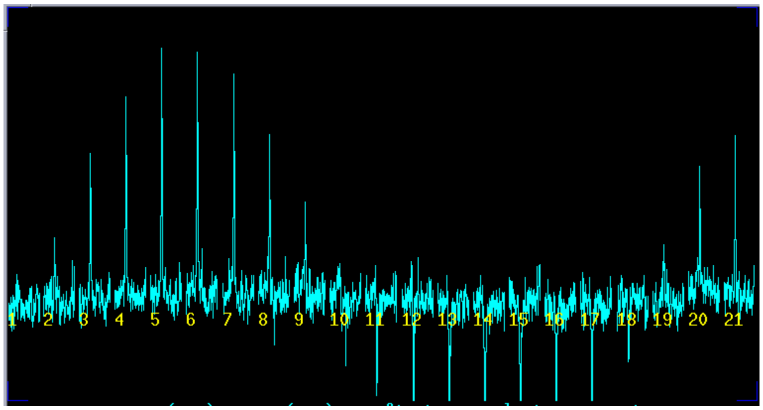

Figure 7.7: Sodium pulse width array to test low frequency channel of double resonance probe. The pulse width is varied from 0 μs to 4 μs in 0.20 μs increments at 52 dB. From this plot, the 90 time is determined to be 1.3 μs

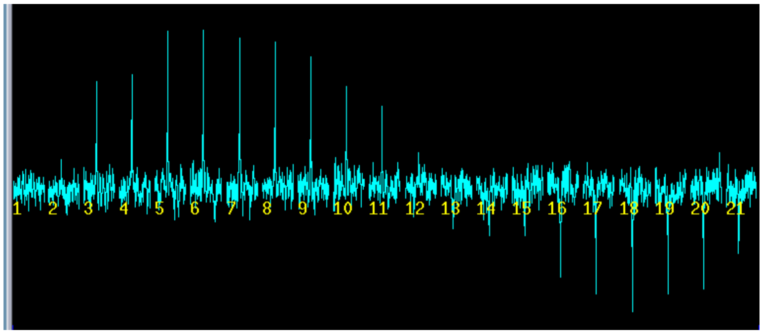

Figure 7.8: Xenon pulse width array on double resonance probe. The pulse width is varied from 0 μs to 3 μs in 0.20 μs increments at 50 dB. From this plot, the 90 time is determined to be 1.0 μs

Given the knowledge that the low frequency channel was working properly, the experiments were performed to locate the aqueous xenon resonance and to determine the 90 time. Hyperpolarized xenon gas was dissolved into water using the homebuilt gas exchange membranes described in section 6.1.2. At that time, 60 psi of a gas mixture containing 2% xenon gas at a polarization of ~6% was dissolved into water flowing at 600 μL/min. Using 1024 scans, a clear nutation curve was observed. The pulse width was arrayed from 0 to 3 μs in 0.20 μs increments at 50 dB (Figure 7.8). The 90 degree time was determined to be 1.0 μs with an SNR of 13.4.

7.2 Remote Detection of Aqueous Xenon through a Microfluidic Chip

In the experiments conducted using the double resonance remote detection probe, two microfluidic chips designed by Elad Harel and fabricated by Dolomite Ltd. for previous proton-based remote detection experiments were used due to their features and availability

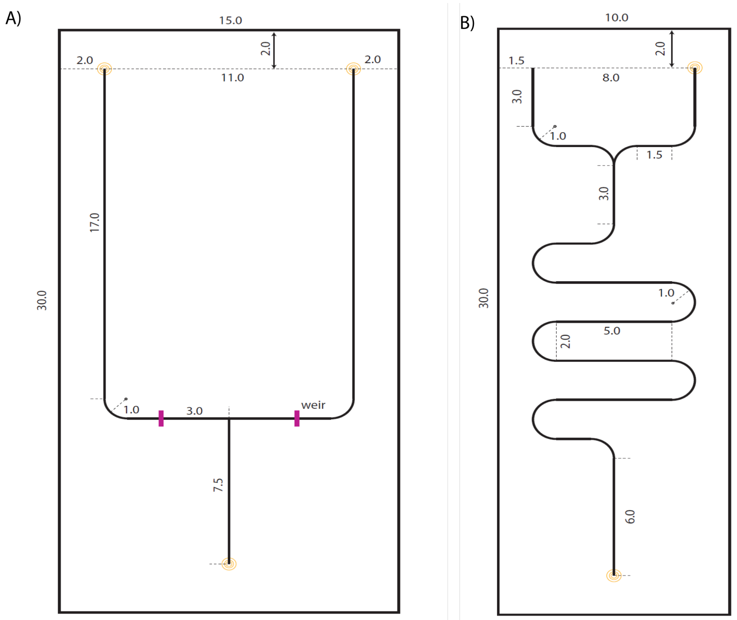

Figure 7.9: Microfluidic chips used in this thesis. The microfluidic chips used in this thesis were originally designed by Elad Harel and fabricated by Dolomite Ltd. All of the units given in the figure are in mm. A) A ‘Y’ shaped chip was used in the xenon-based experiments, where aqueous xenon flowed through one of the inlet ports and out of the outlet. The other inlet port was blocked with an Upchurch plug. B) A serpentine chip was used in the proton-based experiments due to its more complex features. As in (A), water flowed through one of the two inlet ports and out of the outlet, while the other inlet port was blocked with a plug.

(Figure 7.9). The ‘Y’ shaped chip used in the aqueous xenon experiments had dimensions 15 mm x 30 mm x 4 mm while the serpentine chip used in the proton-based experiments was 10 mm x 30 mm x 4 mm. In both chips all channels were semicircular with a radius of 75 μm.

The microfluidic chips were housed in Delrin microfluidic chip holders designed by the author that could be easily attached with 4-40 Teflon screws to the copper hat used to shield the detection probe electronics (Figure 7.10). Upchurch 6-32 flat bottomed connectors compatible with 1mm long Upchurch nanoport adapters were used to secure the PEEK 360 μm inlet and outlet capillary tubing to the ports of the microfluidic chips. Finally, two glass capillary tubes filled with water, flame-sealed over a Bunsen burner, were attached to the face of the microfluidic chip holder such that a traditional gradient echo image in the encoding region could be used to align the microfluidic chip along either the x-z or y-z gradient axis.

7.2.1 Aqueous Xenon Travel Curves through a Microfluidic Chip

The first remotely detected xenon travel curves were acquired by flowing aqueous xenon through the ’Y’ shaped chip given in Figure 7.9A. 65 psi of a 2% xenon gas mixture was delivered to the gas exchange membranes at 0.5 SLM, while pressurized water was set to flow at 550 μL/min. The SNR following 512 averages of a hard pulse in the detection region was ~20. An inversion pulse was applied in the encoding region using a 240 μs pulse at 57 dB on

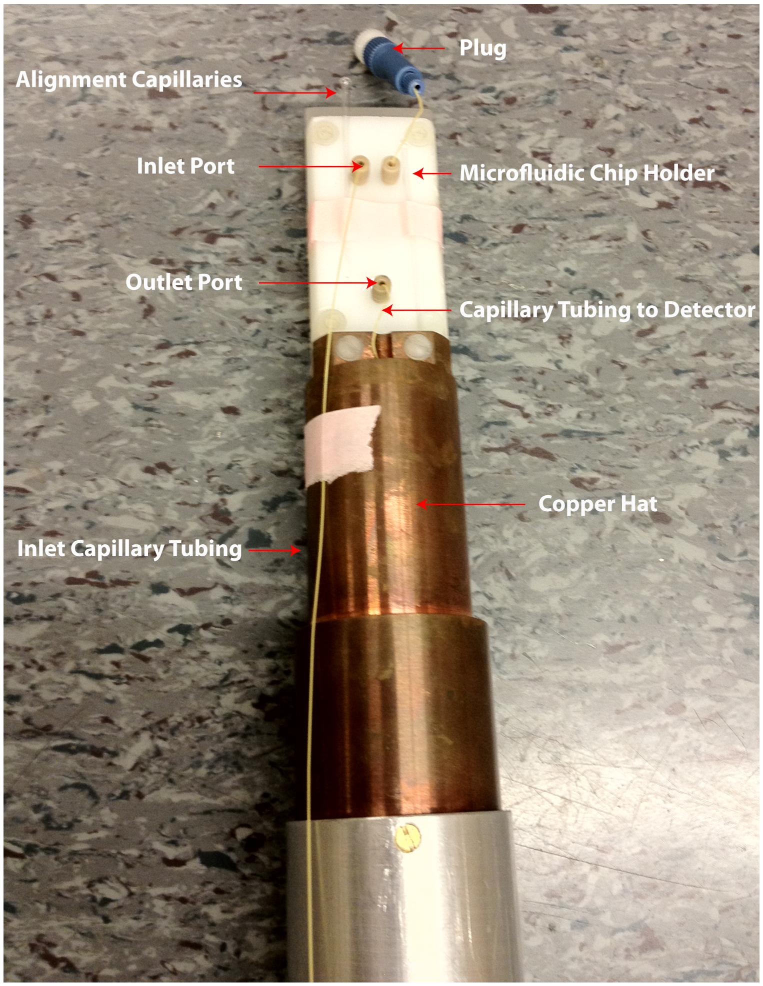

Figure 7.10: Microfluidic Chip Assembly. Microfluidic chips were housed in Delrin holders that matched the dimensions of the chips and could be screwed onto the copper hat used to shield the RF electronics. Upchurch nanoport assemblies were then used to seal the inlet and outlet 360 μm capillary tubing into the ports of the microfluidic chips and water-filled glass capillaries were used to align the microfluidic chips along one of the primary axes in the gradient field.

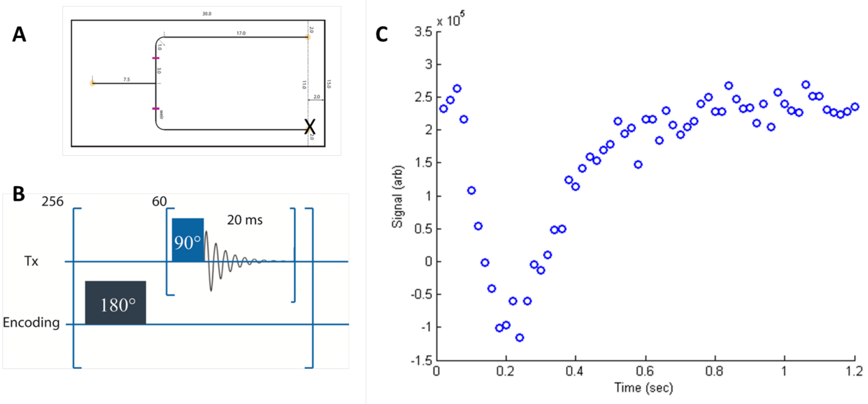

Figure 7.11: Inverted xenon travel curve. A) A schematic of the ’Y’ chip used for this experiment. Water flowed through one of the branches, was blocked from flowing through the second branch, and flowed out of the single stem. B) A schematic of the remote detection pulse sequence. C) Integrated signal intensity for each acquired FID. Full signal intensity is observed for the initial points where xenon did not experience the 180 degree pulse. The signal from 80 ms to 500 ms was manipulated by the inversion pulse.

the xenon external amplifier (Figure 7.11A) such that the initial magnetization due to the hyperpolarized xenon was stored along the -z axis and was only susceptible to T_1 relaxation as the liquid flowed to the detection solenoid coil. After 256 averages, the processed FIDs (Figure 7.11C) show a clear region from 80 - 500 ms where inverted hyperpolarized xenon contributed to the total magnetization. Thus, the total travel time through the microfluidic chip at this water flow rate was approximately 420 ms.

Following the initial travel curve, a four step phase cancellation pulse sequence was applied after which positive signal was generated if and only if spins where within the encoding region (Figure 7.12). This four-pulse phase table was first used by Paulsen, et al. in 2010 in order to simplify data collection in remotely detected imaging pulse sequences [101]. Here, 1024 averages were necessary to collect data with roughly the same signal intensity. As can be seen in Figure 7.13B, positive signal intensity is only generated in the same 420 ms region from 80 - 500 ms.

7.2.2 Extending the Residence Time in the Microfluidic Chip

While a clear region of inversion was observed for aqueous xenon flowing at 550 μL/min (Figures 7.11C and 7.13C), the residence time for aqueous xenon in the microfluidic chip was only ∼420 ms. This amount of time is unlikely to be long enough to observe aqueous xenon signal depletion due to the application of a saturation pulse at the resonance frequency of xenon associating with cryA on a microfluidic chip. A simple way to extend the length of time that signal is observed is to slow the water flow rate and to observe the subsequent inversion of the aqueous xenon resonance. The initial signal intensity is decreased in this type of experiment by T_1 relaxation. At a water flow rate of 190 μL/min, the SNR for the aqueous xenon peak following 1024 averages was ∼15. This is approximately half of the SNR

A)

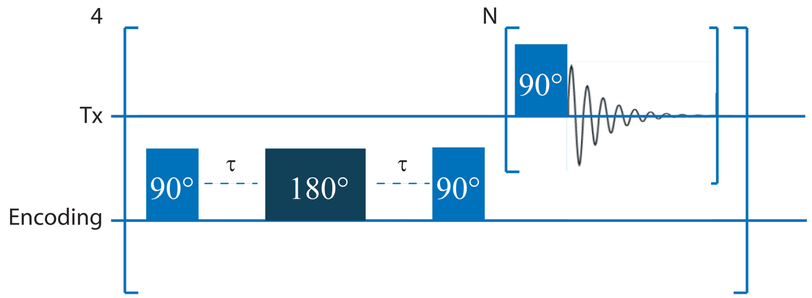

B)

				All 4	Detection
-y	+x	-y	+x	+x	+x
+y	+y	+x	+y	+x	+y
-y	-x	+y	-x	+x	-x
+y	-y	-x	-y	+x	-y
			Total	4x	0

Figure 7.12: Remote Detection Phase Canceling Phase Table. A) Schematic of a pulse sequence used to cancel the signal outside of the encoding region. This pulse sequence was developed by Dr. Vikram Bajaj and a variation on the phase table was first reported in [101]. B) The phase table used in this thesis. As shown in the 'Total' row, signal inductively detected in the x-y plane is only present when spins are perturbed by pulses in the encoding region. The sum pulses in the detection region alone cancel the initial magnetization.

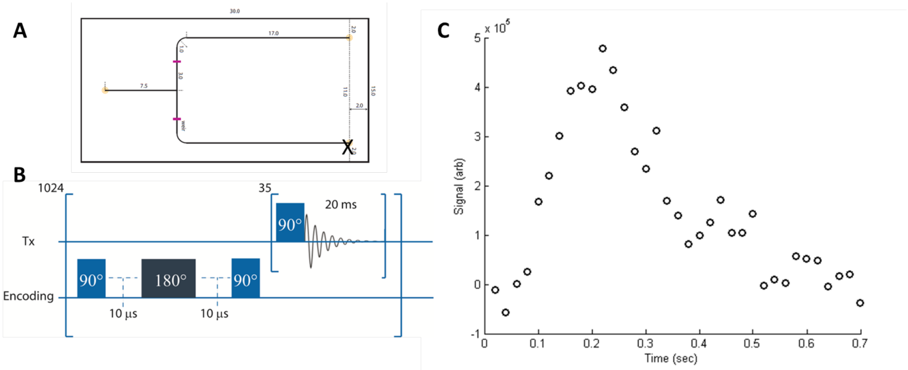

Figure 7.13: Xenon phase cancellation travel curve. A) A schematic of the 'Y' chip used for this experiment. Water flowed through one of the branches, was blocked from flowing through the second branch, and flowed out of the single stem. B) A schematic of the phase cancellation pulse sequence. C) Integrated signal intensity for each acquired FID. Positive signal is only expected in the region where the xenon nuclei experienced all four pulses. This corresponds to the region between 80 and 500 ms.

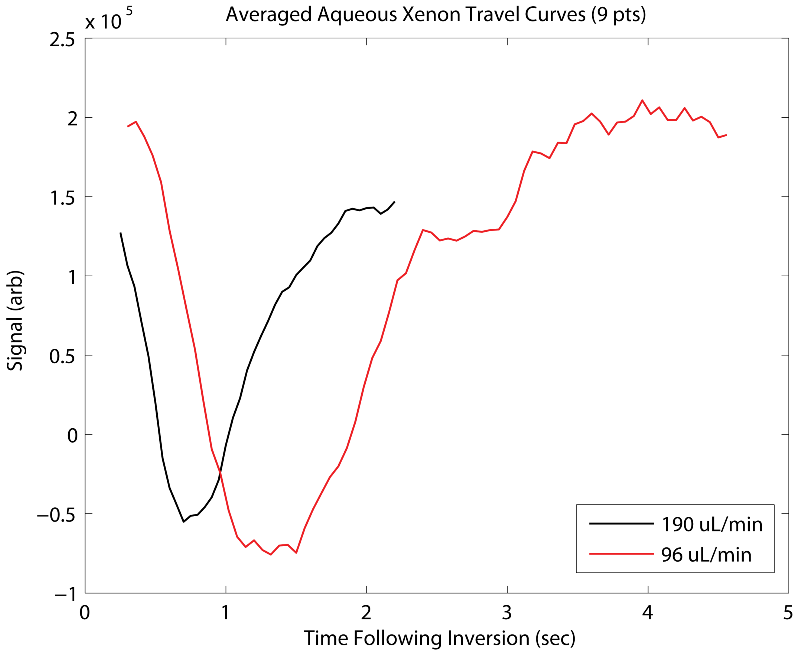

Figure 7.14: Extended Aqueous Xenon Remote Detection Curves. Here, the water flow rate was reduced to 190 μL/min (black) and 96 μL/min (red). Due to the low SNRs at these flow rates, each point in time is the average of nine signal intensities. Under these conditions, the residence time for aqueous xenon within the 'Y' shaped chip was extended to 1.5 and 3 seconds respectively.

for aqueous xenon flowing at 550 μL/min when corrected for the number of scans collected. When the flow of water is slowed further to 96 μL/min, the SNR fell to ∼5 in 1024 averages.

In spite of the decreased SNR, collecting travel curves at these slower flow rates provides a method for extending the residence time for aqueous xenon within the microfluidic chip. Figure 7.14 shows the result of applying a 180 degree pulse in the encoding region followed by stroboscopic detection with the detection probe in 256 averages at 190 μL/min and 512 averages at 96 μL/min. Due to the low SNR, each position on the travel curves in Figure 7.14 corresponds to the average of the individual signal at that time point plus or minus four points (nine points in total). By lowering the water flow rates, the residence time for aqueous xenon within the 'Y' shaped chip could be extended from 420 ms at 550 μL/min to ∼1.5 seconds at 190 μL/min and ∼3 seconds at 96 μL/min.

7.2.3 Aqueous Xenon Noise Characterization

As indicated in the previous section, the signal to noise ratio of the aqueous xenon peak decreased substantially at reduced water flow rates. With the constant potential for low signal due to low levels of xenon hyperpolarization or signal loss due to relaxation effects, scan to scan variability should be considered. The consistency of the signal acquired in the detection region was tested for xenon gas (66 psi, 0.45 SLM) dissolved into water flowing at 575 μL/min where the SNR following 1024 scans was 12.4. In this study, 1024 averages of a

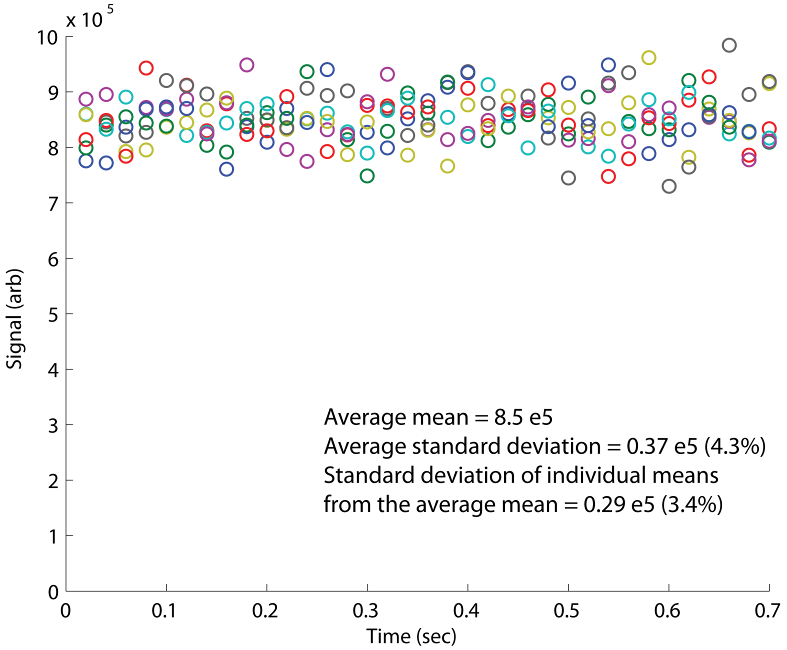

Figure 7.15: The precision and accuracy mock aqueous xenon travel curves were recorded by stroboscopically detecting the signal in the detection region without application of a pulse in the encoding region. This process was repeated six times, where each color represents one run acquired in 1024 scans. Both the accuracy and precision of these measurements are below 5%.

90 degree pulse applied 35 times stroboscopically in the detection region were collected. This process was repeated six times in succession, with the resulting signal intensities plotted in Figure 7.15. Here, excellent accuracy given by the average standard deviation (4.3%) and precision given by the standard deviation of the individual means from the average (3.4%) were observed.

In addition to the accuracy and precision across the same number of scans, the standard deviation from the mean was recorded for an increasing number of scans (Figure 7.16). As the number of averages increases (nt = 512, 1024, 4096, 12288), the standard deviation from the mean decreases from 5.5% for 512 averages to 1.0% for 12288 scans. Therefore, the number of scans performed in a study can be tailored to yield contrast between two states under varying thresholds for noise.

7.3 Proton-based Imaging and Spectroscopy using the Double Resonance Remote Detection Probe

7.3.1 Proton Travel Curve

Following acquisition of remotely detected aqueous xenon travel curves through a microfluidic chip, the proton channel was tested for its spectroscopic and imaging capabilities.

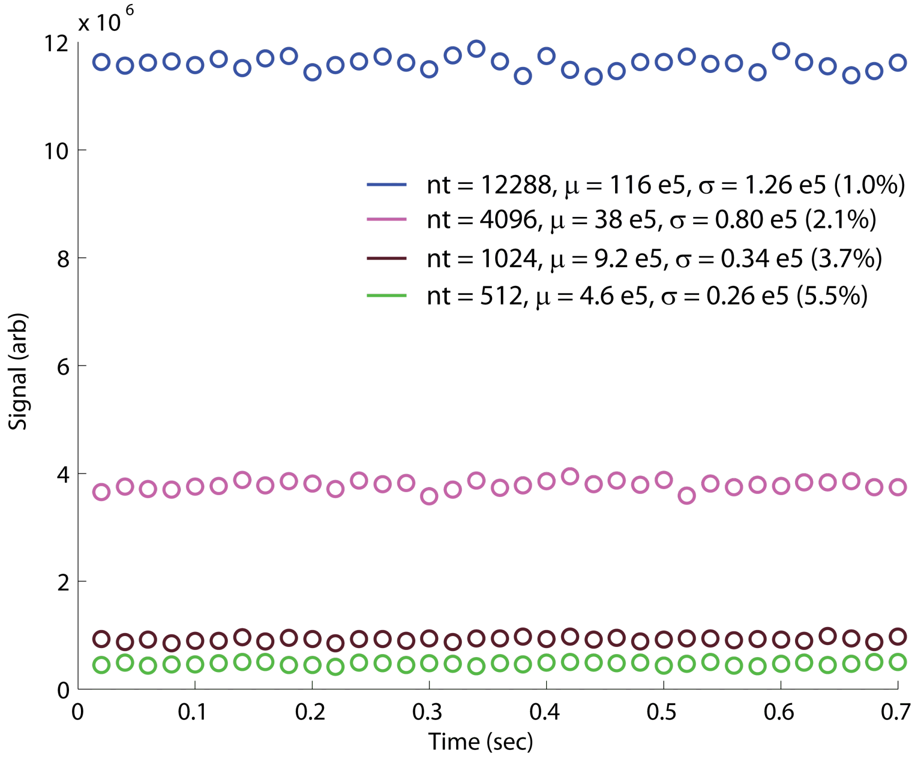

Figure 7.16: The consistency of aqueous xenon travel curves was tested by evaluating the standard deviation from the mean following stroboscopic detection in the detection region alone. Here, the standard deviation was observed to decrease as the number of averages was increased.

As in the single resonance remote detection scheme, the first step was to calibrate an external amplifier to match the power settings for the internal amplifier on the high frequency channel. Using the same protocol detailed in Chapter 6, a 46 dB pulse on the high frequency external amplifier was determined to match the power output of a 52 dB pulse using the internal amplifier.

The phase cancellation remote detection scheme described above was used to calibrate the 90 and 180 times for the proton channel on the 30 mm probe as water flowed through the 'Y' shaped chip used in the aqueous xenon experiments. Here, the three pulses (90 - 180 - 90) in the encoding region were assumed to be linear and co-varied such that the 90 degree pulses were incremented in 20 μs increments and the 180 degree pulse was simultaneously incremented by 40 μs. The maximum positive signal intensity occurred using an 80 μs 90 degree pulse and 160 μs 180 degree pulse at 46 dB with the external amplifier. Figure 7.17 shows the result of applying a single phase cancellation pulse sequence (4 scans total) to water flowing at 390 μL/min through the 'Y' shaped chip. When each FID is transformed, the area under the curves was integrated and the signal intensity was plotted as a function of time from the beginning of stroboscopic detection (Figure 7.17C). Here, water arrived in the detection region 180 ms following the conclusion of the encoding pulses with a total residence time of 620 ms.

7.3.2 Proton Image

Once the 90 and 180 degree pulses were calibrated and the initial phase canceled water proton travel curve was collected a proton image could be acquired. For this experiment, two glass capillaries were filled with water and flame sealed such that they could be inverted without fear of losing the sample. The capillaries were taped onto the flat face of the microfluidic chip holder in order to be used as an alignment mechanism. After locating the primary resonance frequency offset with a hard pulse in the encoding region, a traditional gradient echo pulse sequence was used to orient the face of the microfluidic chip, and thus the chip itself, with the x-z axis.

Following chip alignment, the approximate x and z gradient strengths were calculated using the formula [97]:

$$FOV_{x,z} = \frac{1}{\gamma G_{x,z} t} \tag{7.6}$$

where $FOV_{x,z}$ is the image field-of-view in the x or z dimension, $G_{x,z}$ is the maximum applied gradient strength, and t is the length of time for the gradient pulse. For this experiment, the gradients were chosen to be applied for a constant time t = 500 μs. Then, for FOV_x = 1.2 cm and FOV_z=2.5 cm, the gradient strengths were calculated to be G_x = 6.2 G/cm and G_z = 3.0 G/cm. The calibrated maximum gradient strengths for the gradient stack used in the system are $G_{x,max}$ = 79.2 G/cm and $G_{z,max}$ = 58.1 G/cm. Knowing these values and that the maximum DAQ value is 32767, the maximum applied gradient strengths were estimated

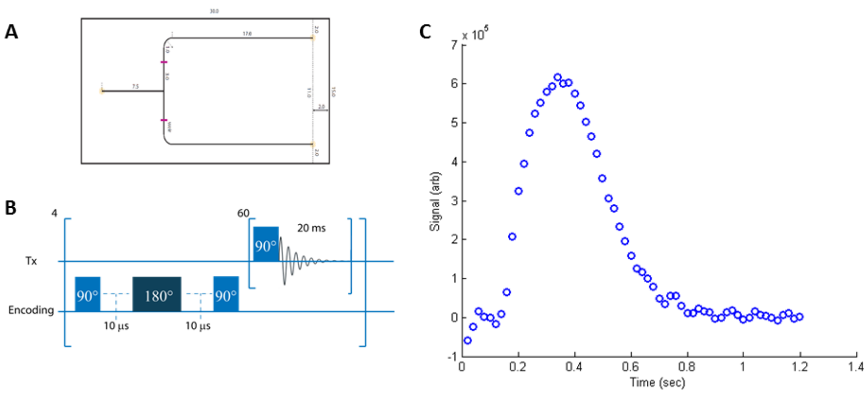

Figure 7.17: Proton phase cancellation travel curve. A) A schematic of the ’Y’ chip used for this experiment. Water flowed through one of the branches, was blocked from flowing through the second branch, and flowed out of the single stem. B) A schematic of the phase cancellation pulse sequence. C) Integrated signal intensity for each acquired FID. Positive signal is only expected in the region where the water protons experienced all four pulses. This corresponds to the region between 180 and 800 ms.

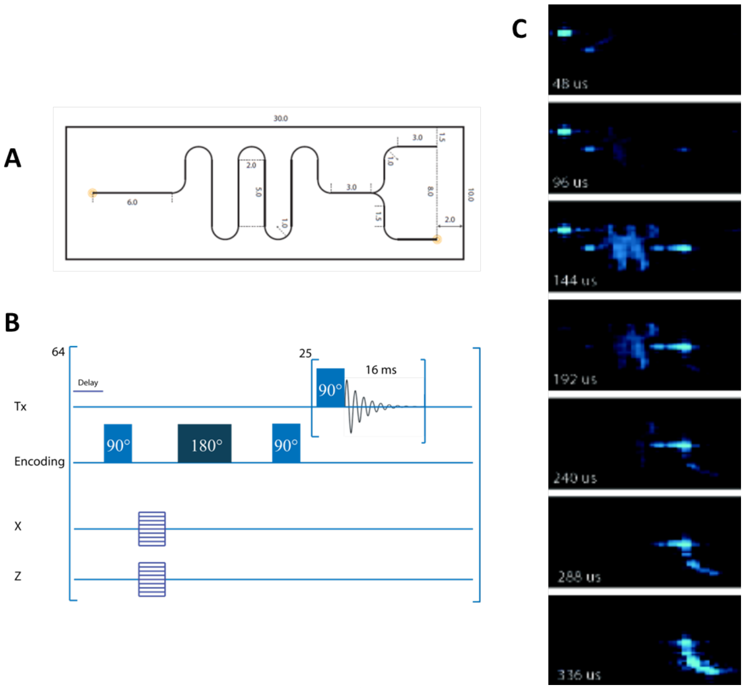

Figure 7.18: Time of flight proton image. A) A schematic of the serpentine chip used for this experiment. B) The remote detection pulse sequence. C) Time of flight images for water flowing from the encoding region to the detector. The first time points correspond to water near the outlet of the chip. The water flowing logically through the chip can be traced backwards in time.

to be $G_x = 2565$ and $G_z = 1692$ DAQ units.

A two-dimensional image was acquired of water flowing at 400 μL/min through a serpentine chip. Here, 21 x 21 phase encoding steps were applied following the initial 90 degree pulse in the encoding region (Figure 7.18A), where the z-gradient was incremented from -1000 to 1000 DAQ units in 100 unit steps and the x-gradient was incremented from -2000 to 2000 in 200 unit steps. The resulting image is displayed in Figure 7.18B. From top to bottom are the images for water detected in 16 ms increments from the conclusion of the encoding pulse sequences. This sequence captures the reverse progression of water flowing through the serpentine chip. As an aid to the eye, it is easier to follow the progression of water from the late time points (bottom) to the early time points (top). In this manner, the flow of liquid through the chip is clearly visible.

7.4 Discussion and Future Directions

This chapter presented the design and fabrication of a double resonance probe for detecting both aqueous xenon and water protons flowing through microfluidic chips remotely. The remotely detected aqueous xenon signal was fully characterized and an example of a water proton travel curve and image were presented for fluid flow through commercial microfluidic chips. These experiments suggest that detection of a sensor on a chip will be possible.

In addition to the hardware required for this experiment, a sensor was selected for the initial remote detection experiments on a microfluidic chip. This sensor was a 20-mer of single-stranded DNA (5' - TCA TAC GAC TCA CTC TAG GG -3') with a six carbon chain linking a primary amine to the 5' end. This sequence was used heavily in the Matt Francis lab at UC Berkeley at the time this thesis was written. Gary Tong, a graduate student in the Francis lab attached monoacid cryA to the 20-mer for use in this study. The vision for this construct was to attach the complementary strand of DNA to the surface of a microfluidic chip via relatively standard surface chemistry and to subsequently attach the sensor to the chip through hybridization.

For a chip with a well that had dimensions 2 mm x 8 mm x 20 μm with a realistic surface density of $10^{11}/\text{cm}^2$ (personal communication with Sonny Hsiao, formerly of the Matt Francis group), the effective concentration of the sensor would be $\sim$166 nM. Work is actively being done by Dan Kennedy of the Pines Lab to develop single and double well glass chips that can be tailored to this type of experiment. In order for this experiment to be viable, the polarization of the MITI hyperpolarizer must be restored to its previous 6% polarization or better. Experiments with DNA sensors could not be completed because the polarizer has been inoperative for the past 8 months.

7.5 Acknowledgements

The work presented in this Chapter was conducted with support and assistance from Hattie Ring, to whom I would like to give thanks.

Chapter 8

Paramagnetic Relaxation Agents for Xenon-based Applications

The development of xenon-based molecular sensors has expanded the realm of contrast agents for magnetic resonance imaging. With more academic research and a helping hand from industry, these sensors could find a niche in clinical applications such as lung cancer diagnostics and biological and chemical assays where it is either undesirable or not possible to purify samples for optical detection. Exploring the possibility for novel xenon contrast agents is an exciting space, especially when paired with talented synthetic collaborators such as those in the Francis Lab at UC Berkeley.

One class of sensors not previously explored is the combination of traditional xenon biosensors and a paramagnetic contrast agent. Depending on the metal ion chosen, these novel sensors could act as enhanced chemical shift agents similar to the PARACEST agents detailed in Chapter 2 or as T_1 relaxation agents. Preliminary simulations suggest that the pseudo-contact chemical shift induced by lanthanides such as terbium and dysprosium would induce a chemical shift of the caged xenon resonance frequency, but that in no case would the shift be more than 10 ppm at the realistic 15 angstrom xenon to lanthanide center-to-center distance in isotropic solutions. For this reason, modifications of cryptophane-A with the intention of generating a T_1 relaxation agent were explored. This chapter expands on the theory of T_1 relaxation agents originally presented in Chapter 2. Furthermore, the simulations used to assess the potential utility for these sensors are detailed and the early experimental results are presented.

8.1 T_1 Relaxation Theory

MR relaxation theory was initially studied in great detail by Redfield in the 1950s [108] and Abragam in the 1960s [3]. Since that time, T_1 relaxation theory for water protons in the presence of paramagnetic ions was studied extensively beginning with the work of Solomon and Bloembergen ([121], [122], [19]). Such work has been reviewed by many authors ([20], [76],[48], [106]), from which additional details can be found.

In an NMR experiment, the time constant T_1 is the sum of an inherent diamagnetic component ($T_{1,d}$) and a paramagnetic component ($T_{1,p}$) when such a species exists in solution where the total T_1, $T_{1,obs}$, is given by

$$\frac{1}{T_{1,obs}} = \frac{1}{T_{1,d}} + \frac{1}{T_{1,p}}. \tag{8.1}$$

The paramagnetic component is itself made up of inner sphere effects, $T_{1,inner}$, where water molecules temporarily coordinate with a paramagnetic metal chelate and outer sphere effects, $T_{1,outer}$, where translation past the metal chelate dominates. As above, the contributions to the paramagnetic T_1 relaxation add reciprocally as

$$\frac{1}{T_{1,p}} = \frac{1}{T_{1,inner}} + \frac{1}{T_{1,outer}}. \tag{8.2}$$

8.1.1 Inner Sphere Relaxation

Inner sphere relaxation is the result of one or more water molecules briefly coordinating with a paramagnetic center, where q is the number of molecules coordinated. This number can range from 1 for tightly chelated metals (e.g. Gd^{3+}-DOTA) to 8 or 9 for free metal ions in solution (e.g. Gd^{3+}-aquo ion) [76]. Given a mole fraction of metal ions in a solution, P_M, inner sphere relaxation is defined to be [76]

$$\frac{1}{T_{1,inner}} = \frac{P_M q}{T_{1,M} + \tau_M} \tag{8.3}$$

where τ_M is the lifetime of the bound water molecules and $T_{1,M}$ is the relaxation time constant of the bound water molecules as defined by Solomon and Bloembergen. The relaxation time constant of the bound water molecules is comprised of two components: a dipolar, distance dependent term and a through-bond scalar term [76]

$$\begin{aligned} \frac{1}{T_{1,M}} &= \frac{2}{15}\frac{\gamma_I^2 g^2 S(S+1)\beta^2}{r^6}\left[\frac{7\tau_c}{(1+\omega_S^2\tau_c^2)} + \frac{3\tau_c}{(1+\omega_I^2\tau_c^2)}\right] && (8.4)\\ &+ \frac{2}{3}S(S+1)\left(\frac{A}{\hbar}\right)^2\left[\frac{\tau_e}{(1+\omega_S^2\tau_c^2)}\right] && (8.5)\end{aligned}$$

where γ_I is the gyromagnetic ratio of water in radians/seconds, g is the electronic g-factor, S is the total electron spin, β is the Bohr magneton, r is the center-to-center distance separating the metal ion and the water proton, $\omega_{I,S}$ is the Larmor frequency of the water proton (I) and electron (S) respectively, and $A/\hbar$ is the hyperfine coupling constant between the electron and the nucleus of a water proton. The correlation times τ_c and τ_e are defined by [76]

$$\frac{1}{\tau_c} = \frac{1}{T_{1e}} + \frac{1}{\tau_M} + \frac{1}{\tau_r} \tag{8.6}$$

$$\frac{1}{\tau_e} = \frac{1}{T_{1e}} + \frac{1}{\tau_M} \tag{8.7}$$

Table 8.1: Electronic Spin Relaxation Time Constants

Agent	Spin	Magnetic Field (Range)	Value
Nitroxide	1/2		100 ns [103]
Mangenese(II)	5/2	14.1 T	5.4 ns [104]
Mangenese(II)	5/2	0.47 T	1.5 ns [4]
Gadolinium(III)	7/2		0.1 - 1 ns [76]

where T_{1e} is the electronic spin relaxation time constant and τ_r is the rotational correlation time.

The electronic spin relaxation time constant T$_{1e}$ arises from zero-field splittings induced by collisions between solvent molecules and metal ions with S $>$ 1/2. For symmetric metal ions in solution [76]

$$\frac{1}{T_{1e}} = B\left[\frac{\tau_V}{1+\omega_S^2\tau_V^2} + \frac{4\tau_V}{1+4\omega_S^2\tau_V^2}\right] \tag{8.8}$$

where ω_S is the Larmor frequency for the metal ion in rad/s, B is proportional to the magnitude of the zero-field splitting, and τ_V is the correlation time constant for the fluctuations. For metal complexes with low symmetry, on the other hand, T$_{1e}$ becomes highly complex and magnetic field dependent. Typically, electronic relaxation times are estimated by measuring the linewidth in an electron spin resonance experiment. The T$_1$ electronic relaxation time constants used in this thesis are given in Table 8.1.

8.1.2 Outer Sphere Relaxation

While inner sphere effects describe the relaxation of water molecules that are coordinated to a metal ion, outer sphere effects provide additional T_1 relaxation due to the translation of water molecules past the metal chelates. Bennett, et al. define outer sphere relaxation as [13]

$$\frac{1}{T_{1,outer}} = \left(\frac{32\pi}{405}\right)\gamma_I^2\gamma_S^2\hbar^2 S(S+1)\frac{N_A}{1000}\left(\frac{[M]}{dD}\right)[3j(\omega_I)+7j(\omega_S)] \tag{8.9}$$

where $\gamma_{I,S}$ is the gyromagnetic ratio of the nucleus and electron respectively in radians/second, S is the total electron spin, N_A is Avogadro's number, $[M]$ is the molarity of the metal ions, d is the distance of closest approach for a water molecule to the metal ion, and D is the sum of the diffusion coefficients for the metal chelate and the water molecule. The spectral density function, $j(\omega)$, is based on the work of Freed, et al. [43] and is defined here to be

$$j(\omega) = \mathrm{Re}\left(\frac{1+\frac{1}{4}(\imath\omega\tau_t+\tau_t/T_{1e})^{\frac{1}{2}}}{1+(\imath\omega\tau_t+\tau_t/T_{1e})^{\frac{1}{2}}+\frac{4}{9}(\imath\omega\tau_t+\tau_t/T_{1e})+\frac{1}{9}(\imath\omega\tau_t+\tau_t/T_{1e})^{\frac{3}{2}}}\right) \tag{8.10}$$

where $\tau_t = d^2/D$ is the translational correlation time. For tightly chelated metal ions, outer sphere relaxation dominates the total paramagnetic contribution to T_1 relaxation.

8.2 Novel Contrast Agent Simulations

8.2.1 Testing the Simulation Code against Published Data

The goal of the simulations presented in this thesis was to predict the enhancement in xenon T_1 relaxation by cryptophane-A conjugated to a variety of paramagnetic ions over a range of center-to-center distances. As a result of these simulations, the most suitable agents would be synthesized by the Francis Lab. Three paramagnetic ions were evaluated due to their previous use described in the literature: a spin-1/2 nitroxide molecule, spin-5/2 manganese(II) complexes, and spin-7/2 gadolinium(III) complexes. Before modeling the T_1 relaxation properties of novel xenon-based relaxation agents with these paramagnetic centers, the simulation code was tested for efficacy by inserting parameters from a published experiment and comparing the simulation to the authors' experimental data.

In 2004, Pintacuda, et al. evaluated the effect of copper(II) and manganese(II) as both T_1 and T_2 spin labels for protein structure refinement [104]. In their experiment, the authors bound S-(2-pyridylthio)-cysteaminyl-EDTA to the lone cysteine at residue 78 of the ^{15}N-labeled arginine repressor of *E. coli* via disulfide exchange. $CuCl_2$ and $MnCl_2$ were aded into solution at 10% excess and the uncoordinated metals were removed with Chelex-100 beads. Inner sphere relaxation due to either the copper(II) or manganese(II) spin label was empirically determined by subtracting the measured T_1 relaxation of each amide proton resonance on a Bruker 600 MHz (14.1 T) spectrometer at 25°C from the value of T_1 measured in the same way for the wild-type protein.

Inner sphere T_1 relaxation was modeled and matched to the data from the authors' manganese(II) labeled protein due to the high spin number of manganese (S =5/2) relative to copper (S = 1/2). In this model, the mole fraction of spin label in solution (P_M) and the number of coordinated protons (q) were set to 1 and the exchange of coordinated protons (τ_M) was set to zero. Based on the authors' analysis, an electronic relaxation time constant of 5.4 ns and rotational correlation time of 4.8 ns were used to simulated the T_1 relaxation rate (R_1) over a center-to-center distance over a range of 15 - 35 angstroms with a step size of 0.1 angstroms. The result given in Figure 8.1 shows that the model for inner sphere relaxation of amide protons due to the presence of manganese(II) matched the published data.

8.2.2 Simulation

Knowing that the inner sphere contribution to bulk T_1 relaxation was correctly simulated for amide protons in the presence of a manganese(II) chelate, the remainder of a model for predicting the T_1 relaxation effects for a xenon-lanthanide complex was developed. Two modes for T_1 relaxation were considered: bulk aqueous xenon relaxation with outer sphere effects and the additional contribution of dipolar inner sphere relaxation of xenon within the cryA that is close to the paramagnetic center. Several assumptions went into the model that was ultimately developed. First, the electronic relaxation time constants given in Table 8.1

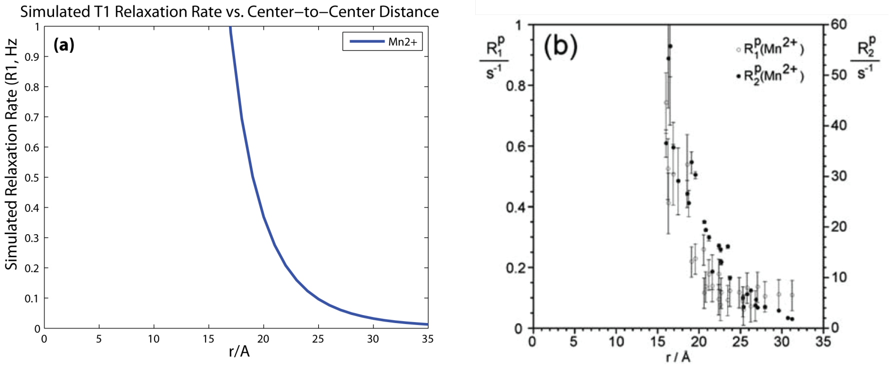

Figure 8.1: Inner Sphere Relaxation: Simulation versus Published Data. A) Simulated T_1 relaxation rates (R_1) versus center-to-center distance for a manganese spin-labeled protein based on the experimental work of Pintacuda, et al. [104]. B) Figure 4B from [104] presented here for a direct comparison of the experimental and simulated values for R_1 over a range of center-to-center distances.

Table 8.2: Simulation parameters based on data referenced in [76], [48], [4], [13], and [99]

	Nitroxide	**Manganese(II)-EDTA**	**Gadolinium(III)-DPTA**
Spin Number	1/2	5/2	7/2
Distance of Closest Approach (nm)	0.25	0.35	0.313
Number Coordinated (q)	2.4	1	1
Diffusion Coefficient (10^9, m^2/s)	1.53	1.3	0.4
Rotational Correlation Time (ps)	16	100	100

were assumed to be correct for all external magnetic fields. Then, the T_1 relaxation time constant for hyperpolarized xenon in water and xenon in cryA were set to 60 seconds and 15 seconds respectively [30]. Furthermore, the exchange time constant τ_M was set to the lifetime of xenon in cryA [30]: 30 ms at 25°C and 6 ms at 37°C. The diffusion coefficient of xenon in water was assumed to be $D = 2.2 * 10^{-9}$ m^2/s [145] and the distance of closest approach for xenon translating past a metal chelate was set to equal the center-to-center distance from the xenon nucleus to the paramagnetic center. Finally, the equilibrium constant for the affinity of xenon with cryA was set to 10,000 M^{-1}.

Additional parameters that were assumed in the model, but varied according to the paramagnetic center are given in Table 8.2. Using these input parameters, the variables considered for optimization in this simulation include the system temperature (T), external magnetic field (B_0), center-to-center distance (r), over-pressure of 2% natural abundance ^{129}Xe gas, concentration of the paramagnetic agent, and the wait time before taking a measurement.

In order to assess the bulk T_1 relaxation of aqueous xenon in the presence of a paramagnetic agent, the concentration of xenon in water, $[Xe]_w$, was first calculated using Equation 3.2. The mole fraction of bound xenon was then determined using

$$PM = \frac{[\text{Agent}]q}{[Xe]_w + [H_2O]} \tag{8.11}$$

where [Agent] is the concentration of the contrast agent in solution and q is given in Table 8.2. The bulk T_1 relaxation ($\text{T}_{1,w}$) was then determined using Equations 8.1, 8.2, 8.3, 8.4, and 8.9.

Next, the additional T_1 relaxation due to inner sphere dipolar effects for xenon within cryA at a center-to-center distance r from the paramagnetic center ($\text{T}_{1,\text{cryA}}$) was calculated using Equation 8.4. Here, the mole fraction of bound xenon was determined using

$$PM = \frac{[\text{Agent}]\text{Occ}}{[Xe]_w + [H_2O]} \tag{8.12}$$

where the occupancy (Occ) was calculated using Equation 4.17. Once both $\text{T}_{1,w}$ and $\text{T}_{1,\text{cryA}}$ were calculated, they were sent as new inputs into the 4-state model for magnetization referenced in Chapter 5 (Figure 8.2).

Unlike HyperCEST saturation, in the case of T_1 relaxation the x and y components of magnetization do not contribute to the time progression of signal decay and therefore the solutions to the kinetic equations describing the 4-state model are identically equal to the McConnell-Bloch equations. Using Equation 4.15 to determine k_{ex} for the system at temperature T in degrees Celsius, the forward (k_1) and reverse (k_{-1}) rates of xenon complexing with cryA were solved for using

$$\begin{aligned} k_{-1} &= \frac{k_{ex}}{K[\text{cryA}]_{\text{free}} + 1} && (8.13) \\ k_1 &= K k_{-1} && (8.14) \end{aligned}$$

where $K = 10000\ \text{M}^{-1}$ and $[\text{cryA}]_{\text{free}} = (1 - \text{Occ})*[\text{cryA}]_{\text{total}}$. As detailed by Chavez [30], the solution to the time progression of magnetization of aqueous hyperpolarized xenon using a 4-state kinetic model is given by

$$\begin{aligned} M(t) &= \frac{1}{(2D)} \times ([Xe]_w^p(A+D)e^{\frac{1}{2}(B-D)t} + [Xe]_w^p(-A+D)e^{\frac{1}{2}(B+D)t} \\ &- \frac{2k_{-1}[\text{cryA}]\text{Occ}}{[Xe]_w} e^{\frac{1}{2}(B-D)t} + \frac{2k_{-1}[\text{cryA}]\text{Occ}}{[Xe]_w} e^{\frac{1}{2}(B+D)t}) \end{aligned} \tag{8.15}$$

where $[Xe]_w^p$ is the initial concentration of hyperpolarized xenon in water that is typically normalized to 1, $[Xe]_w$ is the total concentration of xenon in water, [cryA] is the total concentration of cryA is solution, t is the time following delivery of hyperpolarized xenon, and the coefficients A, B, C, and D are equal to

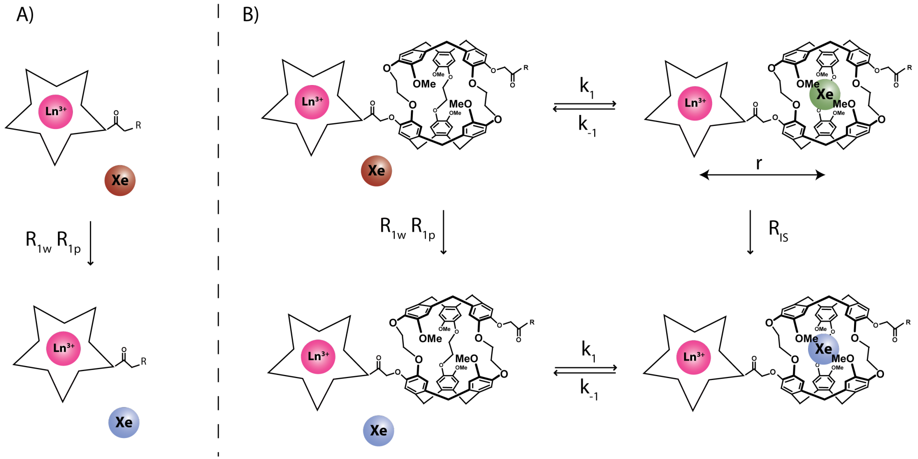

Figure 8.2: Schematic for enhanced xenon T_1 relaxation. A) In the absence of cryA, hyperpolarized xenon will relax to thermal equilibrium due to traditional diamagnetic relaxation (R_{1w}) and bulk paramagnetic effects due to the presence of a paramagnetic ion in solution (R_{1p}). B) In addition to the T_1 relaxation effects described in (A), the dipolar contribution to inner sphere relaxation is added for xenon atoms temporary associated with cryA with a center-to-center distance r to the paramagnetic ion.

$$A = -k_{-1} + [\text{cryA}]_{\text{free}}k_1 - R_{1c} + R_{1w} \tag{8.16}$$

$$B = -k_{-1} - [\text{cryA}]_{\text{free}}k_1 - R_{1c} - R_{1w} \tag{8.17}$$

$$C = [\text{cryA}]_{\text{free}}k_1 R_{1c} + k_{-1}R_{1w} + R_{1c}R_{1w} \tag{8.18}$$

$$D = \sqrt{B^2 - 4C} \tag{8.19}$$

when the saturation pulse applied in a HyperCEST experiment is set equal to zero. The signal decay due to T_1 relaxation following dissolution of hyperpolarized xenon can then be compared for aqueous xenon T_1 relaxation due to outer sphere effects of the paramagnetic chelate versus this bulk T_1 relaxation plus the additional inner sphere dipolar contribution of xenon temporarily bound to cryA close to the paramagnetic center (Figure 8.2). It is expected that the signal depletion will be enhanced at progressively longer wait periods following dissolution of the hyperpolarized xenon.

8.2.3 Simulation Results

For the following simulations contrast was defined as

$$\text{contrast} = \frac{M(\text{wait})_w - M(\text{wait})_{\text{Agent}}}{M(\text{wait})_w} \tag{8.20}$$

where $M(\text{wait})$ is the predicted magnetization at time = wait following dissolution of hyperpolarized xenon normalized to the signal at wait = 0. The background signal depletion $M(\text{wait})_w$ is the expected signal due to outer sphere T_1 relaxation of aqueous xenon in the presence of a chelated paramagnetic ion at wait seconds following dissolution of xenon. As

Table 8.3: Paramagnetic Center Comparison. Simulated contrast (ΔM) for novel xenon-based contrast agents at a constant magnetic field (7.05 T), temperature (298 K), xenon pressure (65 psi), center-to-center distance (10 $\mathring{A}$), agent concentration (20 μM), and wait time (10 seconds).

Paramagnetic Center	$\mathbf{T_{1e}}$ **(ns)**	$\mathbf{R_{1,M}}$ **(Hz)**	$\mathbf{R_{IS}}$ **(Hz)**	**ΔM (%)**
Nitroxide	100	0.09	$3.7*10^{-3}$	2.7
Mn	5.4	6.5	$2.2*10^{-1}$	11
Gd	0.1	5.94	$2.1*10^{-1}$	10
Gd	0.001	0.23	$9.2*10^{-1}$	2.9

described above, the signal depletion for the full cryA construct $M(\text{wait})_{\text{Agent}}$ contains the same background relaxation effects plus the additional dipolar inner sphere relaxation accessible to xenon temporarily bound to cryA.

This simulation, developed to guide synthetic design of novel xenon-based molecular sensors as T_1 contrast agents, was first used to assess the potential change in magnetization under constant conditions as a function of the paramagnetic center (Table 8.3). In this simulation, 20 μM of a paramagnetic cryptophane agent was evaluated at 7.05 T, 298 K, and 65 psi xenon with a center-to-center distance of 10 $\mathring{A}$. The predicted difference in magnetization 10 seconds after the delivery of hyperpolarized xenon to a sample containing the paramagnetic cryptophane agent versus background relaxation in the presence of a paramagnetic center is 2.7% for a nitroxide agent, 11% for a manganese(II) agent, 10% for a gadolinium(III) agent assuming $T_{1e} = 100$ ps, and 2.9% for a gadolinium(III) agent assuming $T_{1e} = 1$ ps. Therefore, if a 5% noise threshold is assumed for the system, manganese(II) or gadolinium(III) agents assuming $T_{1e} = 100$ ps could result in a detectable change in magnetization without the external pulses at the cryA resonance frequency required by a Hyper-CEST pulse sequence under these conditions.

For water equilibrated with a 2% xenon gas mixture at 65 psi, the concentration of xenon in water is ~475 μM. As the concentration of agent increases from 20 μM to 100 μM, the mole fraction of bound xenon increases, which is reflected in an increase in R_{IS} (Table 8.4). The resulting increase in inner sphere dipolar relaxation is predicted to increase the contrast for both manganese(II) and gadolinium(III) agents. Unfortunately, dilution reduces the effect, and for 20 nM concentrations of the agents, the predicted contrast is negligible.

Similarly, decreasing the over-pressure of xenon gas supplied to the system decreases the concentration of the gas dissolved in water, thereby increasing the ratio of paramagnetic cryA to xenon gas. The increased ratio of paramagnetic cryA to xenon results in an increase in MR contrast (Table 8.5). As shown in Table 8.6, increasing the system temperature leads to an increase in the contrast generated with the paramagnetic cryA agents. This is due to the increased exchange of xenon with cryA at elevated temperatures. Furthermore, due to the magnetic field dependence of T_{1e}, moving from an assay at high magnetic fields to low fields such as detection in the Earth's field is also predicted to increase contrast (Table 8.7).

Table 8.4: Concentration Dependence. Novel contrast agent simulated results for constant magnetic field (7.05 T), temperature (298 K), xenon pressure (65 psi), center-to-center distance (10 $\mathring{A}$), and wait time (10 seconds).

Paramagnetic Center	**T_{1e} (ns)**	**Concentration of Agent**	**R_{IS} (Hz)**	**ΔM** (%)
Mn	5.4	250 μM	2.8	100
Mn	5.4	100 μM	1.1	85
Mn	5.4	20 μM	$2.2*10^{-1}$	11
Mn	5.4	20 nM	$2.2*10^{-4}$	$2.7*10^{-3}$
Gd	0.1	250 μM	2.6	100
Gd	0.1	100 μM	1.0	83
Gd	0.1	20 μM	$2.1*10^{-1}$	10
Gd	0.1	20 nM	$2.1*10^{-4}$	$2.7*10^{-3}$

In addition to system parameters, the wait time inserted into the pulse sequence can be adjusted to result in higher contrast. This time period can be made as short as the time required to allow the xenon gas bubbles to settle with an upper bound dictated by T_1 relaxation. As shown in Figure 8.3, for 20 μM of a paramagnetic cryA agent at 65 psi xenon, 298 K, and 7.05 T, more MR contrast is achieved as the length of the wait period is extended. For both the manganese(II) and gadolinium(III) constructs at a center-to-center distance of 10 $\mathring{A}$, the wait period should be greater than ~5 seconds for contrast greater than 5%.

Knowing that increasing the wait time following the dissolution of xenon has the potential to increase the contrast generated with these agents, extending the center-to-center distance for model constructs becomes possible. Table 8.8 gives the results of the simulation when considering 10 and 15 $\mathring{A}$ center-to-center distances for 20 μM of the agent at 298 K, 7.05 T following a 20 second wait. Due to the $1/r^6$ dependence on distance, contrast is decreased at increased distances, but with a long enough wait period, it could be possible to reproducibly detect MR contrast with an extended agent.

Finally, the rotational correlation time could be increased by binding the agent to a bulky molecule such as a protein in solution. If, for instance, the rotational correlation time was on the order of 10 ns rather than 0.1 ns, the contrast generated for a paramagnetic cryA agent versus background T_1 relaxation is predicted to increase dramatically (Table 8.9). For 20 μM of an agent at 65 psi xenon, 298 K, 7.05 T, the increase in contrast for a manganese(II) agent is predicted to be 2.6x and 1.5x for a gadolinium(III) agent.

Table 8.5: Pressure Effects. Novel contrast agent simulated results for constant magnetic field (7.05 T), temperature (298 K), center-to-center distance (10 $\mathring{A}$), concentration (20 μM), and wait time (10 seconds).

Paramagnetic Center	**T$_{1e}$ (ns)**	**Pressure (psi)**	**R$_{IS}$ (Hz)**	**ΔM (%)**
Mn	5.4	65	$2.2*10^{-1}$	11
Mn	5.4	45	$2.9*10^{-1}$	17
Gd	0.1	65	$2.1*10^{-1}$	10
Gd	0.1	45	$2.7*10^{-1}$	16

Table 8.6: Temperature Effects. Novel contrast agent simulated results for constant magnetic field (7.05 T), xenon pressure (65 psi), center-to-center distance (10 $\mathring{A}$), concentration (20 μM), and wait time (10 seconds).

Paramagnetic Center	**T$_{1e}$ (ns)**	**Temperature (K)**	**R$_{IS}$ (Hz)**	**ΔM (%)**
Mn	5.4	298	$2.2*10^{-1}$	11
Mn	5.4	310	$3.2*10^{-1}$	17
Gd	0.1	298	$2.1*10^{-1}$	10
Gd	0.1	310	$2.9*10^{-1}$	16

Table 8.7: Magnetic Field Effects. Novel contrast agent simulated results for constant temperature (298 K), xenon pressure (65 psi), center-to-center distance (10 $\mathring{A}$), concentration (20 μM), and wait time (10 seconds).

Paramagnetic Center	**T$_{1e}$ (ns)**	**Magnetic Field (T)**	**R$_{IS}$ (Hz)**	**ΔM (%)**
Mn	5.4	7.05	$2.2*10^{-1}$	11
Mn	1.5	$0.5*10^{-4}$	$5.2*10^{-1}$	20

Table 8.8: Center-to-Center Distance. Novel contrast agent simulated results for constant magnetic field (7.05 T), temperature (298 K), xenon pressure (65 psi), concentration (20 μM), and wait time (20 seconds).

Paramagnetic Center	**T$_{1e}$ (ns)**	**Distance ($\mathring{A}$)**	**R$_{IS}$ (Hz)**	**ΔM (%)**
Mn	5.4	10	$2.2*10^{-1}$	20
Mn	5.4	15	$3.0*10^{-2}$	6.8
Gd	0.1	10	$2.1*10^{-1}$	19
Gd	0.1	15	$2.0*10^{-2}$	6.6

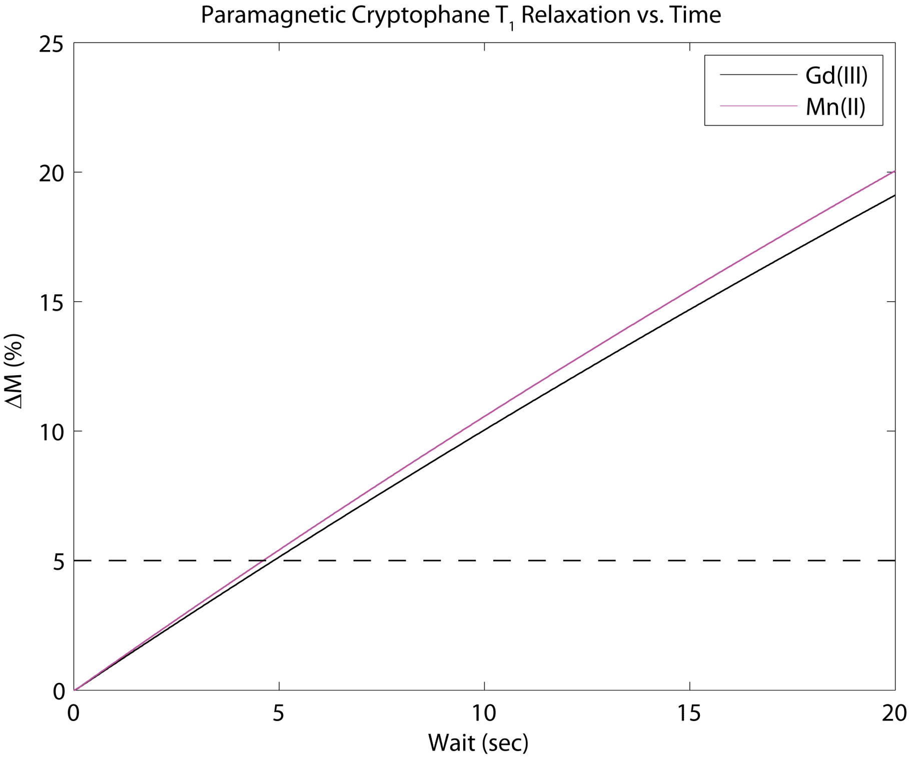

Figure 8.3: Percent Change versus Wait Time. Novel contrast agent simulated results for constant magnetic field (7.05 T), temperature (298 K), xenon pressure (65 psi), concentration (20 μM), and center-to-center distance (10 $\mathring{A}$). The wait time between delivery of hyperpolarized xenon and data acquisition was varied from 0 to 20 seconds for manganese(II) (pink) and gadolinium(III) (black). The dotted line represents the level for a 5% noise cut-off.

Table 8.9: Rotational Correlation Time. Novel contrast agent simulated results for constant magnetic field (7.05 T), temperature (298 K), xenon pressure (65 psi), center-to-center distance (10 $\mathring{A}$), concentration (20 μM), and wait time (10 seconds).

Paramagnetic Center	**T$_{1e}$ (ns)**	**Rotational Correlation Time (ns)**	**R$_{IS}$ (Hz)**	**ΔM (%)**
Mn	5.4	0.1	$2.2*10^{-1}$	11
Mn	5.4	10	$8.4*10^{-1}$	29
Gd	0.1	0.1	$2.1*10^{-1}$	10
Gd	0.1	10	$3.5*10^{-1}$	15

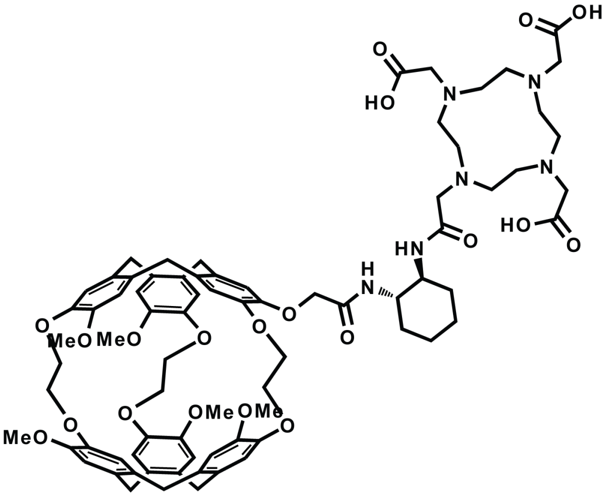

Figure 8.4: CryA-DOTA Schematic.

8.3 Experimental Data

Given the knowledge that the center-to-center distance scales the dipolar inner sphere T_1 relaxation as $1/r^6$, a paramagnetic cryA agent was developed and synthesized by collaborators in the Francis Lab at UC Berkeley that minimized this distance. 1,4,7,10-tetraazacyclododecane-1,4,7,10-tetraacetic acid (DOTA) was attached to cryA via a six carbon ring structure (Figure 8.4). This MR contrast agent (cryA-DOTA) has a center-to-center distance of 11 $\mathring{A}$ between xenon in the center of cryA and either Mn(II) or Gd(III) chelated by DOTA. The simulated contrast for Mn(II) and Gd(III) chelated versions of the cryA-DOTA construct was expected to be sufficient to measure reliably ($> 5\%$) following 4.6 second wait for 20 μM of a Mn(II) construct or 6.9 second wait for the same concentration of a Gd(III) construct at 65 psi xenon, 298 K, and 7.05 T (Figure 8.5).

The initial experiments were conducted at 9.4 T with a xenon overpressure at 15 - 20 psi. Furthermore, due to the potential for spontaneous oxidation of Mn(II) to Mn(III), Gd(III) chelates were chosen for initial testing. Under these conditions, a 20 μM concentration of the Gd(III) cryA-DOTA construct was expected to generate over 5% contrast in ~2 seconds (Figure 8.6). Furthermore, 250 μM of a Gd(III) construct in solution was expected to generate 80% contrast in ~1 second.

For all of the planned cryA-DOTA experiments, a 10mM HEPES buffer at pH 7 was to be used with 10% ACN to improve the solubility of cryA-DOTA in solution. T_1 relaxation time constants for solutions of 250 μM Gd(III)-DOTA, 250 μM Gd(III)-cryA-DOTA, and the buffer at 298 K, 9.4 T were determined using an inversion recovery pulse sequence where 15 - 20 psi of a 2% xenon gas mixture with a natural abundance of xenon-129 was bubbled into solution followed by a wait period, a 180 degree pulse, variable delay period, and a 90 degree pulse for acquisition. The buffer solution was expected to have a long T_1 time constant, therefore the delay time prior to acquisition was arrayed from 0 to 180 seconds in 9 second increments. Xenon was bubbled into solution for 10 seconds, followed by a 1 second

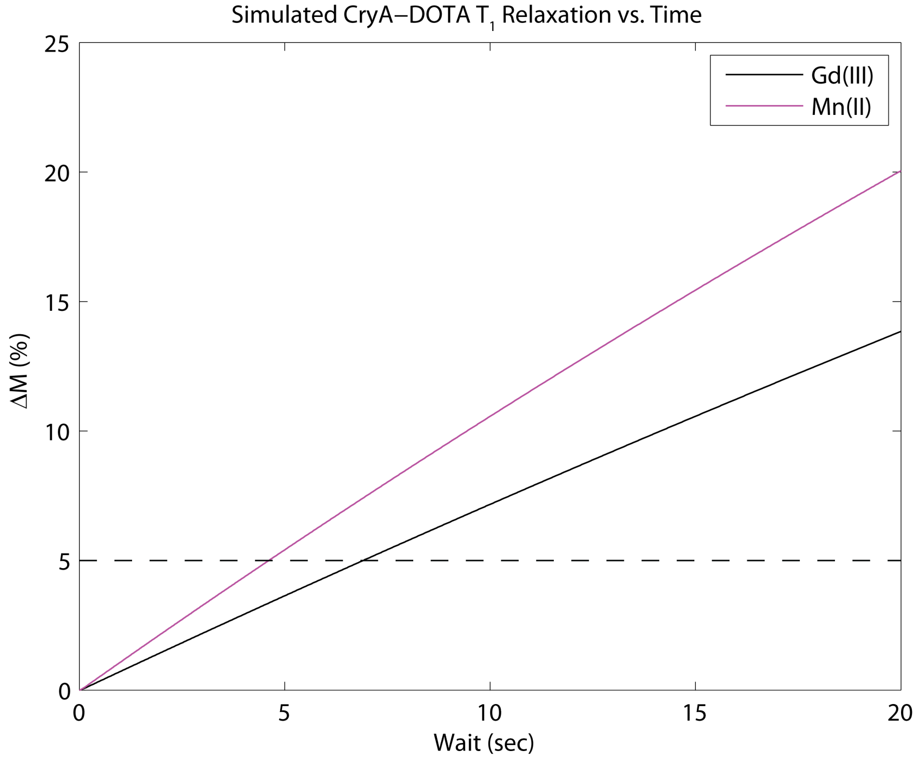

Figure 8.5: CryA-DOTA Simulated Contrast. Simulated contrast for 20 μM cryA-DOTA doped with $GdCl_3$ and $MnCl_2$ at 65 psi xenon, 298 K, and 7.05 T. Contrast is expected to exceed a 5% threshold ∼5 seconds for the Mn(II) construct and ∼7 seconds for the Gd(III) construct.

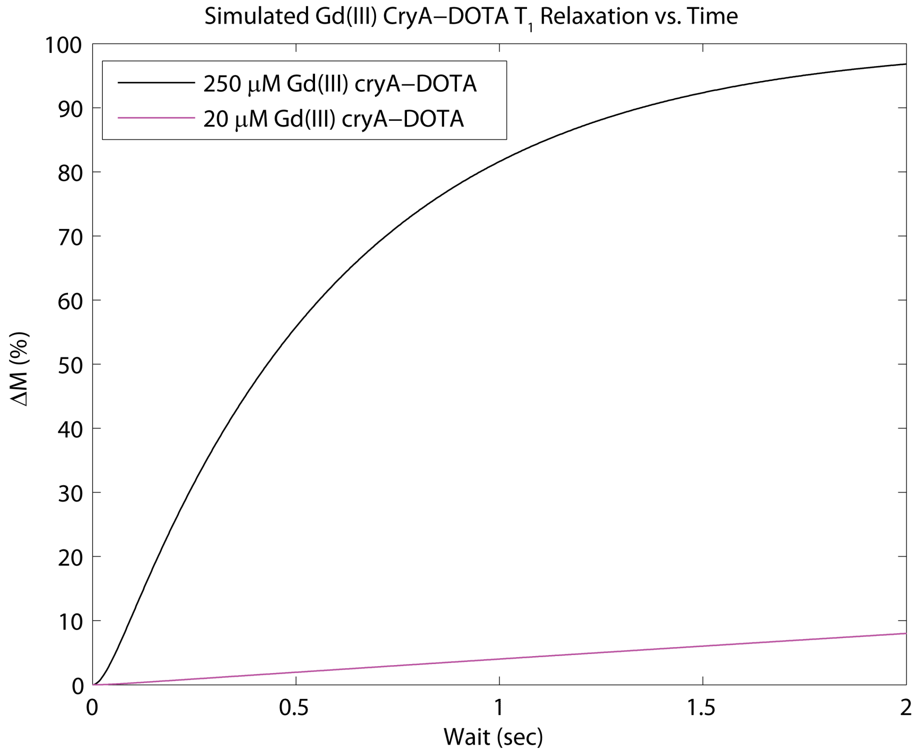

Figure 8.6: Gd(III) CryA-DOTA Simulated Contrast. Simulated contrast for 20 μM cryA-DOTA and 250 μM cryA-DOTA doped with an equivalent of $GdCl_3$ at 20 psi xenon, 298 K, and 9.4 T.

wait before application of the pulses. The processed data was then fit to an exponential of the form

$$M(t) = -Ae^{-t/T_{1,fit}} + O \tag{8.21}$$

where A, O, and $T_{1,fit}$ were fit parameters sent to a non-linear least squares fitting program in Matlab®. The T_1 relaxation time constant for xenon in the buffer was determined to be 54 seconds - within the range of values expected for water (45-60 seconds) (Figure 8.7A).

Analogous experiments were conducted for 250 μM Gd-DOTA and 250 μM Gd-cryA-DOTA in solution. The simulation developed in this thesis suggested that the background T_1 relaxation for 250 μM Gd-DOTA would be near 23 seconds for 20 psi xenon at 298 K, 9.4 T. Therefore, the delay period for the inversion recovery sequence was set to vary from 0 to 72 seconds in 3 second increments following 20 seconds of bubbling and a 1.5 second wait period. In this case, $T_{1,fit} = 26$ seconds, in good agreement with the simulation (Figure 8.7B). The solution with 250 μM Gd-cryA-DOTA was expected to have a much faster T_1 ($\sim$240 ms), but the initial experiment was performed under analogous conditions to 250 μM Gd-DOTA. Xenon was bubbled into solution for 20 seconds followed by a 5 second wait to let the visibly larger bubbles settle with all other acquisition parameters kept constant. Surprisingly, this resulted in a T_1 relaxation time constant of 25 seconds (Figure 8.7C).

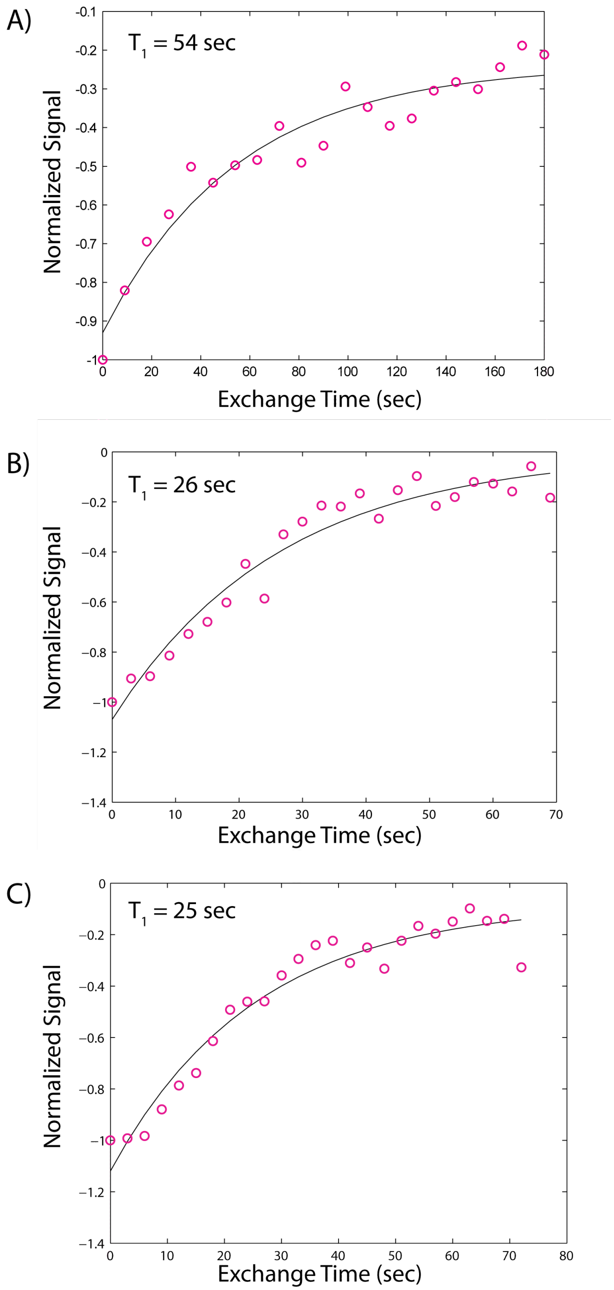

Figure 8.7: T_1 Data. A) An inversion recovery pulse sequence was used to determine the T_1 of 10mM HEPES buffer at pH 7 with 10% ACN added as a co-solvent. An exponential fit to the data gives $T_1 = 54$ seconds, in good agreement with the expected aqueous xenon T_1. B) An inversion recovery pulse sequence was used to determine that the T_1 for xenon in a solution of 250 μM Gd(III)-DOTA was 26 seconds. This is close to the simulated value of 14 seconds under the same conditions. C) The inversion recovery pulse sequence was used to determine that the T_1 for xenon in a solution of 250 μM Gd(III)-cryA-DOTA was 25 seconds. This is much longer than expected and was the first indicator that the construct was not remaining soluble in solution.

Investigations into the reason for this relatively long time constant suggest that xenon is unable to access the cage environment. At an SNR of 34 following a single acquisition of the aqueous xenon peak at 35 psia (∼20 psi), very few averages should be necessary to detect cryA at 250 μM, but no peak was detectable within 64 averages. Follow-up ^{1}H NMR studies suggest that the cryA-DOTA construct is aggregating during the bubbling step. Bubbling xenon into ACN results in visible evaporation in as little as 30 minutes. Thus, it is likely that that the cryA-DOTA construct is precipitating from the solution with the reduction of its organic co-solvent.

8.4 Discussion and Future Directions

While the initial cryA-DOTA construct has yet to be proven as a xenon-based T_1 contrast agent, this class of agents should continue to be pursued due to their potential use in situations where extended pulsing at the cryA resonance frequency is not an option. Experiments are currently on-going to exchange the co-solvent for Gd(III)-cryA-DOTA from ACN to one that is less volatile in order to improve the solubility of the construct in solution with extended bubbling. In the future, a more water soluble version of cryA-DOTA would help improve solubility of the construct in aqueous environments lending easier access of xenon to the cage environment.

Paramagnetic cryptophane-A contrast agents show promise as novel xenon-based molecular sensors, particularly at low magnetic fields. Assuming that the magnetization from a sample can be approximated as a point source, from magnetostatics we know that

$$\mathbf{B}_{dipole} = \frac{\mu_0 m}{4\pi d^3}(2\cos(\theta)\hat{d} + \sin(\theta)\hat{\theta}) \tag{8.22}$$

where μ_0 is the permeability of free space, $m = M/V$ is the magnetic moment, d is the distance from the dipole to the detector, and θ is the angle between the two. Using Equations 2.5 and 8.22, for a sphere of hyperpolarized xenon with radius 2.5 mm, 4 mm from a detector, with 1% polarization using 60 psi xenon at 298 K, the expected magnetic field along the axis of the detector is 1.7 pT. Atomic magnetometers currently functioning in the Pines Lab are capable of detecting magnetic fields with a sensitivity of $\sim$40 fT/$\sqrt{\text{Hz}}$. Thus, paramagnetic cryA constructs could be developed for use at Earth's field and below.

Finally, the cryA-DOTA construct developed as a T_1 relaxation agent has a center-to-center distance far smaller than what was assumed in the original lanthanide chemical shift agent calculations. At 11 $\mathring{A}$, dysprosium, terbium, and thulium agents could induce cryA chemical shift changes greater than 10 ppm. Furthermore, the use of alignment media such as bacteriophage or stretched gels would enhance the chemical shift displacement by an even larger amount. Simultaneous development of T_1 relaxation agents and chemical shift agents would offer increased experimental flexibility and could open the door to novel applications.

Chapter 9

Outlook

Remote detection of xenon-based molecular sensors on a microfluidic chip shows great promise to influence the design and implementation of biological and geochemical assays. An effort is currently being pushed forward in the Wemmer, Pines, and Francis labs to develop a library of peptides to uniquely screen for hydrophobicity, small molecules, etc. using the sensitivity of xenon to its local environment. These sensors could then be specifically deposited in an array on a microfluidic chip. A sample containing unlabeled analytes could then be injected onto the chip and allowed to interact with the library of sensors after which hyperpolarized xenon would be delivered to the chip for detection of perturbed XBMS. A series of scans will most likely be necessary to unambiguously resolve which combination of sensors the sample was interacting with, from which the sample's fingerprint could be compared to a set of standards for unique identification.

The ultimate vision for this project is lofty, but I strongly believe that it is achievable. There are a few developments that would significantly improve the time frame in which the goals could be met. Most importantly, remote detection of aqueous xenon in a microcoil is significantly dependent on the number of hyperpolarized xenon-129 atoms within the coil. The spin density of hyperpolarized can be increased by using a higher overall percentage of xenon in the gas mixture or by enriching the concentration of xenon-129 within the mixture, but both of these options are very expensive. Alternatively, the MITI or home-built polarizers could be optimized by renewed laser alignment and careful monitoring of the cell temperature to improve polarization from their current level at 1-2% to ∼15%. A more ambitious project would involve building a recirculating system similar to the polarizer developed by Hersmann, et al. to increase polarization of xenon-129 to even higher levels [75]. Furthermore, the lab-scale polarizers could be replaced by efficient chip-sized micropolarizers such as the ones in development in the Pines and Budker labs at UC Berkeley in collaboration with the Kitching group at NIST if their level of polarization exceeds that achieved with the traditional hyperpolarizers.

While convenient given the physical space constraints for the remote detection experiments and for avoiding gas bubbles in the system, use of the Membrana®membranes decreases the overall aqueous xenon signal by a factor of ∼4 relative to saturation of the solution via bubbling [114]. Design of a micro cell similar to large cell developed for the original continuous flow experiments [62] in which xenon gas could either be bubbled or more efficiently dissolved into water flowing to the encoding region would be of tremendous value. Given the space constraints, this project would most likely involve completely redesigning the entire remote detection platform.

The true power of microfluidic applications using XBMS will likely lie in their ability to be paired with low-field applications. Moving to low magnetic fields removes the dependency on large, costly, superconducting magnets. Single-sided low-field magnets [2] and atomic magnetometers [1] are currently commercially available. Combined with a set of low-field sensors such as the T_1 relaxation agents proposed in Chapter 8, these detection schemes could result in chemically sensitive, portable analytical devices.

Bibliography

[1] *GEM Systems - Advanced Magnetometers*, 2012 (accessed March 3, 2012). `http://www.gemsys.ca/apps_unexploded_ordnance.htm`.

[2] *The NMR-MOUSE Home*, 2012 (accessed March 3, 2012). `http://www.nmr-mouse.de`.

[3] A. Abragam. *Principles of Nuclear Magnetism.* Oxford University Press, Oxford, 1961.

[4] Silvio Aime, Lucio Anelli, Mauro Botta, Marino Brocchetta, Simonetta Canton, Franco Fedeli, Eliana Gianolio, and Enzo Terreno. Relaxometric evaluation of novel manganese(II) complexes for application as contrast agents in magnetic resonance imaging. *Journal of Biological Inorganic Chemistry*, 7:58–67, 2002.

[5] Silvio Aime, Daniela Delli Castelli, and Enzo Terreno. Highly sensitive MRI chemical exchange saturation transfer agents using liposomes. *Angewandte Chemie (International ed. in English)*, 44(34):5513–5, August 2005.

[6] Belinda S Akpa, Sinéad M Matthews, Andrew J Sederman, Kamran Yunus, Adrian C Fisher, Michael L Johns, and Lynn F Gladden. Study of miscible and immiscible flows in a microchannel using magnetic resonance imaging. *Analytical Chemistry*, 79(16):6128–34, August 2007.

[7] Mitchell S. Albert, Dilip Balamore, Daniel F. Kacher, Arvind K. Venkatesh, and Ferenc A. Jolesz. Hyperpolarized 129Xe T1 in oxygenated and deoxygenated blood. *NMR in Biomedicine*, 13(7):407–414, 2000.

[8] MS Albert, GD Cates, B Driehuys, W Happer, B Saam, CS Springer, and A Wishnia. Biological magnetic resonance imaging using hyperpolarized ^{129}Xe. *Nature*, 370:199–201, 1994.

[9] Dmitri Artemov. Molecular magnetic resonance imaging with targeted contrast agents. *Journal of Cellular Biochemistry*, 90(3):518–24, October 2003.

[10] Vikram S Bajaj, Jeffrey Paulsen, Elad Harel, and Alexander Pines. Zooming in on microscopic flow by remotely detected MRI. *Science*, 330:1078–81, 2010.

[11] Kristin Bartik, Michel Luhmer, Jean-pierre Dutasta, André Collet, and Jacques Reisse. ^{129}Xe and ^{1}H NMR Study of the Reversible Trapping of Xenon by Cryptophane-A in Organic Solution. *JACS*, 120(4):784–791, 1998.

[12] Kristin Bartik, Michel Luhmer, Stephen J. Heyes, Robert Ottinger, and Jacques Reisse. Probing Molecular Cavities in a-Cyclodextrin Solutions by Xenon NMR. *Journal of Magnetic Resonance, Series B*, 109(2):164 – 168, 1995.

[13] H F Bennett, R D Brown III, SH Koenig, and HM Swartz. Nitroxides on the Magnetic Field and Temperature Dependence of $1/T_1$ of Solvent Water Protons. *Magnetic Resonance in Medicine*, 4:93–111, 1987.

[14] Patrick Berthault, Aurore Bogaert-Buchmann, Herve Desvaux, Gaspard Huber, and Yves Boulard. Sensitivity and Multiplexing Capabilities of MRI Based on Polarized Xe Biosensors. *Journal of the American Chemical Society*, 130:16456–16457, 2008.

[15] Patrick Berthault, Gaspard Huber, and Hervé Desvaux. Biosensing using laser-polarized xenon NMR/MRI. *Progress in Nuclear Magnetic Resonance Spectroscopy*, 55(1):35–60, July 2009.

[16] A Bifone, YQ Song, R Seydoux, RE Taylor, BM Goodson, T Pietrass, TF Budinger, G Navon, and A Pines. NMR of laser-polarized xenon in human blood. *Proceedings of the National Academy of Sciences*, 93:12932 – 12936, 1996.

[17] B Bleaney. Nuclear Magnetic Resonance Shifts in Solution Due to Lanthanide Ions. *Journal of Magnetic Resonance*, 8:91–100, 1972.

[18] F Bloch. Nuclear Induction. *Physical Review*, 70:460–474, 1946.

[19] N Bloembergen. Proton Relaxation Times in Paramagnetic Solutions. *Journal of Chemical Physics*, 27(2):572–573, 1957.

[20] Babul Borah and Robert G Bryant. NMR relaxation dispersion in an aqueous nitroxide system. *J Chem Phys*, 75(7):3297–3300, 1981.

[21] Céline Boutin, Hervé Desvaux, Marie Carrière, François Leteurtre, Nadège Jamin, Yves Boulard, and Patrick Berthault. Hyperpolarized ^{129}Xe NMR signature of living biological cells. *NMR in Biomedicine*, 24(10):1264–1269, 2011.

[22] Céline Boutin, Antoine Stopin, Fatimazohra Lenda, Thierry Brotin, Jean-Pierre Dutasta, Nadège Jamin, Alain Sanson, Yves Boulard, François Leteurtre, Gaspard Huber, Aurore Bogaert-Buchmann, Nawal Tassali, Hervé Desvaux, Marie Carrière, and Patrick Berthault. Cell uptake of a biosensor detected by hyperpolarized ^{129}Xe NMR: The transferrin case. *Bioorganic & Medicinal Chemistry*, 19(13):4135–43, July 2011.

[23] C. R. Bowers, V. Storhaug, C. E. Webster, J. Bharatam, A. Cottone, R. Gianna, K. Betsey, and B. J. Gaffney. Exploring Surfaces and Cavities in Lipoxygenase and Other Proteins by Hyperpolarized Xenon-129 NMR. *Journal of the American Chemical Society*, 121(40):9370–9377, 1999.

[24] Neil Branda, Robert M. Grotzfeld, Carlos Valdés, and Julius Jr. Rebek. Control of Self-Assembly and Reversible Encapsulation of Xenon in a Self-Assembling Dimer by Acid-Base Chemistry. *Journal of the American Chemical Society*, 117(1):85–88, 1995.

[25] Rodney A. Brooks. T_2-shortening by strongly magnetized spheres: A chemical exchange model. *Magnetic Resonance in Medicine*, 47(2):388–391, 2002.

[26] Thierry Brotin and Jean-pierre Dutasta. Xe@cryptophane Complexes with C_2 Symmetry: Synthesis and Investigations by ^{129}Xe NMR of the Consequences of the Size of the Host Cavity for Xenon. *Eur. J. Org. Chem.*, 2003:973–984, 2003.

[27] Thierry Brotin, Anne Lesage, Lyndon Emsley, and André Collet. ^{129}Xe NMR Spectroscopy of Deuterium-Labeled Cryptophane-A Xenon Complexes: Investigation of Host-Guest Complexation Dynamics. *Journal of the American Chemical Society*, 122:1171–1174, 2000.

[28] H Carr and E Purcell. Effects of diffusion on free precession in nuclear magnetic resonance experiments. *Physical Review*, 94(3):630–638, 1954.

[29] Jennifer M Chambers, P Aru Hill, Julie A Aaron, Zhaohui Han, David W Christianson, Nicholas N Kuzma, and Ivan J Dmochowski. Cryptophane Xenon-129 Nuclear Magnetic Resonance Biosensors Targeting Human Carbonic Anhydrase Cryptophane Xenon-129 Nuclear Magnetic Resonance Biosensors Targeting Human Carbonic Anhydrase. *Journal of the American Chemical Soceity*, 131:563–569, 2009.

[30] Lana Joleen Chavez. *Applications of Clever Pulse Sequences to Detect the ^{129}Xe Biosensor with Enhanced Sensitivity and for a Fast Imaging Technique*. PhD thesis, University of California, Berkeley, 2007.

[31] R. Y. Chen, F. C. Fan, S. Kim, K. M. Jan, S. Usami, and S. Chien. Tissue-blood partition coefficient for xenon: temperature and hematocrit dependence. *Journal of Applied Physiology*, 49(2):178–183, 1980.

[32] Andrea Cherubini and Angelo Bifone. Hyperpolarised xenon in biology. *Progress in Nuclear Magnetic Resonance Spectroscopy*, 42(12):1 – 30, 2003.

[33] A Collet, JP Dutasta, B Lozach, and J Canceill. Cyclotriveratrylenes and Cryptophanes: Their Synthesis and Applications to Host-Guest Chemistry and to the Design of New Materials. *Topics in Current Chemistry*, 165:103–129, 1993.

[34] Charles H. Cunningham, Takayasu Arai, Phillip C. Yang, Michael V. McConnell, John M. Pauly, and Steven M. Conolly. Positive contrast magnetic resonance imaging of cells labeled with magnetic nanoparticles. *Magnetic Resonance in Medicine*, 53(5):999–1005, 2005.

[35] Vasiliki Demas and Thomas J Lowery. Magnetic resonance for *in vitro* medical diagnostics: superparamagnetic nanoparticle-based magnetic relaxation switches. *New Journal of Physics*, 13:025005, 2011.

[36] L W Dobrucki and a J Sinusas. Molecular imaging. A new approach to nuclear cardiology. *The Quarterly Journal of Nuclear Medicine and Molecular Imaging*, 49(1):106–115, March 2005.

[37] Bastiaan Driehuys, Gary P Cofer, Jim Pollaro, Julie Boslego Mackel, Laurence W Hedlund, and G Allan Johnson. Imaging alveolar-capillary gas transfer using hyperpolarized ^{129}Xe MRI. *Proceedings of the National Academy of Sciences of the United States of America*, 103:18278–18283, 2006.

[38] G Duhamel, P Choquet, E Grillon, L Lamalle, J L Leviel, a Ziegler, and a Constantinesco. Xenon-129 MR imaging and spectroscopy of rat brain using arterial delivery of hyperpolarized xenon in a lipid emulsion. *Magnetic Resonance in Medicine*, 46(2):208–12, 2001.

[39] RR Ernst, G Bodenhausen, and A Wokaun. *Principles of Nuclear Magnetic Resonance in One and Two Dimensions.* Oxford University Press, Oxford, 1990.

[40] Robert M Fairchild, Akil I Joseph, K Travis Holman, Heather A Fogarty, Thierry Brotin, Jean-pierre Dutasta, Céline Boutin, Gaspard Huber, and Patrick Berthault. A Water-Soluble Xe@cryptophane-111 Complex Exhibits Very High Thermodynamic Stability and a Peculiar ^{129}Xe NMR Chemical Shift. *Journal of the American Chemical Society*, 132:15505–15507, 2010.

[41] Heather A Fogarty, Patrick Berthault, Thierry Brotin, Gaspard Huber, Hervé Desvaux, and Jean-Pierre Dutasta. A Cryptophane Core Optimized for Xenon Encapsulation. *Journal of the American Chemical Society*, 129:10332–10333, 2007.

[42] Sture Forsén and Ragnar A. Hoffman. Study of Moderately Rapid Chemical Exchange Reactions by Means of Nuclear Magnetic Double Resonance. *The Journal of Chemical Physics*, 39(11):2892–2901, 1963.

[43] Jack H Freed. Dynamic effects of pair correlation functions on spin relaxation by translational diffusion in liquids. II. Finite jumps and independent T_1 processes. *Journal of Chemical Physics*, 68(9):4034–4037, 1978.

[44] Jacqueline Gabard and André Collet. Synthesis of a (D_3)-Bis(cyclotriveratrylenyl) Macrocage by Stereospecific Replication of a (C_3)-Subunit. *J.C.S. Chem. Comm.*, 21:1137–1139, 1981.

[45] Praveena Garimella, Tyler Meldrum, Leah Witium, Monica A Smith, Vikram S Bajaj, Matthew B Francis, David E Wemmer, and Alex Pines. Hyperpolarized xenon molecular sensors for label-free detection of analytes. *JACS*, In progress.

[46] M. Gatzke, G. D. Cates, B. Driehuys, D. Fox, W. Happer, and B. Saam. Extraordinarily slow nuclear spin relaxation in frozen laser-polarized ^{129}Xe. *Phys. Rev. Lett.*, 70:690–693, Feb 1993.

[47] L H Gevantman. *CRC Handbook of Chemistry and Physics.* CRC Press, 87 edition, 2006.

[48] E v Goldammer, W Kreysch, and H Wenzel. Proton NMR Relaxation Studies on Several Nitroxyl-Water Systems. *Journal of Solution Chemistry*, 7(3):197–204, 1978.

[49] Boyd M Goodson. Nuclear Magnetic Resonance of Laser-Polarized Noble Gases in Molecules, Materials, and Organisms. *Journal of Magnetic Resonance*, 155:157–216, 2002.

[50] J. Granwehr, E. Harel, S. Han, S. Garcia, A. Pines, P. Sen, and Y.-Q. Song. Time-of-Flight Flow Imaging Using NMR Remote Detection. *Physical Review Letters*, 95:075503, 2005.

[51] J. Granwehr and J.A. Seeley. Sensitivity quantification of remote detection NMR and MRI. *Journal of Magnetic Resonance*, 179(2):280 – 289, 2006.

[52] EL Hahn. Spin Echoes. *Physical Review*, 80(4):580–594, 1950.

[53] Nicholas W Halpern-Manners. *Applications of Magnetic Resonance to Current Detection and Microscale Flow Imaging*. PhD thesis, University of California, Berkeley, 2011.

[54] Nicholas W Halpern-Manners, Jeffrey L Paulsen, Vikram S Bajaj, and Alexander Pines. Remotely Detected MRI Velocimetry in Microporous Bead Packs. *The Journal of Physical Chemistry. A*, 115(16):4023–30, April 2011.

[55] Song-i Han, Sandra Garcia, Thomas J Lowery, E Janette Ruiz, Juliette A Seeley, Lana Chavez, David S King, David E Wemmer, and Alexander Pines. NMR-Based Biosensing with Optimized Delivery of Polarized ^{129}Xe to Solutions. *Analytical Chemistry*, 77:4008–4012, 2005.

[56] Ileana Hancu, W Thomas Dixon, Mark Woods, Elena Vinogradov, A Dean Sherry, and Robert E Lenkinski. CEST and PARACEST MR contrast agents. *Acta Radiologica*, 51(8):910–23, 2010.

[57] William Happer. Optical Pumping. *Reviews of Modern Physics*, 44:169–249, Apr 1972.

[58] Elad Harel, Christian Hilty, Katherine Koen, Erin McDonnell, and Alex Pines. Time-of-Flight Flow Imaging of Two-Component Flow inside a Microfluidic Chip. *Physical Review Letters*, 98(1):017601, January 2007.

[59] Elad Harel and Alex Pines. Spectrally resolved flow imaging of fluids inside a microfluidic chip with ultrahigh time resolution. *Journal of Magnetic Resonance*, 193(2):199–206, August 2008.

[60] P Aru Hill, Qian Wei, Roderic G Eckenhoff, and Ivan J Dmochowski. Thermodynamics of Xenon Binding to Cryptophane in Water and Human Plasma. *Journal of the American Chemical Society*, 129:9262–9263, 2007.

[61] P Aru Hill, Qian Wei, Thomas Troxler, and Ivan J Dmochowski. Substituent Effects on Xenon Binding Affinity and Solution Behavior of Water-Soluble Cryptophanes Substituent Effects on Xenon Binding Affinity and Solution Behavior of Water-Soluble Cryptophanes. *Journal of the American Chemical Society*, 131:3069–3077, 2009.

[62] Christian Hilty, Thomas J Lowery, and David E Wemmer. Spectrally Resolved Magnetic Resonance Imaging of a Xenon Biosensor. *Angew Chem Int Ed*, 45:70–73, 2006.

[63] D I Hoult and B Bhakar. NMR Signal Reception : Virtual Photons and Coherent Spontaneous. *Concepts in Magnetic Resonance*, 9:277–297, 1996.

[64] D.I Hoult and R.E Richards. The signal-to-noise ratio of the nuclear magnetic resonance experiment. *Journal of Magnetic Resonance*, 24(1):71 – 85, 1976.

[65] Gaspard Huber, Læ titia Beguin, Thierry Brotin, and Heather A Fogarty. Cryptophane-Xenon Complexes in Organic Solvents Observed through NMR Spectroscopy. *Synthesis*, 2008.

[66] Gaspard Huber, Thierry Brotin, and Lionel Dubois. Water Soluble Cryptophanes Showing Unprecedented Affinity for Xenon : Candidates as NMR-Based Biosensors. (4):6239–6246, 2006.

[67] ER Hunt and HY Carr. Nuclear Magnetic Resonance of Xe^{129} in Natural Xenon. *Physical Review*, 130(6), 1963.

[68] Cynthia J Jameson, A Keith Jameson, Rex Gerald, and Angel C de Dios. Nuclear magnetic resonance studies of xenon clusters in zeolite NaA. *Journal of Chemical Physics*, 96:1676–1689, 1992.

[69] Kastler, Alfred. Quelques suggestions concernant la production optique et la détection optique d'une inégalité de population des niveaux de quantifigation spatiale des atomes. Application à l'expérience de Stern et Gerlach et à la résonance magnétique. *J. Phys. Radium*, 11(6):255–265, 1950.

[70] James Keeler. *Understanding NMR Spectroscopy*. Wiley, 2005.

[71] RR Kennedy, JW Stokes, and P Downing. Anaesthesia and the 'Inert' Gases with Special Reference to Xenon. *Anaesth Intens Care*, 20:66–70, 1992.

[72] Chalermchai Khemtong, Chase W Kessinger, Jimin Ren, Erik A Bey, Su-Geun Yang, Jagadeesh Setti Guthi, David A Boothman, A Dean Sherry, and Jinming Gao. In vivo off-resonance saturation magnetic resonance imaging of $\alpha_v\beta_3$-targeted superparamagnetic nanoparticles. *Cancer Research*, 69(4):1651–8, February 2009.

[73] Wolfgang Kilian, Frank Seifert, and Herbert Rinneberg. Dynamic NMR Spectroscopy of Hyperpolarized ^{129}Xe in Human Brain Analyzed by an Uptake Model. *Magnetic Resonance in Medicine*, 51(4):843–7, April 2004.

[74] Lily Kim. *List of microfluidics companies*, 2011 (accessed December 29, 2011). `http://fluidicmems.com/list-of-microfluidics-lab-on-a-chip-and-biomems-companies/`.

[75] Kevin Knagge, Jonathan Prange, and Daniel Raftery. A continuously recirculating optical pumping apparatus for high xenon polarization and surface NMR studies. *Chemical Physics Letters*, 397:11–16, 2004.

[76] Randall B. Lauffer. Paramagnetic metal complexes as water proton relaxation agents for NMR imaging: theory and design. *Chemical Reviews*, 87(5):901–927, 1987.

[77] PC Lauterbur. Image Formation by induced local interactions: Examples employing nuclear magnetic resonance. *Nature*, 242:190–191, 1973.

[78] Cristina Lavini, Geoffrey S. Payne, Martin O. Leach, and Angelo Bifone. Intravenous delivery of hyperpolarized ^{129}Xe: a compartmental model. *NMR in Biomedicine*, 13(4):238–244, 2000.

[79] M. P. Ledbetter, I. M. Savukov, D. Budker, V. Shah, S. Knappe, J. Kitching, D. J. Michalak, S. Xu, and A. Pines. Zero-field remote detection of NMR with a microfabricated atomic magnetometer. *Proceedings of the National Academy of Sciences*, 105(7):2286–2290, 2008.

[80] MH Levitt. *Spin Dynamics: Basics of Nuclear Magnetic Resonance*. Wiley, Chicester, England, 2nd edition, 2008.

[81] Thomas J Lowery. *Biomolecular Sensing and Imaging using Hyperpolarized ^{129}Xe Magnetic Resonance*. PhD thesis, University of California, Berkeley, 2007.

[82] Thomas J Lowery, Michaeleen Doucleff, E Janette Ruiz, Seth M Rubin, Alexander Pines, and David E Wemmer. Distinguishing multiple chemotaxis Y protein conformations with laser-polarized ^{129}Xe NMR. *Protein Science*, 14:848–855, 2005.

[83] Thomas J Lowery, Sandra Garcia, Lana Chavez, E Janette Ruiz, Tom Wu, Thierry Brotin, Jean-pierre Dutasta, David S King, Peter G Schultz, Alex Pines, and David E Wemmer. Optimization of Xenon Biosensors for Detection of Protein Interactions. *ChemBioChem*, 7:65–73, 2006.

[84] Marcus R Makowski, Andrea J Wiethoff, Christian H P Jansen, and René M Botnar. Molecular imaging with targeted contrast agents. *Topics in Magnetic Resonance Imaging*, 20(4):247–59, August 2009.

[85] Venkatesh Mani, Karen C. Briley-Saebo, Vitalii V. Itskovich, Daniel D. Samber, and Zahi A. Fayad. Gradient echo acquisition for superparamagnetic particles with positive contrast (GRASP): Sequence characterization in membrane and glass superparamagnetic iron oxide phantoms at 1.5T and 3T. *Magnetic Resonance in Medicine*, 55(1):126–135, 2006.

[86] Shin Matsuoka, Samuel Patz, Mitchell S Albert, Yanping Sun, Rahim R Rizi, Warren B Gefter, and Hiroto Hatabu. Hyperpolarized Gas MR Imaging of the Lung: Current Status as a Research Tool. *Journal of Thoracic Imaging*, 24(3):181–8, August 2009.

[87] Harden M. McConnell. Reaction Rates by Nuclear Magnetic Resonance. *The Journal of Chemical Physics*, 28(3):430–431, 1958.

[88] Erin E McDonnell, SongI Han, Christian Hilty, Kimberly L Pierce, and Alexander Pines. NMR Analysis on Microfluidic Devices by Remote Detection. *Analytical Chemistry*, 77(24):8109–14, December 2005.

[89] Michael T McMahon, Assaf a Gilad, Jinyuan Zhou, Phillip Z Sun, Jeff W M Bulte, and Peter C M van Zijl. Quantifying exchange rates in chemical exchange saturation transfer agents using the saturation time and saturation power dependencies of the magnetization transfer effect on the magnetic resonance imaging signal (QUEST and QUESP): Ph calibration for poly-L-Lysine and a Starburst Dendrimer. *Magnetic Resonance in Medicine*, 55(4):836–47, April 2006.

[90] Sandro Mecozzi and Julius Rebek, Jr. The 55% Solution: A Formula for Molecular Recognition in the Liquid State. *Chemistry A European Journal*, 4(6):1016–1022, 1998.

[91] S Meiboom and D Gill. Spin-Echo Method for Measuring Nuclear Relaxation Times. *Review of Scientific Instruments*, 29(8):688–691, 1958.

[92] Tyler Meldrum, Leif Schröder, Philipp Denger, David E Wemmer, and Alexander Pines. Xenon-based Molecular Sensors in Lipid Suspensions. *Journal of Magnetic Resonance*, 205:242–246, 2010.

[93] Tyler Meldrum, Kristen L Seim, Vikram S Bajaj, Krishnan K Palaniappan, Wesley Wu, Matthew B Francis, David E Wemmer, and Alexander Pines. A Xenon-Based Molecular Sensor Assembled on an MS2 Viral Capsid Scaffold. *JACS*, 132:5936–5937, 2010.

[94] Adam J Moulé, Megan M Spence, Song-I Han, Juliette a Seeley, Kimberly L Pierce, Sunil Saxena, and Alexander Pines. Amplification of xenon NMR and MRI by remote detection. *Proceedings of the National Academy of Sciences of the United States of America*, 100(16):9122–7, August 2003.

[95] John P. Mugler, Bastiaan Driehuys, James R. Brookeman, Gordon D. Cates, Stuart S. Berr, Robert G. Bryant, Thomas M. Daniel, Eduard E. De Lange, J. Hunter Downs, Christopher J. Erickson, William Happer, Denise P. Hinton, Neal F. Kassel, Therese Maier, C. Douglas Phillips, Brian T. Saam, Karen L. Sauer, and Mark E. Wagshul. MR Imaging and Spectroscopy Using Hyperpolarized ^{129}Xe Gas: Preliminary Human Results. *Magnetic Resonance in Medicine*, 37(6):809–815, 1997.

[96] Justin L. Mynar, Thomas J. Lowery, David E. Wemmer, Alexander Pines, and Jean M. J. Fréchet. Xenon Biosensor Amplification via Dendrimer-Cage Supramolecular Constructs. *Journal of the American Chemical Society*, 128(19):6334–6335, 2006.

[97] DG Nishimura. *Principles of Magnetic Resonance Imaging.* Stanford University, Palo Alto, California, 2010.

[98] FS Orcutt and MH Seevers. A Method for Determining the Solubility of Gases in Pure Liquids or Solutions by the Van Slyke-Neill Manometric Apparatus. *J. Biol. Chem.*, 117:501–507, 1937.

[99] T Osuga and S Han. Proton magnetic resonance imaging of diffusion of high- and low- molecular-weight contrast agents in opaque porous media saturated with water. *Magnetic Resonance Imaging*, 22:1039–1042, 2004.

[100] S Patz, I Muradian, MI Hrovat, FW Hersman, H Hatabu, and J Butler. *MRI of the Lung*. Springer, 2009.

[101] Jeffrey Paulsen, Vikram S Bajaj, and Alexander Pines. Compressed sensing of remotely detected MRI velocimetry in microfluidics. *Journal of Magnetic Resonance*, 205(2):196–201, August 2010.

[102] Sharon Peled, Ferenc A Jolesz, Ching-Hua Tseng, Luigino Nascimben, Mitchell S Albert, and Ronald L Walsworth. Determinants of Tissue Delivery for ^{129}Xe Magnetic Resonance in Humans. *Magnetic Resonance in Medicine*, 36(3):340–344, 1996.

[103] Paul W Percival and James S Hyde. Saturation-recovery measurements of the spin-lattice relaxation times of some nitroxides in solution. *Journal of Magnetic Resonance (1969)*, 23(2):249 – 257, 1976.

[104] Guido Pintacuda, Ahmad Moshref, Ainars Leonchiks, Anatoly Sharipo, and Gottfried Otting. Site-specific labelling with a metal chelator for protein-structure refinement. *Journal of Biomolecular NMR*, 29:351–361, 2004.

[105] Gerald L Pollack, Richard P Kennan, Jeffrey F Himm, and Peter W Carr. Solubility of xenon in 45 organic solvents including cycloalkanes, acids, and alkanals: Experiment and theory. *J Chem Phys*, 90:6569–6579, 1989.

[106] C F Polnaszek and R G Bryant. Nitroxide radical induced solvent proton relaxation: Measurement of localized translational diffusion. *Journal of Chemical Physics*, 81(9):4038–4045, 1984.

[107] RM Ramirez, TK Stevens, MA Smith, DE Wemmer, and A Pines. Bloch-McConnell Modeling of HyperCEST with Xenon Biosensors. In progress.

[108] A. G. Redfield. On the theory of relaxation processes. *IBM J. Res. Dev.*, 1:19–31, January 1957.

[109] Vincent Roy, Thierry Brotin, Jean-pierre Dutasta, Marie-Hélène Charles, Thierry Delair, François Mallet, Gaspard Huber, Hervé Desvaux, Yves Boulard, and Patrick Berthault. A Cryptophane Biosensor for the Detection of Specific Nucleotide Targets through Xenon NMR Spectroscopy. *ChemPhysChem*, 8:2082 – 2085, 2007.

[110] Seth M Rubin, Megan M Spence, Ivan E Dimitrov, E Janette Ruiz, Alexander Pines, and David E Wemmer. Detection of a Conformational Change in Maltose Binding Protein by ^{129}Xe NMR Spectroscopy. *Journal of the American Chemical Society*, 123:8616–8617, 2001.

[111] Kai Ruppert, James R. Brookeman, Klaus D. Hagspiel, Bastiaan Driehuys, and John P. Mugler III. NMR of hyperpolarized ^{129}Xe in the canine chest: spectral dynamics during a breath-hold. *NMR in Biomedicine*, 13(4):220–228, 2000.

[112] I. C. Ruset, S. Ketel, and F. W. Hersman. Optical Pumping System Design for Large Production of Hyperpolarized ^{129}Xe. *Phys. Rev. Lett.*, 96:053002, Feb 2006.

[113] John F. Schenck. The role of magnetic susceptibility in magnetic resonance imaging: MRI magnetic compatibility of the first and second kinds. *Medical Physics*, 23(6):815–850, 1996.

[114] Franz Schilling. MRI Thermometry Based on Hyperpolarized Xenon Biosensors. Master's thesis, Julius - Maximilians University Wurzburg, 2009.

[115] Andreas Schlundt, Wolfgang Kilian, Michael Beyermann, Jana Sticht, Sebastian Günther, Sabine Höpner, Kirsten Falk, Olaf Roetzschke, Lorenz Mitschang, and Christian Freund. A Xenon-129 Biosensor for Monitoring MHC-Peptide Interactions. *Angew. Chem. Int. Ed.*, 48:4142–4145, 2009.

[116] L Schröder, TJ Lowery, C Hilty, DE Wemmer, and A Pines. Molecular Imaging Using a Targeted Magnetic Resonance Hyperpolarized Biosensor. *Science*, 314(2006):446–449, 2006.

[117] Leif Schröder, Lana Chavez, Tyler Meldrum, Monica Smith, Thomas J. Lowery, David E. Wemmer, and Alexander Pines. Temperature-Controlled Molecular Depolarization Gates in Nuclear Magnetic Resonance. *Angewandte Chemie International Edition*, 47(23):4316–4320, 2008.

[118] Leif Schröder, Tyler Meldrum, Monica Smith, Thomas J. Lowery, David E. Wemmer, and Alexander Pines. Temperature Response of ^{129}Xe Depolarization Transfer and Its Application for Ultrasensitive NMR Detection. *Phys. Rev. Lett.*, 100:257603, Jun 2008.

[119] Juliette A Seeley, Song-I Han, and Alexander Pines. Remotely detected high-field MRI of porous samples. *Journal of Magnetic Resonance*, 167(2):282–90, April 2004.

[120] Garry K Seward, Qian Wei, and Ivan J Dmochowski. Peptide-Mediated Cellular Uptake of Cryptophane. *Bioconjugate Chem*, 19:2129–2135, 2008.

[121] I. Solomon. Relaxation Processes in a System of Two Spins. *Phys. Rev.*, 99:559–565, Jul 1955.

[122] I Solomon and N Bloembergen. Nuclear Magnetic Interactions in the HF Molecule. *Journal of Chemical Physics*, 25(2):261–266, 1956.

[123] Yi-qiao Song, Boyd M Goodson, Rebecca E Taylor, David D Laws, Gil Navon, and Alexander Pines. Selective Enhancement of NMR Signals for α-Cyclodextrin with Laser-Polarized Xenon. *Angew. Chem. Int. Ed. Engl.*, 36:2368 – 2370, 1997.

[124] Megan M Spence, Seth M Rubin, Ivan E Dimitrov, E Janette Ruiz, David E Wemmer, Alexander Pines, Shao Qin, Feng Tian, and Peter G Schultz. Functionalized xenon as a biosensor. *PNAS*, 98(19):10654–10657, 2001.

[125] Megan M Spence, E Janette Ruiz, Seth M Rubin, Thomas J Lowery, Nicolas Winssinger, Peter G Schultz, David E Wemmer, and Alexander Pines. Development of a Functionalized Xenon Biosensor. *Journal of the American Chemical Society*, 126:15287–15294, 2004.

[126] Todd K. Stevens, Krishnan K. Palaniappan, R. Matthew Ramirez, Matthew B. Francis, David E. Wemmer, and Alex Pines. HyperCEST detection of a 129Xe-based contrast agent composed of cryptophane-A molecular cages on a bacteriophage scaffold. *Magnetic Resonance in Medicine*, Submitted.

[127] Scott D. Swanson, Matthew S. Rosen, Bernard W. Agranoff, Kevin P. Coulter, Robert C. Welsh, and Timothy E. Chupp. Brain MRI with laser-polarized ^{129}Xe. *Magnetic Resonance in Medicine*, 38(5):695–698, 1997.

[128] M. S. Syamala, R. James Cross, and Martin Saunders. ^{129}Xe NMR Spectrum of Xenon Inside C_{60}. *Journal of the American Chemical Society*, 124(21):6216–6219, 2002.

[129] Pei Tang, Wei-jyun Chien, and Gerard S Harbison. Double-resonance circuit for nuclear magnetic resonance spectroscopy. *Solid State Nuclear Magnetic Resonance*, 2:343–348, 1993.

[130] Thomas Z Teisseyre, Jiri Urban, Nicholas W Halpern-manners, Stuart D Chambers, Vikram S Bajaj, Frantisek Svec, and Alexander Pines. Remotely Detected NMR for the Characterization of Flow and Fast Chromatographic Separations Using Organic Polyer Monoliths. *Analytical Chemistry*, 83:6004–6010, 2011.

[131] Ville-Veikko Telkki, Christian Hilty, Sandra Garcia, Elad Harel, and Alexander Pines. Quantifying the Diffusion of a Fluid through Membranes by Double Phase Encoded Remote Detection Magnetic Resonance Imaging. *J Phys Chem B*, 111:13929–13936, 2007.

[132] R. F. Tilton and I. D. Kuntz. Nuclear magnetic resonance studies of xenon-129 with myoglobin and hemoglobin. *Biochemistry*, 21(26):6850–6857, 1982.

[133] J D Trumbull, I K Glasgow, D J Beebe, and R L Magin. Integrating Microfabricated Fluidic Systems and NMR Spectroscopy. *IEEE Transactions on Biomedical Engineering*, 47(1):3–7, 2000.

[134] Arvind K. Venkatesh, Lei Zhao, Dilip Balamore, Ferenc A. Jolesz, and Mitchell S. Albert. Evaluation of carrier agents for hyperpolarized xenon MRI. *NMR in Biomedicine*, 13(4):245–252, 2000.

[135] F Verpillat, M P Ledbetter, S Xu, D J Michalak, C Hilty, L Bouchard, S Antonijevic, and D Budker. Remote detection of nuclear magnetic resonance with an anisotropic magnetoresistive sensor. *PNAS*, 105:2271–2273, 2007.

[136] Thad G. Walker and William Happer. Spin-exchange optical pumping of noble-gas nuclei. *Rev. Mod. Phys.*, 69:629–642, Apr 1997.

[137] K M Ward and R S Balaban. Determination of pH using water protons and chemical exchange dependent saturation transfer (CEST). *Magnetic Resonance in Medicine*, 44(5):799–802, November 2000.

[138] K.M Ward, A.H Aletras, and R.S Balaban. A New Class of Contrast Agents for MRI Based on Proton Chemical Exchange Dependent Saturation Transfer (CEST). *Journal of Magnetic Resonance*, 143(1):79 – 87, 2000.

[139] A.G. Webb and S.C. Grant. Signal-to-Noise and Magnetic Susceptibility Trade-offs in Solenoidal Microcoils for NMR. *Journal of Magnetic Resonance, Series B*, 113(1):83 – 87, 1996.

[140] Qian Wei, Garry K Seward, P Aru Hill, Brian Patton, Ivan E Dimitrov, Nicholas N Kuzma, and Ivan J Dmochowski. Designing ^{129}Xe NMR Biosensors for Matrix Metalloproteinase Detection. *Journal of the American Chemical Society*, 128:13274–13283, 2006.

[141] Ralph Weissleder. Scaling down imaging: molecular mapping of cancer in mice. *Nature Reviews Cancer*, 2(1):11–18, January 2002.

[142] Henk Wensink, Fernando Benito-lopez, Dorothee C Hermes, Willem Verboom, Han J G E Gardeniers, N Reinhoudt, and Albert Van Den Berg. Measuring reaction kinetics in a lab-on-a-chip by microcoil NMR. *Lab on a Chip*, 5:280–284, 2005.

[143] Eric J Werner, Ankona Datta, Christoph J Jocher, and Kenneth N Raymond. High-Relaxivity MRI Contrast Agents: Where Coordination Chemistry Meets Medical Imaging. *Angew. Chem. Int. Ed.*, 47:8568–8580, 2008.

[144] R. Wiebe and V. L. Gaddy. The Solubility of Helium in Water at 0, 25, 50 and 75° and at Pressures to 1000 Atmospheres. *Journal of the American Chemical Society*, 57:847–851, 1935.

[145] Jan Wolber, Simon J Doran, Martin O Leach, and Angelo Bifone. Measuring diffusion of xenon in solution with hyperpolarized ^{129}Xe NMR. *Chemical Physics Letters*, 296:391–396, 1998.

[146] Annjoe Wong-Foy, Sunil Saxena, Adam J. Moulé, Hans-Marcus L. Bitter, Juliette A. Seeley, Robert McDermott, John Clarke, and Alexander Pines. Laser-polarized ^{129}Xe NMR and MRI at Ultralow Magnetic Fields. *Journal of Magnetic Resonance*, 157(2):235 – 241, 2002.

[147] Shoujun Xu, Valeriy V. Yashchuk, Marcus H. Donaldson, Simon M. Rochester, Dmitry Budker, and Alexander Pines. Magnetic resonance imaging with an optical atomic magnetometer. *Proceedings of the National Academy of Sciences*, 103(34):12668–12671, 2006.

[148] X. Zeng, E. Miron, W.A. Van Wijngaarden, David Schreiber, and W. Happer. Wall relaxation of spin polarized ^{129}Xe nuclei. *Physics Letters A*, 96(4):191 – 194, 1983.

[149] Q W Zhang, Huiming Zhang, D K Lee, C H Bradley, and R J Wittebort. Double and Triple Resonance Circuits for High-Frequency Probes. *Journal of Magnetic Resonance*, 171(132):167–171, 1998.

[150] Shanrong Zhang, Matthew Merritt, Donald E Woessner, Robert E Lenkinski, and A Dean Sherry. PARACEST agents: Modulating MRI Contrast via Water Proton Exchange. *Accounts of Chemical Research*, 36(10):783–90, October 2003.

[151] Jinyuan Zhou and Peter C.M. Van Zijl. Chemical exchange saturation transfer imaging and spectroscopy. *Progress in Nuclear Magnetic Resonance Spectroscopy*, 48(2-3):109–136, May 2006.

[152] Xin Zhou, Dominic Graziani, and Alexander Pines. Hyperpolarized xenon NMR and MRI signal amplification by gas extraction. *Proceedings of the National Academy of Sciences*, 106(40):16903–16906, 2009.

Appendix A

Matlab Simulation Code

Below, the Matlab ®code for modeling the effects of T_1 relaxation on a paramagnetic XMBS are presented.

```
%Script developed to determine the contrast generated due to enhanced T1
%relaxation for a paramagnetic cryA XBMS - MAS 03/03/2012

clear all
satdly=0;

%% Variables

agent='Mn';                %Cu or Mn
cAgent = 20*10^-6;         %concentration of agent ( = concentration of cage)
cCage = cAgent;

T = 298;                   %Temperature, K
tau_M = 30*10^-3;          %bound lifetime, sec

pres = 65;                 %psi
Bfield = 7.05;             %T
r_test = 1.0*10^-9;        %center to center distance, m
bind = 10000;              %Association rate constant, 1/M

%% Parameters

field_range = 'high';
if strcmp(agent,'Gd')
    r=0.313*10^-9;                 %m, typical Gd complex
    a=r;
    S = 7/2;                       %nuclear spin of Gd
    q=1;
    D_S = 0.4*10^-9;               %Gd-DTPA (Osuga, 2004), m^2/sec, 25C
   %T1e = 0.001*10^-9;             %electron longitudinal relaxation time,
```

```
                                    %sec (Lauffer: 0.1 - 1ns)
    T1e = 0.1*10^-9;             %electron longitudinal relaxation time,
                                    %sec (Lauffer: 0.1 - 1ns)
    T2e = T1e;                   %electron spin relaxation time, sec,
                                    %(Lauffer: 0.1 - 1ns)
elseif strcmp(agent,'Mn')
    r=0.35*10^-9;                %m, Mn-EDTA complexes, Aime 2001
    a=r;
    S = 5/2;                     %nuclear spin of Gd
    q=1;
    D_S = 1.3*10^-9;             %MnCl2 - Osuga, 2004
    if strcmp(field_range,'high')
        T1e = 5.4*10^-9;         %electronic relaxation time constant, 14.1T
    elseif strcmp(field_range,'low')
        T1e = 1.5*10^-9;         %approximate, from Aime at 0.47T
    end
    T2e = T1e;
elseif strcmp(agent,'nitroxide')
    r = 0.25*10^-9;              %m,distance between xenon and paramagnetic
                                    %center, first hydration sphere, 40 C,
                                    %Goldammer
    a = 0.26*10^-9;              %m, closest approach for outer sphere
                                    %equations, 25C, Bennett
    S=1/2;                       %nuclear spin of nitroxide
    q=2.4;
    D_S = 1.53*10^-9;            %TEMPO (Bennett, 1986), m^2/sec, 25C

    %Stokes Law or experimental, rotational tumbling constant
    %eta = 1*10^-3;                        %viscosity of water, 25C, Pa*s
    %k = 1.38*10^-23;                      %Boltzmann constant, J/K
    %tau_R = (4*pi/3)*r^3*eta/(k*T);       %rotational tumbling time constant
    tau_R = 16*10^-12;                     %Stokes at 298 K
    T1e = 100*10^-9;        %electron longitudinal relaxation time, sec
    T2e = T1e;
end

if strcmp(agent,'nitroxide')
    r = 0.25*10^-9;                        %m,distance between xenon and
                                              %paramagnetic center, first
                                              %hydration sphere, 40 C,
                                              %Goldammer
    %Stokes Law for rotational tumbling constant
    eta = 1*10^-3;                         %viscosity of water, 25C, Pa*s
    k = 1.38*10^-23;                       %Boltzmann constant, J/K
    tau_R = (4*pi/3)*r^3*eta/(k*T);        %rotational tumbling time constant
```

```
elseif strcmp(agent,'Gd')
    tau_R = 0.1*10^-9;                  %Gd complex, freely rotating
    %tau_R = 10*10^-9;
elseif strcmp(agent,'Mn')
    tau_R = 0.1*10^-9;                  %Gd-DTPA ~ Mn-EDTA-BOM, Aime
    %tau_R = 10*10^-9;
end

if satdly==1
    wait=0:0.025:20;                %wait time before taking measurement
else
    wait=10;
end

gamma_I = 2*pi*11.777*10^6;   %gyromagnetic ratio, xenon 3.969
gamma_S = 2*pi*2.8*10^10;   %gyromagnetic ration, electron, Hz/T

pXe = 2;                    %Percent xenon
T1c = 15;                   %initial values, sec
T1w = 60;                   %initial values, sec
R1w = 1/T1w;
R1c = 1/T1c;

%% T1 of xenon in water in the presense of the agent
T1w_new = findBulkT1Relaxation_OS_13Mar2012(T1w,cAgent,agent,pXe,...
    pres,T,T1e,Bfield);  %T1 of xenon@water in presence of nitroxide
R1w_new = 1/T1w_new;
fprintf('T1w_new = %d  \n',T1w_new);

%% Contrast agent effects -> T1c_new

[T1IS,R1IS, R1M] = findT1atR_IS_26Mar2011(S,gamma_I,r_test,tau_R,Bfield,...
    T1e,tau_M,pXe,cAgent,T,pres,bind);
R1c_new = R1IS + (1/T1c);
T1c_new = 1/R1c_new;

fprintf('R1M = %d  \n',R1M);
fprintf('R1IS = %d  \n',R1IS);


%% Finding the difference in the Xe@H2O signal
%Normalize to initial polarized Xe signal = 1

if satdly==1
    M0_agent = findSignal_genmathematica_19Mar2011(R1w_new, 0,bind,...
```

```
        cCage,T,pres,pXe,wait);
    M0_agent_cage = findSignal_genmathematica_19Mar2011(R1w_new, ...
        R1c_new,bind,cCage, T,pres,pXe,wait);

    rem = (M0_agent - M0_agent_cage)./M0_agent;
    pct_diff = rem*100;

    figure(1)
    plot(wait, pct_diff,'k')
    %axis([0 2 0 1])
    xlabel('Wait (sec)')
    ylabel('Delta(M)(%)')
    title('Paramagnetic Cryptophane T1 Relaxation vs. Time')

else
    M0_agent = findSignal_genmathematica_19Mar2011(R1w_new, 0,bind,...
        cCage,T,pres,pXe,wait);
    M0_agent_cage = findSignal_genmathematica_19Mar2011(R1w_new,...
        R1c_new,bind, cCage, T,pres,pXe,wait);

    rem = (M0_agent - M0_agent_cage)/M0_agent;
    pct_diff = rem*100;
    fprintf('M0_agent = %d \n',M0_agent);
    fprintf('M0_agent-cage = %d \n',M0_agent_cage);
    fprintf('Percent difference = %d after a %d second wait \n',...
        pct_diff,wait);
end

function [T1total] = findBulkT1Relaxation_OS_13Mar2012(T1_send,cAgent,name,pX

% Modified from findBulkT1Relaxation_06May2011.m.


%% Variables

agent = name;           %choose Gd or nitroxide

D_I = 2.2*10^-9;        %m^2/sec, diffusion coefficient, 25C
                        %(water and xenon in water)
C_S = cAgent;           %concentration of agent, M

if strcmp(agent,'nitroxide')
    a = 0.26*10^-9;     %m, closest approach for outer sphere equations,
                                %25C, Bennett
    S=1/2;              %nuclear spin of nitroxide
```

```
    D_S = 1.53*10^-9;  %TEMPO (Bennett, 1986), m^2/sec, 25C


elseif strcmp(agent,'Gd')
    r=0.313*10^-9;                  %m, typical Gd complex
    a=r;
    S = 7/2;                        %nuclear spin of Gd
    D_S = 0.4*10^-9;                %Gd-DTPA (Osuga, 2004), m^2/sec, 25C

elseif strcmp(agent,'Mn')
    r=0.35*10^-9;                   %m, Mn-EDTA complexes, Aime 2001
    a=r;
    S = 5/2;                        %nuclear spin of Gd
    D_S = 1.3*10^-9;                %MnCl2 - Osuga, 2004

end

%% Initialization

T10 = T1_send;        %approximate, seconds
u0 = 4*pi*10^-7; %permeability of free space N/A^2
hbar = 1.055*10^-34; %Js
gamma_I = 2*pi*11.777*10^6;  %gyromagnetic ratio, xenon, rad/secT
gamma_S = 2*pi*2.8*10^10;    %gyromagnetic ration, electron, Hz/T

w_I = gamma_I*Bfield;   %larmor frequency, xenon, Hz
w_S = gamma_S*Bfield;%larmor frequency, electron, Hz


%% Outer sphere equations

D= (D_I + D_S);
tau_t = a^2/D; %sec
Const = (32*pi/405)*(u0/(4*pi))^2*(gamma_I)^2*(gamma_S)^2*...
    hbar^2*S*(S+1)*(6.022*10^26)*(C_S/(a*D));

%Includes electronic relaxation rate based on Freed
numeratorI = (1 + (1/4)*sqrt((1i*w_I*tau_t)+(tau_t/T1e)));
denominatorI = (1 + sqrt((1i*w_I*tau_t)+(tau_t/T1e)) +...
    (4/9)*((1i*w_I*tau_t)+(tau_t/T1e)) + (1/9)*((1i*w_I*tau_t)+...
    (tau_t/T1e))^(3/2));
numeratorS = (1 + (1/4)*sqrt((1i*w_S*tau_t)+(tau_t/T1e)));
denominatorS = (1 + sqrt((1i*w_S*tau_t)+(tau_t/T1e)) +...
    (4/9)*((1i*w_S*tau_t)+(tau_t/T1e)) + (1/9)*((1i*w_S*tau_t)+...
    (tau_t/T1e))^(3/2));
```

```
jwI = real(numeratorI/denominatorI);
jwS = real(numeratorS/denominatorS);

%T1 Outer sphere, Bennett 1986
PM = 0;
R1OS_prep = Const*(3*jwI + 7*jwS);
R1OS = (1-PM)*R1OS_prep;

%% Total Relaxation
R1P = R1OS;

R1total = R1P + (1/T10);     %paramagnetic + diamagnetic
T1total = 1/R1total;

end

function [T1IS,R1IS,R1M] = findT1atR_IS_03Mar2012(S,gamma_I,r,tau_R,Bfield,T1
    tau_M,pXe,cAgent,T,pres,bind)

% Modified from findT1atR_Construct_IS_18Mar2011
% Adds back in tau_M

%% Initialization

% Solubility
Tstar = T/100;
xe = pXe*0.01;  %xenon
pressure = pres;  %psi
solubility = exp(-74.7398 + (105.21/Tstar) + (27.4664*log(Tstar)));

C_I_xe = xe*(pressure/14.7)*55.6*solubility;   %concentration of xenon, M
occupancy=bind*C_I_xe./(bind*C_I_xe+1);
PM = cAgent*occupancy/C_I_xe;          %mole fraction of bound water/xenon

%PM = 1; %test

u0 = 4*pi*10^-7; %permeability of free space N/A^2
hbar = 1.055*10^-34; %Js
gamma_S = 2*pi*2.8*10^10;    %gyromagnetic ration, electron, Hz/T

w_I = gamma_I*Bfield;   %larmor frequency, xenon, Hz
w_S = gamma_S*Bfield;%larmor frequency, electron, Hz

T2e = T1e;
```

```
%% Inner sphere equations

rho_c1 = (1/tau_R) + (1/tau_M) + (1/T1e);
rho_c2 = (1/tau_R) + (1/tau_M) + (1/T2e);

tau_c1 = 1/rho_c1;
tau_c2 = 1/rho_c2;


%Note: no scalar term
R1M = ((2/15)*(u0/(4*pi))^2*(gamma_I^2*gamma_S^2*S*(S+1)*hbar^2/r^6)*...
    ((6*tau_c2/(1+((w_S+w_I)^2*tau_c2^2)))+(3*tau_c1/(1+...
    (w_I^2*tau_c1^2)))+(tau_c2/(1+((w_I-w_S)^2*tau_c2^2)))));
T1M = 1/R1M;

R1IS = PM / (T1M + tau_M);    % Inner sphere relaxation (Hz)
T1IS = 1/R1IS;

end
```

Appendix B

Double Resonance Remote Detection Probe

Below are the schematics for the double resonance remote detection probe developed for this thesis. All dimensions are given in inches. All of the components given in this Appendix were fabricated in the machine shop at UC Berkeley, from which the parts were assembled to construct the double resonance probe.

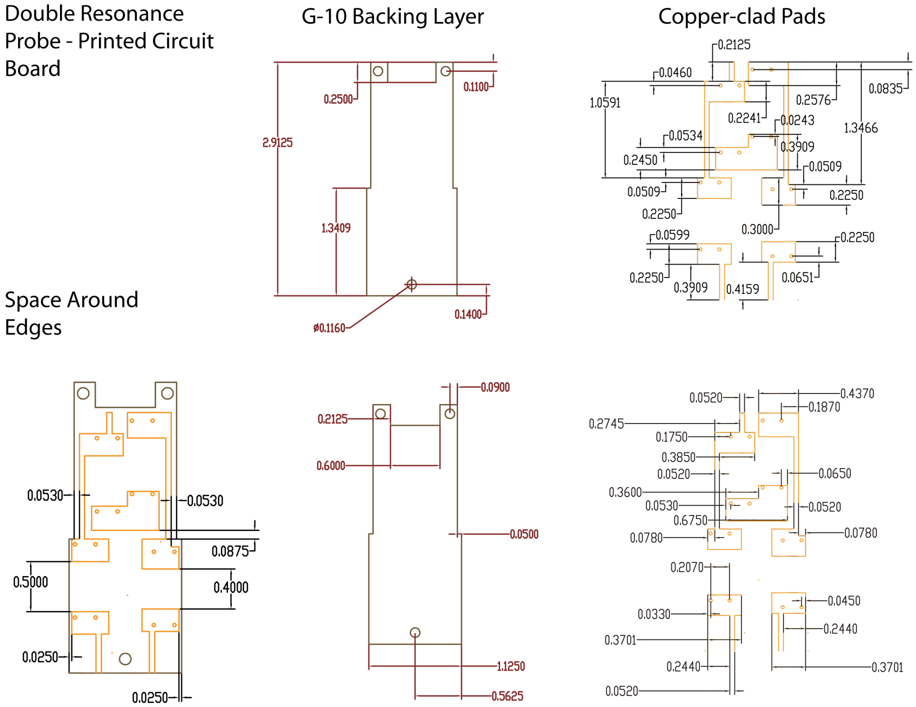

Figure B.1: Double Resonance Printed Circuit Board

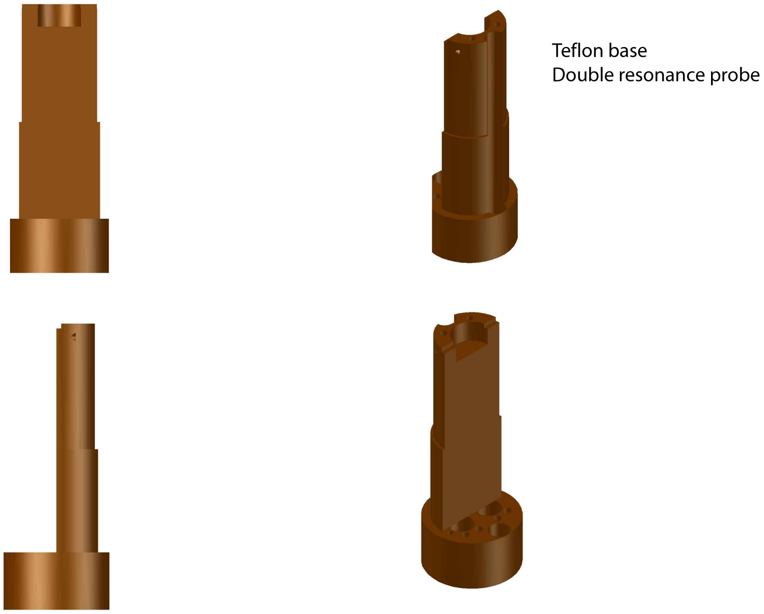

Figure B.2: Three Dimensional Rendering of the Teflon Base

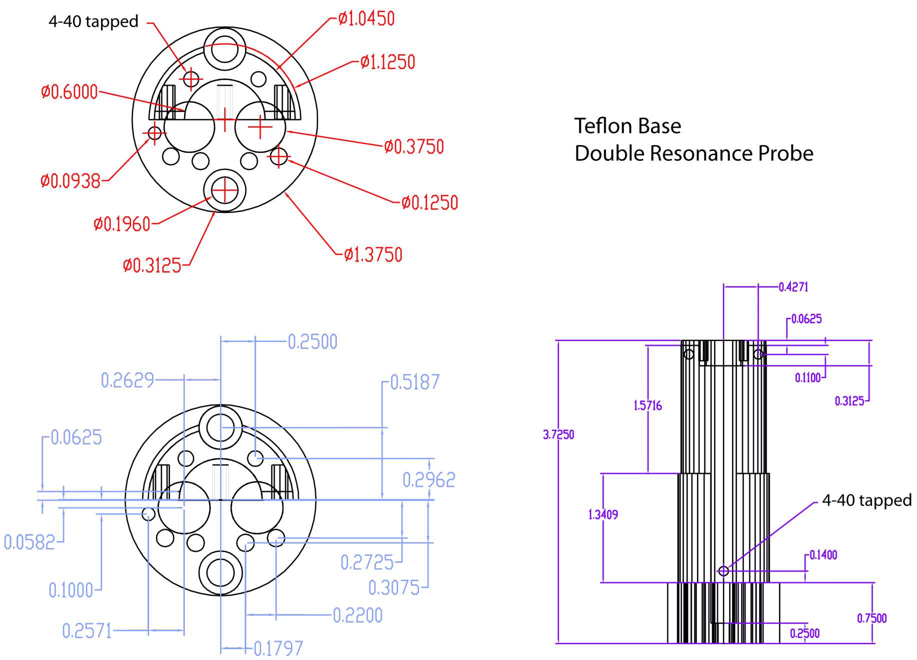

Figure B.3: Double Resonance Teflon Base

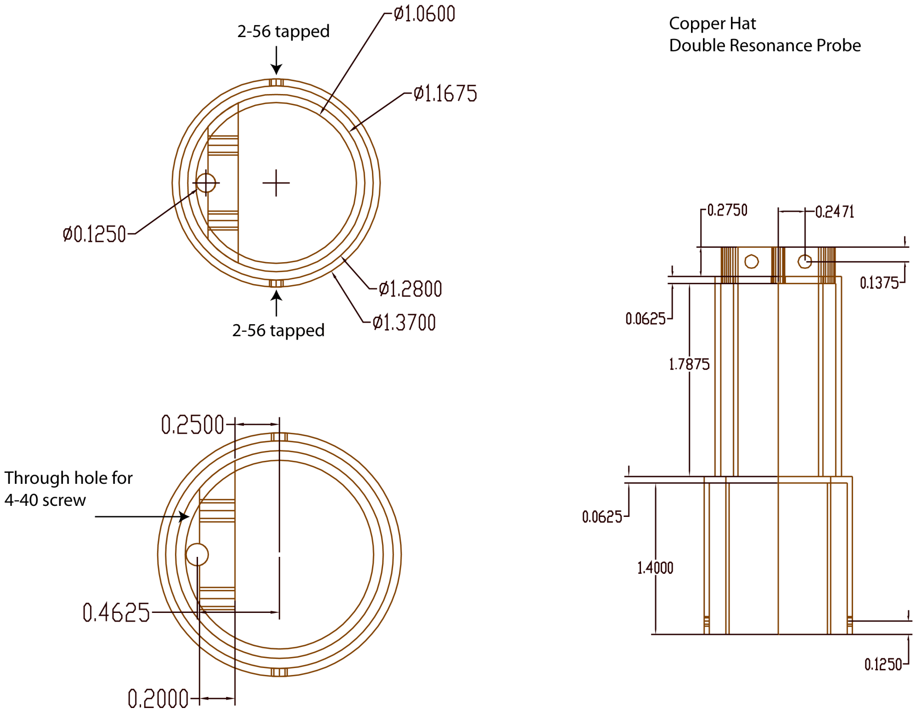

Figure B.4: Double Resonance Copper Hat

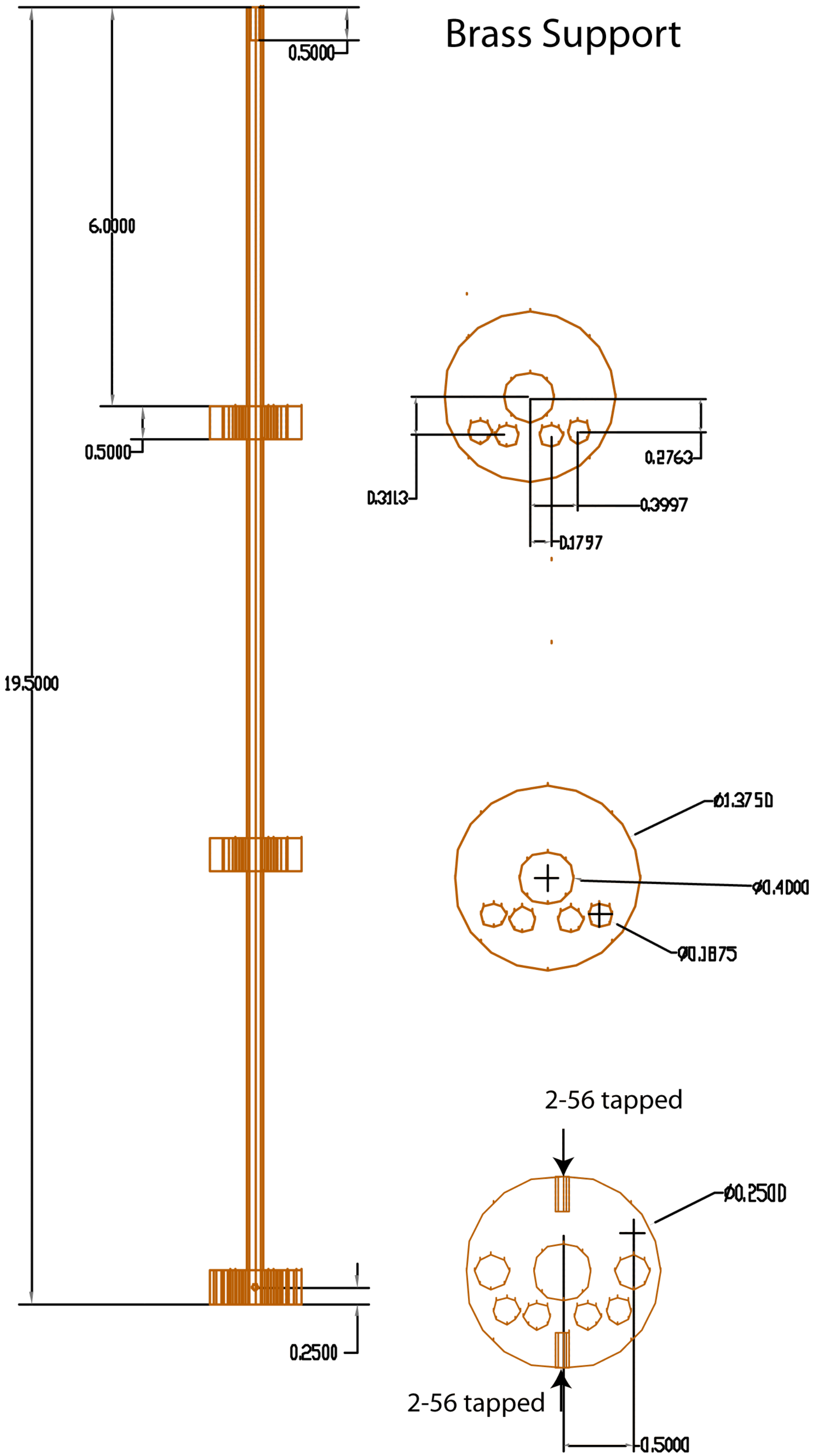

Figure B.5: Double Resonance Brass Support

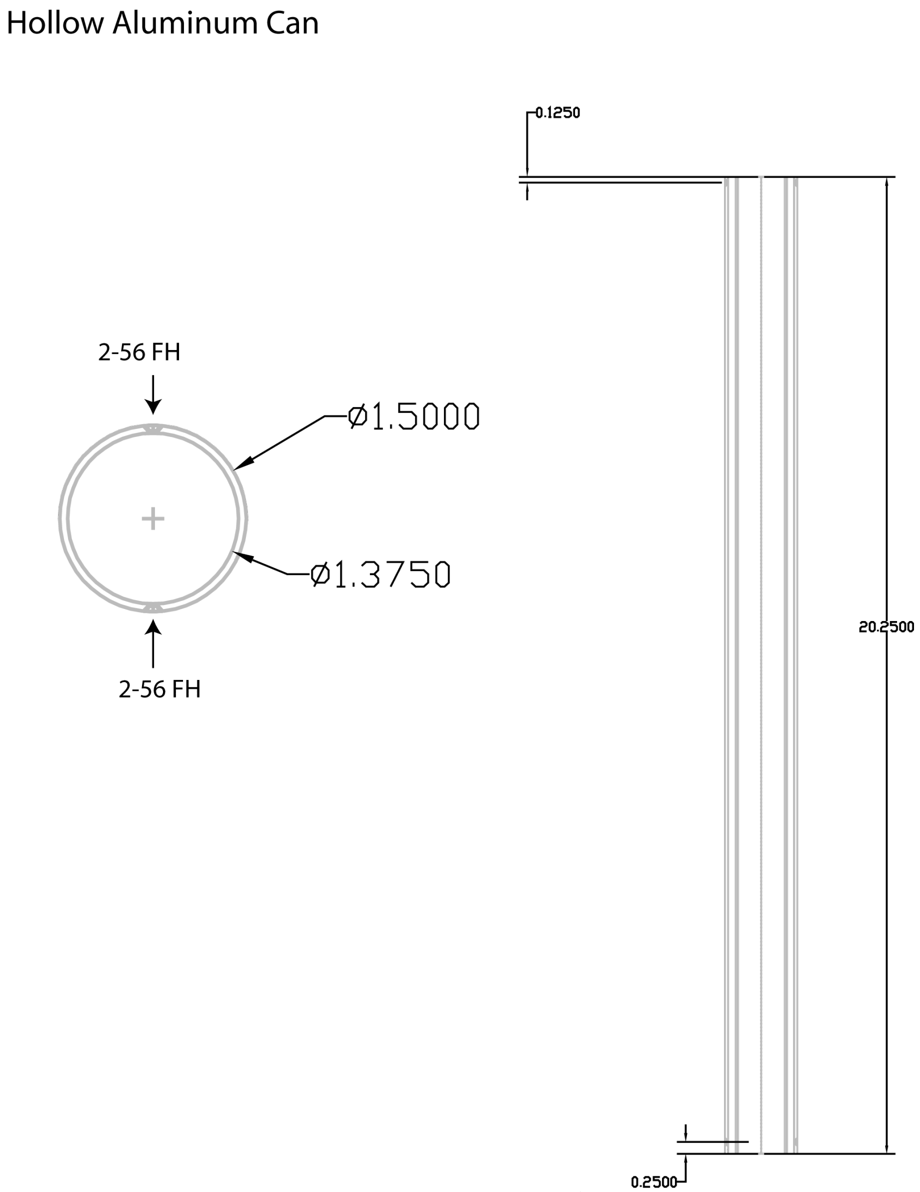

Figure B.6: Double Resonance Aluminum Can

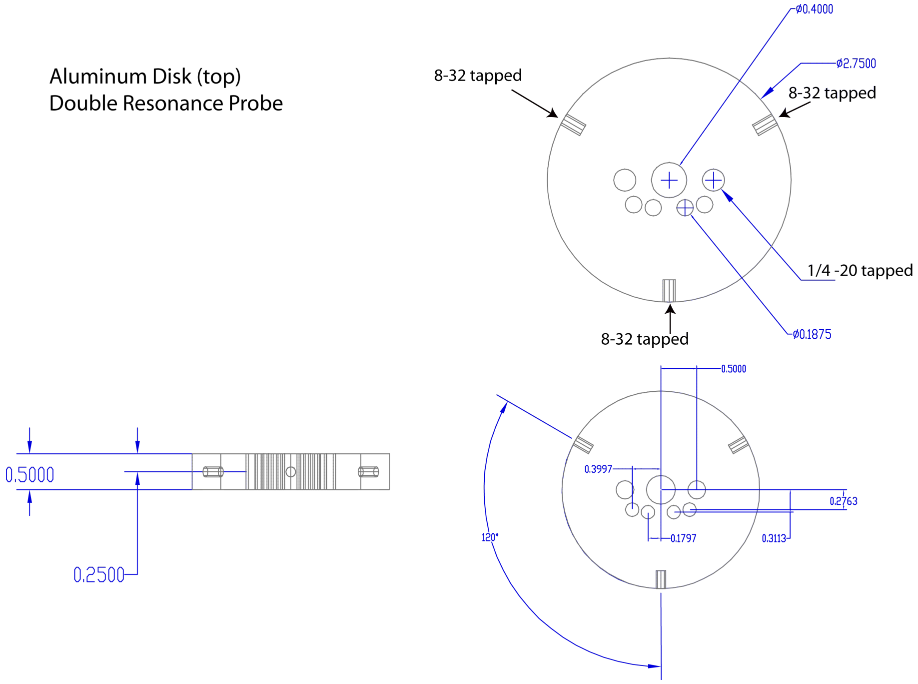

Figure B.7: Double Resonance Aluminum Plate

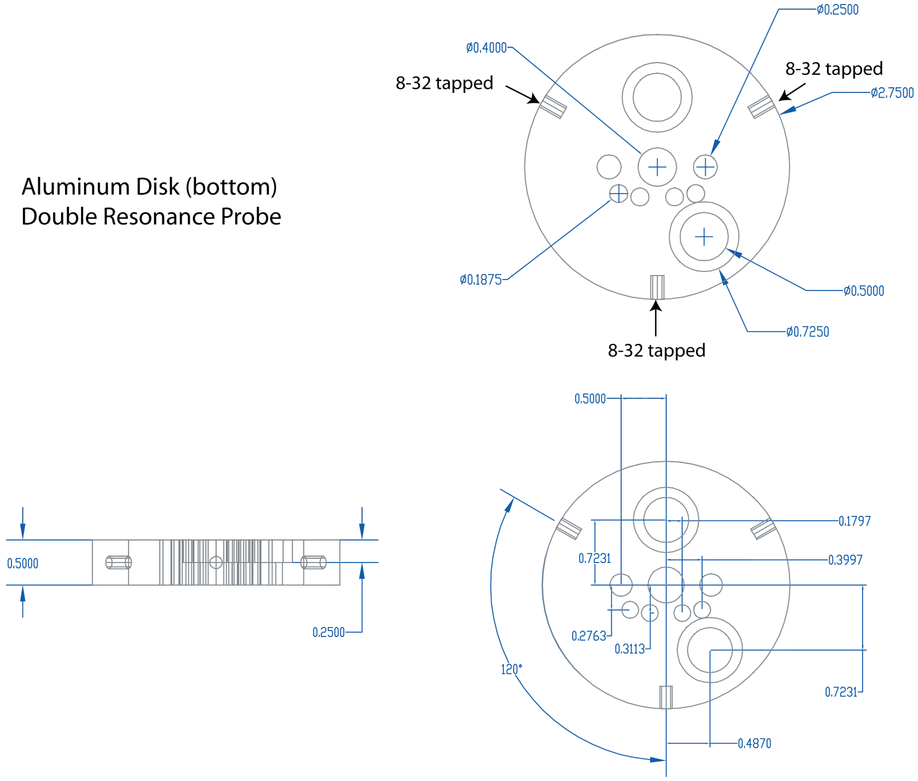

Figure B.8: Double Resonance Aluminum Plate 2

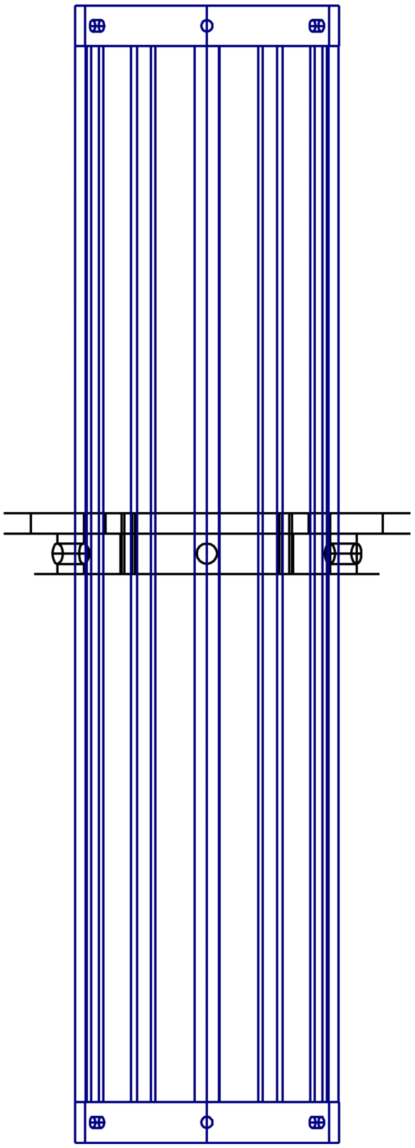

Birdcage Components
1) Aluminum cage
2) Aluminum spacer

Figure B.9: Double Resonance Cage and Spacer Assembly

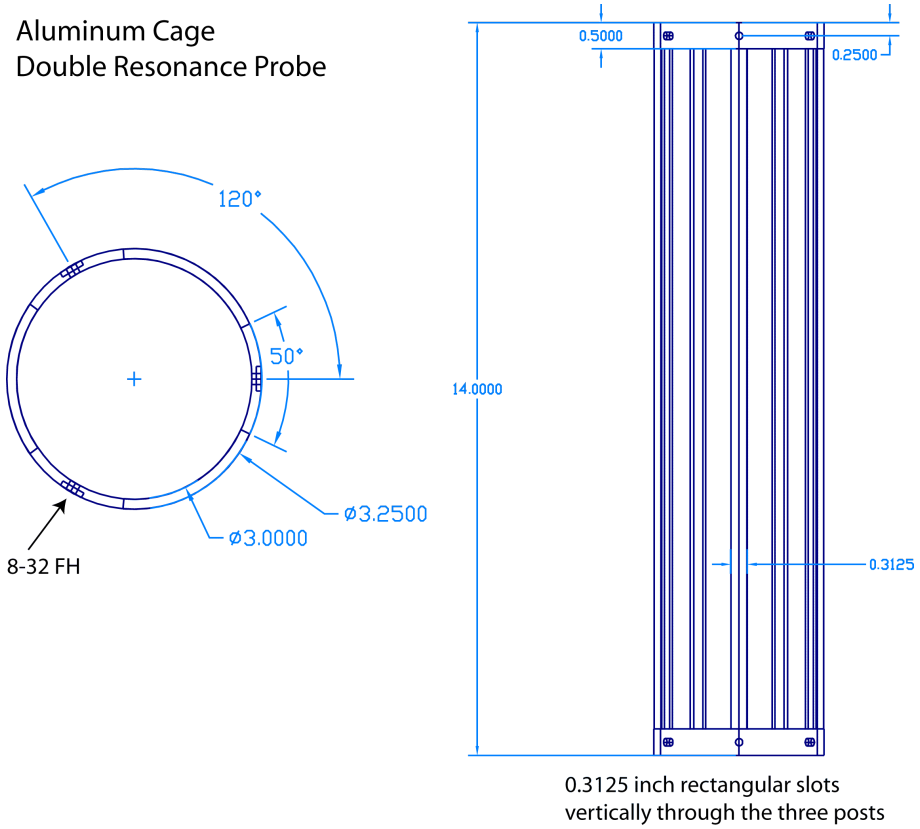
Aluminum Cage
Double Resonance Probe

0.3125 inch rectangular slots
vertically through the three posts

Figure B.10: Double Resonance Birdcage

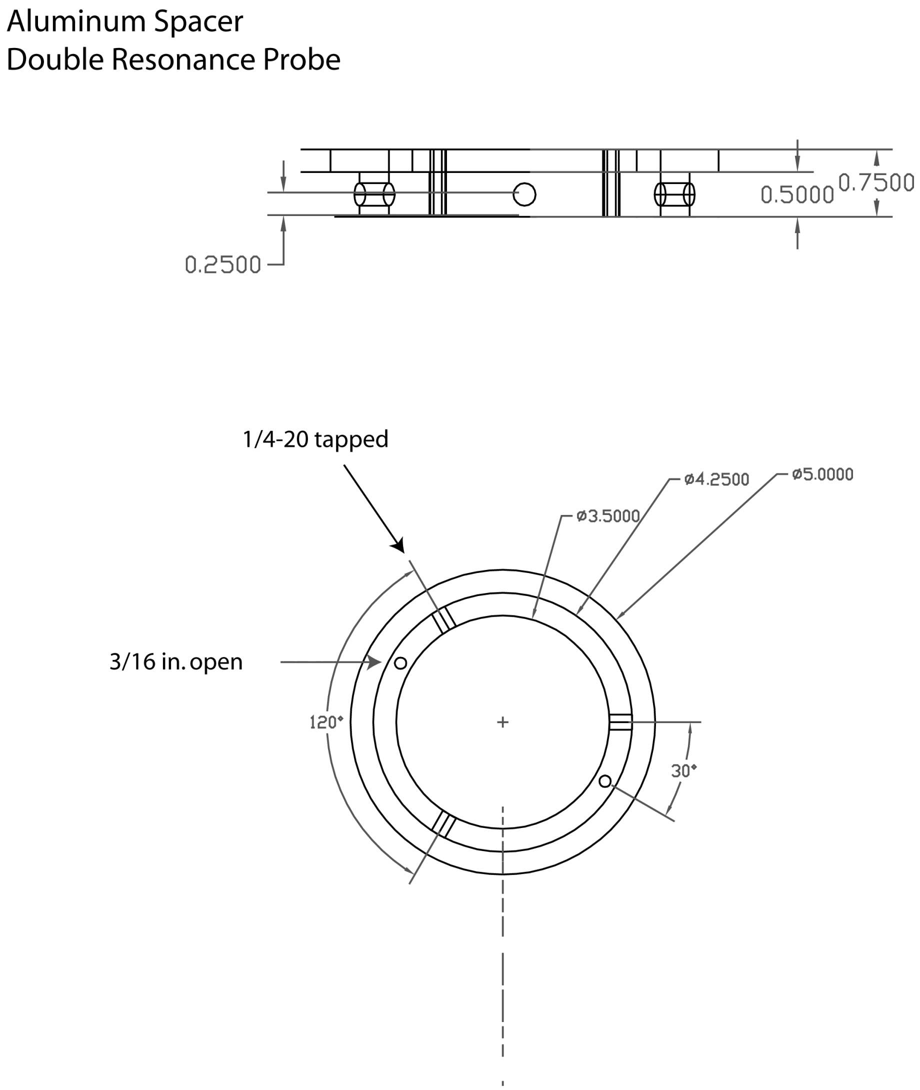

Figure B.11: Double Resonance Birdcage Spacer